NAGHMEH, ABOUALIGALEDARI. Ph.D. Surface-Enhanced Raman Scattering (SERS)
Enhancement using Hybrid Gold nanoparticle-Carbon nanodot Substrate for Herbicides and
Mercury Detection. (2024)
Directed by Dr. Jianjun Wei. 100 pp.

Functionalized nanomaterials are increasingly being utilized for development and innovation in a wide range of industrial fields. Specifically, functional organic/inorganic hybrid nanomaterials and nanocomposites, which have both physicochemical properties of organic and inorganic materials, has potential for use as advanced nanomaterials in various fields. Briefly, hybrid materials are a result of constituting with two or more components, which can interact weakly through van der Waals, electrostatic, or hydrogen bonds between the organic and inorganic components or they can be held together by strong interactions, such as covalent or ionic-covalent bonds. Hybrid nanoparticles not only have the characteristics of both inorganic and organic nanomaterials but can also have unique properties that surpass those of the original components.

Carbon nanomaterials have received considerable attention as SERS-active substrates. Compared with conventional semiconductor quantum dots and semiconductors, carbon nanodots have benefits of low toxicity, excellent biocompatibility, low cost, and simple synthesis. Thus, there is an emerging opportunity to design and create multi-functional hybrid nanomaterials based on carbon nanomaterials with various organic/inorganic materials at the nanoscale or molecule level, for the electronics, catalysis, sensors and energy conversion and storage application.

Interaction of light with metal nanostructures show unique properties given rise to an emergent field called plasmonic. Plasmonic is an optical phenomenon that is very sensitive to the near surface dielectric constant (refractive index, RI) and refers to interaction between free electrons and electro-magnetic fields in metallic materials. Interaction between adsorbed

molecules and surface of plasmonic nanostructures have important influence on SERS. SERS substrates should have abundant free electrons, which is beneficial for the creation of plasmonic hot-spots and ultimately leads to the increase in Raman intensity. Typical metals as SERS substrates are gold and silver nanostructures because they have LSPR-related absorption bands covering most of, visible and near-infrared (NIR) wavelength regimes, which used to excite Raman modes.

This dissertation includes three research thrusts using hybrid carbon nanomaterials. 1) We investigate SERS using a hybrid gold nanoparticles@carbon nanodots substrate for herbicide detection. The hybrid SERS substrate shows excellent signal uniformity compared to AuNPs or CNDs alone. Also, the AuNPs@CNDs illustrates remarkable key parameters of SERS sensor including, repeatability, reproducibility, and stability, which provide the promising application of SERS sensor for ultra-sensitive determination of organic compounds in water and food. 2) We applied 4-Mercaptopyridine (MPY)-functionalized AuNPs@CNDs for mercury detection. The lowest concentration that our MPY-functionalized AuNPs@CNDs nanosensor can detect is 0. 05 nM, which is lower than concentration of Hg^{2+} in drinking water permitted by WHO (6ppb). The sensor had good reproducibility and repeatability and sensitivity for mercury detection. 3) We determine the localization and characteristics of nanoparticles inside cells for sensing application, using hyperspectral-enhanced dark field microscopy (HEDFM). We selected AuNPs and AuNPs@CNDs as a candidate for HEDFM evaluation owing to their unique plasmonic properties. We reported that nano hybrid Unascends and AuNPs can be applied for HEDFM evaluation of herbicides in cell specimen. We hope this research can promote the development of new hybrid materials and composites for sensing of toxic materials in water and foods, so we can benefit human health and environment.

SURFACE-ENHANCED RAMAN SCATTERING (SERS) ENHANCEMENT USING HYBRID GOLD NANOPARTICLES-CARBON NANODOT SUBSTRATE FOR HERBICIDES AND MERCURY DETECTION

by

Naghmeh Aboualigaledari

A Dissertation
Submitted to
the Faculty of The Graduate School at
The University of North Carolina at Greensboro
in Partial Fulfillment
of the Requirements for the Degree
Doctor of Philosophy

Greensboro

2024

Approved by

Dr. Jianjun Wei
Committee Chair

APPROVAL PAGE

This dissertation written by Naghmeh Aboualigaledari has been approved by the following committee of the Faculty of The Graduate School at The University of North Carolina at Greensboro.

Committee Chair	Dr. Jianjun Wei
Committee Members	Dr. Dennis R. LaJeunesse
	Dr. Tetyana Ignatova
	Dr. Peng He

June 21, 2024
Date of Acceptance by Committee

June 2, 2024
Date of Final Oral Examination

ACKNOWLEDGMENTS

First and foremost, I would like to express my deep and sincere gratitude to my advisor, Dr. Jianjun Wei, for his persistent support and invaluable guidance within my whole Ph.D. period. His insights towards problems also inspires me to think issues deeply as well as expand my ideas. In particular, he is not only my academic mentor, but also plays a role of wise man in my life journey. To be honesty, I feel so lucky to become a student in his group.

Next, I would like to thank my committee members, Dr. Tetyana Ignatova, Dr. Dennis R. LaJeunesse and Dr. Peng He for their guidance and insight comments to guarantee the implementation of my project. In addition, I am also thankful to my teachers, Dr. Joseph Starobin, Dr. Hemali Rathnayake, Dr. Dan Herr and, who have guided me over these years as well.

Subsequently, I would like to thank to my lovely group members, Dr. Anitha Jayapalan, Dr. Mengxin Liu, and Dr. Frank Tukur. I feel so lucky to study and collaborate in such big and lovely group. I wish all of you every happiness and all the best.

Last but not least, I would like to express my greatest love to my family. They are always my strongest support and let me focus my achievement without any worries of the rear. I would never go so far without their support and love. Thus, I wish they are in good health and wait me to back and accompany with them. I love them forever!

TABLE OF CONTENTS

CHAPTERS

LIST OF TABLES

LIST OF FIGURES

CHAPTER I: INTRODUCTION

Pesticides including herbicides, insecticides, and fungicides are natural or synthetic compounds, which play a vital role in increasing agriculture products. However, concerns about their widespread distribution in environment and potential hazards to human health and wildlife have been raised [1–3]. According to estimation, less than 0.1% of the pesticides applied to crops actually reaches the target pest, the rest enters the environment and ultimately pollute the environment [4]. It has been proved that absorption of pesticide residues by humans via respiratory system, through skin or via digestive may cause acute and chronic effects, such as hormone disruption, allergies, and cancer [3,5]. Herbicides, substance used to control undesired plants (weedkiller) are the most frequent used group of pesticides, which has a proportional in global consumption around 50-60% [4]. Therefore, there is an urgent need of a fast method that can detect herbicide residues in crops to minimize potential health hazards. Traditional methods used for pesticide detection are expensive, time-consuming, and require substantial sample manipulation, and highly trained operators [3]. Since the discovery of SERS method, it have been used for detection of pesticides residues by using different substrates [5]. SERS method have proven to be fast, sensitive, nondestructive, and highly efficient for probe molecule detection [6], [7]. However, there is still a demand on creating and optimizing SERS substrate to provide largest SERS enhancement possible [8]. This dissertation work focuses on the state-of-the-art advances of hybrid AuNPs@CNDs for detection of toxic materials including herbicides and mercury.

Fundamental of SERS

Concept and Basic Science

SERS is a powerful analytical technique that combines the principles of Raman spectroscopy and nanoscale surface plasmon resonances to achieve significant enhancement of the Raman scattering signal from molecules adsorbed onto or near roughened metallic surfaces or nanostructures [9].

Raman Scattering

Raman scattering is an inelastic scattering process in which a molecule interacts with an incident photon, leading to a shift in the photon's frequency due to the exchange of energy with the molecule's vibrational modes. This frequency shift provides information about the molecular structure and can be used for chemical identification and analysis [10].

Principle and Enhancement Mechanism

SERS was discovered in 1970’s by Fleischman and coworkers when accidently strong Raman spectra of pyridine on a roughened silver surface was observed [11]. In the first SERS experiment, an enhancement in the Raman signal by a magnitude of at least 10^6 was observed. At first the reason of the enhancement was not clear but subsequently, Van Duyne et al. systematically repeated the experiment and mentioned that the unexpected enhancement of Raman scattering is due to electromagnetic effect [12]. In the same period, other researcher proposed a chemical effect for the Raman scattering enhancement [13], [14]. Therefore, the enhancement of Raman scattering in SERS is results of two distinct mechanisms: the electromagnetic mechanism (EM) and chemical mechanism (CM). The electromagnetic enhancement is related to the excitation of localized surface plasmon (LSP) on nanostructured metal surfaces from incident radiation with its frequency closer to the plasmon characteristic oscillations. Therefore, there is an enhancement in the intensity due to a resonance between excitation and the localized plasmon collective oscillations. Areas of strongly enhanced electromagnetic field on the surface of nanoparticles named as “hot-spots” is created by the localized surface plasmon resonance (LSPR). The hot spots are generated on the sharp edges, interparticle junctions, interface between noble metal nanoparticles and metal substrates, and thin gaps between nanoparticles. A significant enhancement of Raman scattering cross section of molecules located in the hot spot can be observed, which make the detection of single molecules possible [15]–[18].

Chemical effect is based on the charge transfer interactions between the molecule and the metal surface. Electrons from metal nanoparticles are transferred to the absorbed molecules and causes a reinforcement in electric field [19], [20].

Electromagnetic enhancement contributes to greater extension (range of 10^6-10^8 times) to the enhancement as compared to the chemical mechanism (range of 10^2-10^3 times) and the fundamental of CM have been less investigated in the literatures than the EM effects [6], [21].

Mathematical models

The mathematical models for describing the SERS involve both classical electromagnetic theory and quantum mechanical considerations.

The electromagnetic enhancement factor (EF)

EF is derived from classical electromagnetic theory, considering the metal nanostructures as antennas that amplify the incident and scattered electromagnetic fields. The EF is given by the following expression:

$EF = (E_{loc}/E_0)^4 \times (E_{scat}/E_{loc})^4$ where:

E_{loc} is the localized electric field at the metal surface, E_0 is the incident electric field, E_{scat} is the Raman scattered electric field.

The first term, $(E_{loc}/E_0)^4$, represents the enhancement of the incident field due to the surface plasmon resonance, and the second term, $(E_{scat}/E_{loc})^4$, represents the enhancement of the Raman scattered field. The localized electric field, E_{loc}, can be calculated using classical electrodynamics and the finite-difference time-domain (FDTD) or boundary element method (BEM) simulations, taking into account the size, shape, and material properties of the metal nanostructures, as well as the excitation wavelength. For simple geometries, like a sphere or an ellipsoid, analytical solutions based on Mie theory or the electrostatic approximation can be used to calculate the enhancement factor [22], [23].

The chemical enhancement (CE)

Chemical factor is typically described using quantum mechanical models that consider the charge transfer between the metal and the adsorbed molecules. One of the commonly used models is the Herzberg-Teller vibronic coupling model, which considers the mixing of the electronic states of the adsorbed molecule with the metal's conduction band states. The chemical enhancement factor (CEF) is given by: $CEF = (\Delta Q/\Delta r)^2 \times (1/\Delta\varepsilon)^2$ where:

ΔQ is the change in the molecular charge due to the charge transfer, Δr is the change in the equilibrium bond length, $\Delta\varepsilon$ is the energy difference between the molecular and metal states involved in the charge transfer.

This model suggests that the chemical enhancement is maximized when the energy difference between the molecular and metal states is minimized, and the molecular polarizability is maximized.

Combined Enhancement

The total SERS enhancement factor is the product of the electromagnetic enhancement factor and the chemical enhancement factor: Total EF = EF × CEF In most cases, the electromagnetic enhancement is the dominant contribution, but the chemical enhancement can play a significant role, especially for molecules that form strong chemical bonds with the metal surface.

These mathematical models provide a framework for understanding the SERS enhancement mechanisms and guide the design and optimization of SERS substrates for specific applications. However, it's important to note that these models have limitations and approximations, and experimental validation is often necessary to fully understand the SERS enhancement in specific systems [22], [24].

Nanoparticles-based SERS substrates

NPs-based SERS substrates, often consisting of engineered NP assemblies or nanostructures, are designed to optimize the LSPR conditions and maximize the EM field enhancement at specific excitation wavelengths. By carefully controlling the NPs properties and assembly, significant Raman enhancements can be achieved, enabling the detection of trace amounts of analytes and providing valuable structural information about the molecules under investigation. Factors influencing SERS enhancement are, material composition (e.g., gold, silver, copper), NP size and shape (e.g., spheres, rods, shells, dimers), NP surface properties (e.g., roughness, hot spots), NP aggregation and interparticle coupling, and excitation wavelength and its overlap with the LSPR. By optimizing these factors, researchers can engineer NP-based SERS substrates with tailored plasmonic properties to achieve maximum Raman enhancement, enabling highly sensitive detection and analysis of various analytes, including biomolecules, chemicals, and environmental pollutants [25], [26].

The Raman enhancement NPs-based SERS is primarily attributed to the EM mechanism, which arises from the amplification of the incident and Raman-scattered fields due to the LSPR effect. Here's how the Raman enhancement occurs: When the incident electromagnetic radiation (e.g., laser) interacts with the metallic NP, it excites the LSPR, leading to a strong concentration and enhancement of the EM field in the vicinity of the NP surface. This enhanced excitation field interacts with the molecules adsorbed or located near the NP surface, increasing the probability of Raman scattering. This phenomenon is called excitation field enhancement. The enhanced excitation field induces a time-dependent dipole moment in the adsorbed molecules, leading to inelastic Raman scattering. The Raman-scattered field from the molecules is also influenced by the LSPR effect. The Raman-scattered field couples to the plasmon modes of the NP, resulting in further enhancement of the scattered field. This enhancement is due to the radiative properties of the NP, which acts as an efficient nanoantenna, amplifying the Raman signal in the far-field [10], [25], [27]. Here the research that has been carried out in NPs-based SERS sensor are summarized as following:

Carbon nanomaterials, including carbon nanotubes (CNTs), fullerenes, graphene, carbon dots (CDs), and nanodiamonds have received considerable attention as SERS-active substrates [14]. CDs (with diameter less than 20 nm), which were discovered in 2004 are classified as carbon quantum dots (CQDs), carbon nanodots (CNDs), and graphene QDs (GQDs). In 2012 for the first time, Shi and co-worker applied CDs without doping and modification as the SERS substrate using an electrophoresis deposition strategy to assemble GQDs nanotube arrays [28]. They observed high sensitivity with the detection limit around 10^{-9} M and 74-fold SERS enhancement, compared to graphene substrate using Rhodamine 6G (R6G) as molecular probes. The excellent SERS property of the GQDs was attribute to the efficient charge transfer between GQDs and target molecules, and large specific surface area of GQDs nanotubes which improve absorption of target molecule and capture of incident light [28]. In current studies, CDs demonstrated strong catalysis to produce gold and silver nanomaterials [29], [30]. CDs have been used to support gold and silver material to prevent direct interaction between analyte and plasmonic materials in which can improve SERS activity. For example, a honeycomb architecture composed of CQDs was synthesized to support gold nanoparticle by Qu et al., [31]. This SERS substrate shows 8-11 times higher SERS activity in comparison to traditional gold nanoparticles. The improved Raman response was attribute to the honeycomb structure of CGDs and uniform distribution of gold nanoparticle with the size less than 10 nm [31]. In another work, core-shell structured Ag@CDs nanoparticle as SERS substrate demonstrate enhancement in SERS activity due to quench of fluorescence of CDs through introduction of silver and excellent absorption of target by Ag@CDs [32].

Due to excellent properties of CNDs such as size dependent photoluminescence emission, strong luminescence, resistance to photobleaching, low cell toxicity, high fluorescence, and hydrophilic properties, they have wide range of application in drug delivery, bio-sensing, bio-imaging, and catalysis [33]. Doping of other elements, such as selenium, boron, in GQDs was also reported by hydrothermal method [34]. Among elemental doping of carbon-based nanomaterials, N-doped carbon dots with high fluorescence efficiency have attracted much attention [33]. However, there are low report on preparation oh highly active N-doped carbon dots for the SERS quantitative analysis [33]. In one study, N-doped carbon dots was synthesized by hydrothermal method, and it was used to catalyze the reduction of chlorauric acid by H_2O_2 to produce gold nanoparticles. The substrate was applied to determine sulfate in water and beer samples (0.02–1.7 μmol/L SO_4^{2-}), with a detection limit of 0.007 μmol/L [33]. Silver nanoparticles protected by small nitrogen-doped Graphene Quantum Dots, (Ag NP@N-GQD) was synthesized for systematic evaluation for glucose sensing in mouse blood sample. The results suggest that the Ag NP@N-GQD is a cost-effective and sustained SERS substrate [35]. Core (Au)-shell (Ag) structure nitrogen dots was synthesized for recognition of nitroaniline isomers by surface-enhanced Raman scattering. It was concluded that NDs are rich in nitrogen and oxygen-containing functional groups and can be used as an efficient reducing and stabilizing agent for the synthesis of AuNPs. The new substrates exhibit high SERS activity with a high SERS enhancement factor of 10^7 [36]. The performance of the undoped, S and N doped GQDs as SERS substrate for detection of RhB in nM level shows the highest SERS signal for N-GQD while S-GQD do not shows any measurable signals [34]. Therefore, based on literature review, we can introduced a newly developed AuNPs@N-doped CNDs and investigate their application for SERS sensing using different kinds of organic and inorganic materials to show the applicability and universality of the SERs substrate for sensitive detection of toxic materials which pave the way for introducing a simple, low cost, and effective platform to secure human health and wild life by detecting toxins in water and foods.

A promising SERS substrate should have abundant free electrons, which is beneficial for the creation of plasmonic hot-spots and ultimately leads to the increase in Raman intensity. Gold and silver nanostructures are typical metals used as SERS substrates due to their localized surface plasmon resonance (LSPR) bands covering the visible and near-infrared (NIR) wavelength regimes necessary to excite Raman modes [1]–[3]. While silver nanoparticles

(AgNPs) offer higher plasmon quality, they are susceptible to oxidation, leading to poor stability [26]. In contrast, gold exhibits superior chemical stability [37], [38].

With advancements in nanotechnology, SERS substrates have been developed from single-composition nanomaterials to multiple component nanomaterials [49]. Hybrid nanomaterials and complex nanostructures composed of carbon nanomaterials and metal nanoparticles, especially metals such as silver and gold have outstanding SERS enhancement [50,51]. Hybrid gold/silver nanoparticle-carbon nanomaterial systems enhance the SERS activity which is attributed to the efficient transfer of electrons from the carbon nanomaterial to gold nanoparticle in addition to the electromagnetic field enhancement via effective plasmonic propagation and the formation of localized hotspots under light illumination [22]. In one study Jiwei et al. [23] applied a periodic array of metal nanopillars and observe desirable value for EF in order of 2×10^8. In another study, Wang et al. [24] improved the overall device stability by using film chips based on polyethylene terephthalate as support for the plasmonic structure, which results in EF in order of 3.14×10^6. As examples, N-doped carbon dots-Au@Ag nanoparticles core-shell structures [25], branched silver-supported carbon dots [22], free-standing Si nanowires decorated with Au/graphene nanoparticles [26] were reported and the EF values were 10^7, 10^8, and 10^6-10^7, respectively. However, less research was focused on gold nanoparticle-carbon nanodots systems for SERS enhancement.

Herein, two key questions are solved as following in Chapter II, including introducing a hybrid SERS substrate based on AuNPs@CNDs with promising SERS application as sensors; what elemental doping of CNDs has best SERS efficiency. These compelling findings may offer promise of a way to development A SERS substrate that has universality for detection of any kinds of organic/inorganic material.

SERS herbicide sensors

Traditional sensitive methods for detection of pesticides residues, such as gas/liquid chromatography combined with mass spectroscopy or rapid techniques, including immunoassays, electrochemical detection, and optical sensors have been widely used by researchers [1]. However, these methods are expensive, time-consuming, and require substantial sample manipulation, and highly trained operators [2]. SERS was discovered in the 1970's by Fleischman et al., when accidently strong Raman spectrum of pyridine on a roughened silver surface was observed [3]. In 1987, Alak et al. applied SERS method using silver-coated micro-spheres for detection of a wide range of pesticides including organophosphorus [4]. Then SERS substrates moved from roughened silver electrodes onto silver and gold colloids. Later, metal films with various thicknesses and nanostructured features were investigated as SERS substrates [5]. Rough metal electrodes are not suitable for theoretical study because the whole electrode is not controllable. Metal colloid-based substrate (silver and gold colloids) are promising SERS substrate owing to their simple preparation, favorable enhancement and low cost compared to other substrates. In colloidal based substrates the SERS signal can be improved by optimizing shape, size, and components [39], [40].

Gold nanoparticles with the optimized size leads to achieving high SERS enhancement which is attributed to the three reasons [7]. Firstly, as the size of gold nanoparticles increase, the surface area of NPs increases which result in increase of amount of herbicide molecules absorbed on the surface and ultimately increase the SERS intensity. Secondly, the local electromagnetic enhancement increases with the increase in particle size, but as the nanoparticle size get bigger the particles absorb less light and less inelastic scatterings occurs on surface, which leads to weakening of overall SERS intensity. Thirdly, there is a correlation between the surface plasmon resonance (SPR) properties of gold nano particles and SERS spectra; the largest SERS enhancement factor is for gold nanoparticles with a surface plasmon resonance maximum between the wavelength for laser excitation and the vibrational bon under study. Studied show that by increasing the size of gold nanoparticles, there is a red shift in surface plasmon band; hence the SERS enhancement field generated from gold nanoparticles maximizes at optimize size of gold nanoparticles. In addition, carbon nanodots with the optimized thickness can improve the chemical enhancement by the enhancement of adsorption of analyte and avoiding signal interferences of probe and gold nanoparticles caused by direct contact of probe molecules with gold substate [8].

In this regard, the key objectives in Chapter II are to 1) design and develop a hybrid AuNPs@CNDs system with optimized size and investigate the optical, and morphology of nanoparticles. 2) investigates SERS enhancement properties of hybrid system using rhodamine 6G (R6G) as a standard SERS probe molecule and compare it with bare GNPs, and CNDs. 3) determine reliability of SERS analysis and applicability of SERS substrate for detection of organic compounds (herbicides). Thereby, the focus of the Chapter II is to investigate hybrid AuNPs@CNDs as a SERS substrate for detection of herbicide.

SERS for mercury detection

Among heavy metals ions, Hg^{2+} is known to be highly toxic even at low concentration. The highest mercury concentration in drinking water that meets the standard is 2 ppb (10 nM). So far, the methods for mercury ions detection are mainly includes colorimetry [41], surface-enhanced Raman chips [42], fluorescent probes [43], electro chemiluminescent immunoassay [44], etc. Surface-enhanced Raman scattering (SERS) is a powerful detection and analysis technique due to the sensing principle based on the molecular Raman spectral signatures.

However, the development of a low-cost, highly sensitive, reproducible, stable, and Raman-active nanostructured substrate for heavy metals detection is still a particular challenge because of the sample complexity. But still direct SERS detection of monoatomic metal ions, such as Hg^{2+}, is challenging due to their small scattering cross section [45]. To address these needs, a sensing platform with excellent flexibility and sensitivity is highly anticipated for mercury detection at low concentration. By takes advantage of MPY-functionalized AuNPs amplification tag, a fiber-optic sensor based on SPR effect was developed for Hg^{2+} detection. The coupling between localized surface plasmon resonance (SPR) increased changes in SPR wavelength, which allowed highly sensitive Hg^{2+} sensing in aqueous solution. The sensor's Hg^{2+} detection limit was 8 nM [46]. A SERS-active nanofibers covered with MPY-modified gold nanoparticles was investigated for the detect of Hg^{2+}. The spectral changes were originated from the effect of the coordination between the nitrogen on MPY and the metal ions and the MPY molecular orientation. The detection limit of this method for Hg^{2+} is lower than 5 nM [47]. In particular MPY is a bifunctional molecule that can be chemisorb onto Au surface through the formation of Au-S bond and coordinate mercuric species via the nitrogen of the pyridine moiety in water [47], [48]. After coordination with Hg^{2+} can confirm more perpendicular orientation of MPY on the AuNPs@CNDs surface, which enable sensitive sensing of mercury. This fact leads to modifying the intensity ratio of the SERS signal and enabling the quantitative determination of Hg ions in aqueous solution. This research also is a step to apply our as-prepared SERS for detection of metal ions in cell without need of functionalization of sensor for specific targets located at different subcellular structures cell membrane and permeability of sensors, which is a typical issue in fluorescent sensors.

In this regard, the key focus in chapter III are to 1) Functionalizing the surface AuNPs@CNDs with MPY for selective detection of mercury. 2) determine the reproducibility, repeatability, and sensitivity of SERS substrate for mercury detection. To this end, the objective of Chapter III is to focus on the synthesizing a SERS substrate that has high selectivity, signal reproducibility, and repeatability for mercury detection.

In summary, the theme of my dissertation research is focus on synthesizing hybrid AuNPs@CNDs with optimized size and composite for sensing application. In particular, the goal of the dissertation research is to advance both the fundamental understanding and technical methods on development (design, synthesis, and testing) of novel hybrid nanomaterials emphasizing SERS enhancement for sensing application. The SERS platforms proposed in this dissertation potentially provide a solution to address one of the grand challenges that our society is facing, i.e., detecting toxic materials in water, thus improving the health and wellbeing of the world’s increasing population.

CHAPTER II: SURFACE-ENHANCED RAMAN SCATTERING ENHANCEMENT USING A HYBRID GOLD NANOPARTICLES@CARBON NANODOTS SUBSTRATE FOR HERBICIDE DETECTION

Abstract

The widespread distribution of herbicides in the environment poses a significant risk to human health and wildlife. Surface-enhanced Raman scattering (SERS) has emerged as a powerful technique for detecting and analyzing herbicides. However, developing a low-cost, highly sensitive, reproducible, stable, and Raman-active nanostructured substrate for herbicide detection remains a particular challenge. In this research, a nanohybrid substrate consisting of gold nanoparticles@carbon nanodots (AuNPs@CNDs) was synthesized by reducing HAuCl4 in the presence of CNDs at 100°C. The optical, chemical, and physical properties of CNDs, AuNPs, and the hybrid AuNPs@CNDs substrates were thoroughly investigated using various techniques including UV-vis spectrometry, Raman spectroscopy, X-ray photoelectron spectroscopy (XPS), scanning electron microscopy (SEM), transmission electron microscopy (TEM), and CytoViva darkfield and hyperspectral imaging. The SERS effect of the substrates was evaluated using Rhodamine 6G (Rh6G), a Raman-active probe, and two groups of herbicides. The results demonstrated a significant increase in the SERS spectra of Rh6G and herbicide molecules detection using the AuNPs@CNDs substrate compared to bare CNDs and AuNPs alone. This suggests that the nanohybrid AuNPs@CNDs SERS substrate holds promise for the detection of herbicides and other organic compounds.

Introduction

The widespread distribution of herbicides in the environment poses a significant risk to human health and wildlife.[1] Accurate, quantitative monitoring the residue of herbicides, especially in water environment, is critical for its management and removal or treatment. Traditionally, a broad range of analytical methods have been used for extraction and determining its concentration, such as gas chromatography (GC),[2] high performance liquid chromatography (HPLC), GC-mass spectrometry (GC-MS), electrochemical and spectrophotometric techniques.[3-6] Advancements in nanomaterials and nanotechnology have provided alternative advantageous sensor technologies, such as nano-electrochemical sensors,[7] molecular-imprinted polymers,[8] and nanoplasmonic surface enhanced Raman spectroscopy (SERS),[9] which may render easy operation, improved sensitivity, portability and real-time and on-site applications.

Surface-enhanced Raman scattering (SERS) technique relies on plasmonic metallic nanostructures to concentrate electromagnetic energy, thereby enhancing the molecular Raman signal. SERS spectroscopy is a powerful technique with diverse applications in medical science and analytical chemistry.[10] Tailored nanostructures enable fast, sensitive, nondestructive, and highly efficient detection of probe molecules, even facilitating single molecule analysis.[11-13] In SERS, the amplification of Raman signals of probe molecules results from the excitation of localized surface plasmon resonance (LSPR) at the metal-dielectric interface substrate. Therefore, the magnitude of SERS enhancement critically depends on the SERS substrate.[14]

Gold and silver nanostructures are typical metals used as SERS substrates due to their LSPR bands covering the visible and near-infrared (NIR) wavelength regimes necessary to excite Raman modes.[15-18] While silver nanoparticles (AgNPs) offer higher plasmon enhancement, they are susceptible to oxidation, leading to poor stability.[19] In contrast, gold exhibits superior chemical stability.[20, 21] Recent SERS studies have focused on developing and optimizing substrates with promising enhancement effects.[22-25] For instance, gold nanorod array was developed and optimized for SERS detection of atrazine herbicide.[26] With advancements in nanotechnology, SERS substrates have evolved from single-composition nanomaterials to multiple-component nanomaterials.[27] This is due to their ability to serve a multi-modal platform for enhanced sensing of analytes, sorbent capability , magnetic recyclability , among others.[28] Hybrid nanomaterials and complex nanostructures comprising carbon nanomaterials and metal NPs, such as AuNPs, have demonstrated exceptional SERS enhancement capabilities.[29, 30]

Carbon dots (CDs) with diameter usually less than 10 nm are classified as carbon quantum dots (CQDs), carbon nanodots (CNDs), and graphene QDs (GQDs).[31] Compared to conventional semiconductor quantum dots and semiconductors, CNDs offer advantages such as low toxicity, excellent biocompatibility, multifunctionality, and straightforward synthesis.[32-34] CNDs represent a novel class of carbon nanomaterials characterized by a spherical morphology and typically an amorphous lattice structure. The functional groups present in CNDs play a crucial role in enhancing surface-enhanced Raman scattering (SERS). These functional groups are typically introduced during hydrothermal synthesis through the doping of heteroatoms like nitrogen (N), sulfur (S), boron (B), phosphorus (P), and others.[35-38]

Recent findings indicate that N-doped CNDs contribute to the improvement of SERS signals, likely because N-doped CNDs facilitate excited state charge transfer to the target molecule through π-π interactions.[39-41] By incorporating CNDs as a shell component to AuNPs with optimized thickness, the chemical enhancement can be improved. This enhancement occurs through increased adsorption of analytes and the prevention of signal interferences from probe molecules caused by direct contact with gold surfaces.[42]

The utilization of AuNPs achieves high SERS enhancement due to their appropriate size, shape, and matching the laser line with the AuNPs' LSPR, which leads to an increase in surface area and local electromagnetic (EM) field enhancement.[42] Previous studies have demonstrated the effectiveness of AuNPs as a SERS substrate for detecting herbicides.[43, 44] In this study, microwave-synthesized hybrid AuNP@CNDs core-shell composite NPs are presented and tested as SERS probes for improved detection of herbicide molecules. This approach capitalizes on the advantageous synergistic effects of both chemical and EM field enhancement from the CNDs and AuNP components, respectively, thereby improving SERS sensing capabilities, especially for detection of the effective components in herbicide formulations.

Materials and methods

Chemical and reagents

Hydrogen tetrachloroaurate ($HAuCl_4$) solution (from Fisher Scientific, Au 44% w/w), sodium citrate (from Fisher Scientific, ≥99%), Rhodamine 6G (from ACROS Organics, 99%), citric acid (from ACROS Organics, 99%), and ethylenediamine (EDA, from Fisher Scientific, 99%) were utilized in this study without undergoing further purification.

The herbicides used in the research, including mesotrione (2-(4-methylsulfonyl-2-nitrobenzoyl) cyclohexane-1,3-dione, ZA1296E), A12738A formulation, and S-metolachlor ((S)-2-chloro-N-(2-ethyl-6-methyl-phenyi)-N-(2-methoxy-1-methyl-ethyl)-acetamide, CGA77102), as well as its formulation LUMAX EZ (A19414A), were obtained from Syngenta Crop Protection, LLC.

Materials characterization

The morphology of both the AuNPs and AuNPs@CNDs was examined using field-emission scanning electron microscopy (FE-SEM) conducted with a Carl Zeiss Auriga-BU FIB

FESEM Microscope. The measurements were performed at an accelerating voltage of 5.0 kV. Additionally, transmission electron microscopy (TEM) was employed using a Carl Zeiss Libra 120 PLUS instrument to further investigate the morphology.

The elemental composition of the samples was determined using X-ray photoelectron spectroscopy (XPS) utilizing a Thermo Scientific ESCALAB Xi+ instrument. Raman spectroscopy was conducted using a Horiba XploRA One Raman Confocal Microscope System, with a 532 nm laser serving as the excitation source.

To assess the optical properties of the CNDs, AuNPs, and AuNPs@CNDs, ultraviolet-visible spectrophotometry was performed using a Varian Cary 6000i spectrophotometer. Fluorescence spectrophotometry was carried out using a Varian Cary Eclipse instrument. Varian Agilent 710 Inductively Coupled Plasma Optical Emission Spectrometer (ICP-OES) with trace element analysis capability for wavelength from 177 to 785 nm was used to determine the concentration of Au in AuNPs@CNDs and AuNPs suspensions.

Nanoparticles synthesis

Synthesis of CNDs. The synthesis of CNDs involved a microwave-assisted procedure conducted at 300 W for 18 minutes. A water solution containing ethylenediamine and citric acid as precursors was utilized by following a previous reported procedure.[32] Following the synthesis, the solution underwent purification using centrifugation for 20 minutes. Subsequently, it was dialyzed for 48 hours against deionized (DI) water. The resulting solution was then freeze-dried for 24 hours to obtain the solid sample.

Synthesis of AuNPs. Gold nanoparticles (AuNPs) were synthesized following the method introduced by Frens,[45, 46] which relies on the citrate reduction of $HAuCl_4$. Initially, a 25 mL solution of $HAuCl_4$ (0.01% by weight) was heated to 97°C. After 15 minutes of temperature stabilization, 375 μL of an aqueous solution of sodium citrate (1% by weight) was swiftly added to the gold solution under continuous stirring, maintaining the temperature at 100°C. Following a 30-minute reaction period, a wine-red suspension containing AuNPs was obtained. Subsequently, the suspension was cooled to room temperature over a 15-minute period while being magnetically stirred. The mixture underwent dialysis using a 1 kDa dialysis membrane for 24 hours to eliminate any unreacted precursor molecules.

Synthesis of AuNPs@CNDs. The hybrid AuNPs@CNDs were synthesized through the reduction of $HAuCl_4$ in the presence of CNDs at 100°C, similar to a reported procedure.[45] In this method, a 150 μL aqueous solution of $HAuCl_4$ (1 mg mL^{-1}) was added to a 3 mL solution of CNDs (0.12 mg mL^{-1}). The mixed solution was maintained at 100°C for 80 minutes. Subsequently, the mixture was allowed to cool to room temperature and then dialyzed using a 1 kDa dialysis membrane for 24 hours to eliminate any unreacted precursor molecules. By adjusting the feeding mass ratio of $HAuCl_4$ to CNDs, AuNPs@CNDs with different sizes can be obtained. At first, CNDs solutions with concentrations ranging from 0.09, 0.11, and 0.12 mg mL^{-1} were added to a 150 μL solution of $HAuCl_4$ (1 mg mL^{-1}) to achieve $HAuCl_4$/CNDs with mass ratios of 2.4, 2.2, and 1.8, respectively. It was observed that the minimum concentration of CNDs that resulted in the formation of AuNPs@CNDs was 0.12 mg mL^{-1}. Then, the concentration of CNDs was maintained constant at 0.12 mg mL^{-1} and different volumes of $HAuCl_4$ ranging from 70-190 μL (yielding $HAuCl_4$/CNDs with mass ratios of 5.2, 3.3, 2.4, and 1.9, respectively) were added to the CNDs to produce hybrid AuNPs@CNDs with different sizes for following SERS studies.

SERS measurements of Rh6G and herbicides by NPs

For the SERS measurements of Rh6G, an aliquot 10 μL of Rh6G aqueous solution was mixed with 50 μL of AuNPs@CNDs, AuNPs, and CNDs aqueous suspension, respectively, and the mixed suspension was sonicated for 30 min. Thereafter, a 60 μL of each sample was dropped on cover glass substrate and the samples were air-dried for 3 hours in fume hood. Note that the AuNPs and AuNPs@CNDs solutions have the same particle concentration of 0.0585 mg mL^{-1} measured by ICP-OES, and concentration of CNDs was 0.12 mg mL^{-1}. The SERS measurements were performed at Horiba XploRA Raman Confocal Microscope using 532 nm light excitation, 50 × objective, grating 1800 gr/nm, and acquisition and accumulation time 5 s.

To measure the SERS spectra of 4 herbicide samples, 10 μL of each herbicide samples were added to 50 μL of AuNPs@CNDs aqueous suspension and sonicated for 30 min. The mixture of samples were dried on the cover glasses for 3 h in fume hood. SERS spectra was obtained on dried samples using 532 nm excitation, 50 × objective, grating 1200 gr/nm, accumulation time 5 s, and acquisition 35 s.

The first group of herbicides was CGA77102 (S-metolachlor 86.6% by weight) and A19414A formulation (S-metolachlor 27.1% by weight). The sample solutions containing desired concentration of CGA77102 and A19414A formulation ranging from 10^{-12}-10^{-3} M were determined with respect to effective S-metolachlor component without extraction. The same procedure was carried out for the second group of herbicides, ZA1296E (mesotrione 60.0% by wt.) and A12738A formulation (mesotrione 40.0% wt.).

Results and discussions

Characterization of CNDs, AuNPs, and AuNPs@CNDs

Size and morphology of the NPs were characterized using SEM and TEM. SEM and TEM images of AuNPs (**Figure 1**A) reveal the spherical shape of AuNPs with a size of approximately 50 nm, consistent with the 540 nm absorption of the UV-vis spectra of AuNPs (**Figure 2**A). The TEM images of hybrid AuNPs@CNDs (Figure S1) at different $HAuCl_4$/CNDs mass ratio (5.2, 3.3, 2.4, and 1.9) show that the AuNPs@CNDs obtained from mass ratio of 2.4 have spherical shape and the NPs are not agglomerated and more uniformly distributed compared to other mass ratios. By changing the $HAuCl_4$/CNDs mass ratio there is a change in the size distribution of AuNPs@CNDs and the samples with the mass ratio of 2.4 has a size distribution between 40-50 nm (Figure S2). The HR-TEM images of 2.4-ratio AuNPs@CNDs (**Figure 1**B) suggest successful wrapping of AuNP cores by CND structures. **Figure 1**B (d) confirms 0.24 nm lattice fringe of its crystalline structure corresponding to (111) planes of AuNPs.[47]

Figure 2-1- (A) SEM image (a) and HR-TEM image (b) of the AuNPs; (B) TEM image (a), HR-TEM images (b-c) and zoom-in the lattice fringe of crystalline structure.

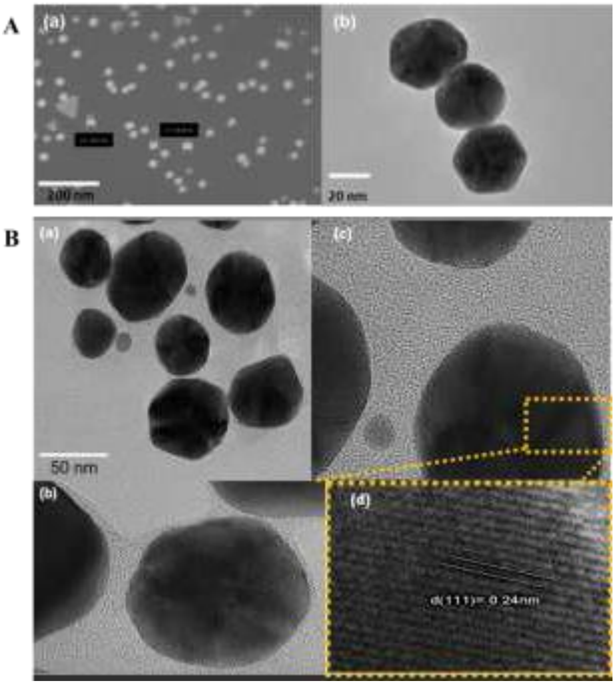

To further confirm the formation of hybrid AuNP@CNDs, UV-visible absorption spectra were collected and compared with three samples, i.e., the AuNPs, CNDs and the hybrid. In **Figure 2**A, the spectrum of AuNPs shows a SPR peak at 540 nm, which indicate the formation of the AuNPs with a size of around 50 ±7 nm.[42] The absorption spectrum of CNDs displays a typical peak at 360 nm which is attributed to n–π* transition of C=O.[48] The absorption spectrum of

AuNPs@CNDs presents both the plasmon absorption peak at 540 nm of the AuNP core[45] and the 360 nm peak for CNDs, corroborating the production of the hybrid NPs. Comparing the UV-vis absorption from different mass ratio products (Figure S3), the 2.4 mass ratio AuNP@CNDs have the highest plasmonic peak around 540 nm along with featured peak 360 nm for the CNDs, implying a potential for Raman signal enhancement.

Figure 2-2- (A) UV-Vis absorption spectra of AuNPs, CNDs and hybrid AuNP@CNDs; (B) SERS of Rh6G with the hybrid AuNPs@CNDs generated with different mass ratios.

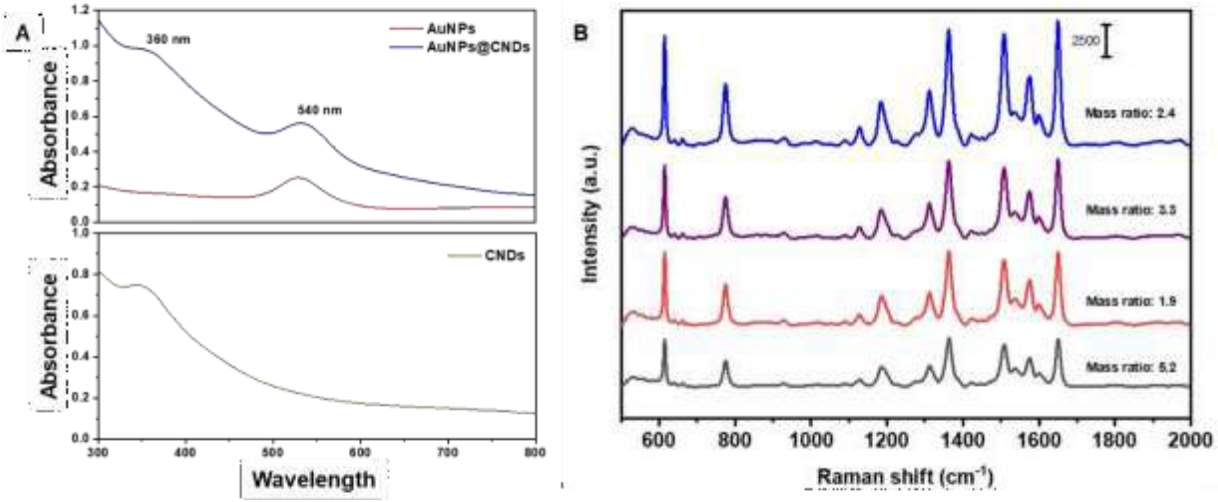

The SERS performance of the hybrid AuNPs@CNDs substates obtained from different mass ratios was evaluated using Rh6G. **Figure 2**B presents the SERS spectra of Rh6G at the concentration of 48×10^{-8} M using AuNPs@CNDs substrates produced from different $HAuCl_4$/CNDs mass ratio. It is apparent that the 2.4 ratio hybrid substrate provides the best SERS signal enhancement of Rh6G, plausibly due to the size range of generated AuNPs. The results further confirm the plasmonic property observed in UV-vis spectra. Therefore, the mass ratio 2.4 AuNPs@CNDs hybrid substrate is selected for the further investigation and applied in herbicide sensing studies.

The structural, composition and spectroscopic properties of the synthesized NPs were further performed and analyzed. Raman spectra of both CNDs and AuNPs@CNDs (Figure S) show two distinct peaks at 1340 cm^{-1} and 1590 cm^{-1}, which correspond to the D and G band of the carbon component, respectively. D band corresponds to structural defects in graphitic sp^3-hybridized carbon, whereas the G band is related to the vibration of sp^2 carbon atoms in a 2D hexagonal lattice.[49, 50] The relative intensity of D and G band (D/G ratio) in Raman spectra of AuNPs@CNDs is 0.780, whereas this ratio is 0.741 for CNDs. The D and G band intensities of AuNPs@CNDs are much higher than that of CNDs, suggesting the enhanced defect effect of AuNPs.[51, 52] The photoluminescence (PL) spectra of CNDs and AuNPs@CNDs (Figure S4b) show that PL intensity of AuNPs@CNDs is decreased compared to CNDs using 360 nm as excitation light, which indicate that the PL of CNDs is quenched in the AuNPs@CNDs system. This phenomenon is attributed to a photo-induced electron transfer process between the CNDs and AuNPS.[45, 51]

Full XPS scan spectra of CNDs and AuNPs@CNDs exhibit three peaks at 285.5, 399.0 and 531.0 eV, which are attributed to C 1s, N 1s, and O 1s, respectively.[53] Compared to the XPS spectrum of CNDs, the XPS spectrum of the AuNPs@CNDs presents a peak of Au element at 335 eV (Figure S5a-b). The C 1s XPS spectra of CNDs and AuNPs@CNDs (Figure S5d-e) show the peaks at 284.3, 285.4, and 287.5 eV which are attributed to C-C, C-O-C, O-C=O groups, respectively. The N 1s XPS spectra in Figure S5c feature two peaks corresponding to pyridinic nitrogen (398 eV) and pyridone nitrogen (399.6 eV).[54] The O 1s band (Figure S5f) can be deconvoluted into three peaks located at 531.4 and 531.9 which represents the C-O and C=O groups, respectively.

Dark-field CytoViva Hyperspectral imaging system was used to measure the light scattering from AuNPs and AuNps@CNDs distributed on a glass substrate. CytoViva hyperspectral imaging system enables both optical and hyperspectral imaging of samples, which can be used for spectral characterization and spectral mapping of nanoscale samples.[48, 55] In experimental measurement, unpolarized plain light (broad band) from a halogen lamp was used as incident light to illuminate the nanoparticle samples from the top. The reflecting light signal captured by a 60 × objective lens is then collected using in a darkfield CytoViva hyperspectral imaging system (**Figure 3**). The peak at around 550 nm is corresponding to the SPR of AuNPs, which is in accordance with the UV-vis spectra and confirm that the SPR of AuNPs occurs at around 540 nm. It is noteworthy that the peak around 580 nm can be attributed to the SPR of aggregation of group of AuNPs.[56] The intensities of SPR peaks of AuNPs@CNDs are much higher than that of AuNPs, suggesting the enhancement effect of AuNPs@CNDs. A new resonant mode located at 615 nm appeared after AuNPs is covered by CNDs, this is probably because of coupling between AuNPs and CNDs.[47]

Figure 2-3- The extracted reflection spectra obtained from the CytoViva hyperspectral.

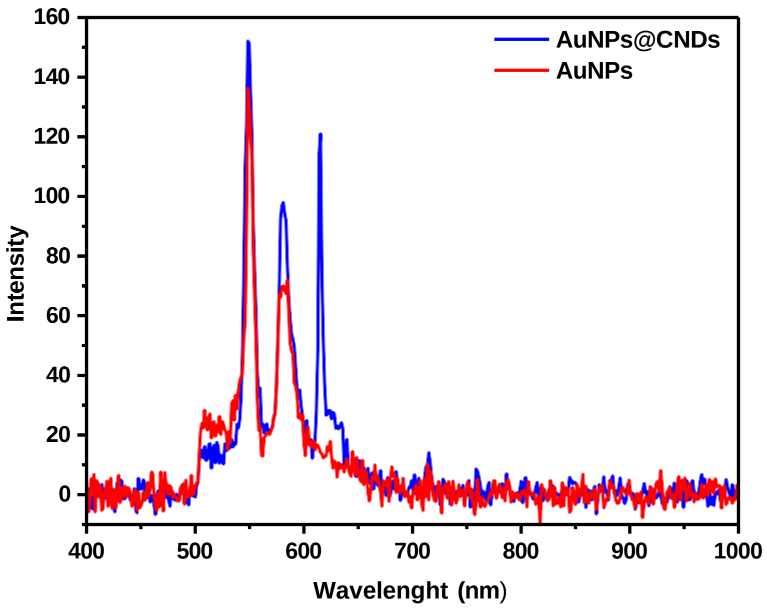

SERS properties of NPs

Rh6G was used as a Raman reporter to perform the SERS evaluation using three NPs, i.e., AuNPs@CNDs, CNDs, and AuNPs prior to the application in herbicide detection. **Figure 4**A displays the SERS spectra of 48×10^{-8} M Rh6G after mixing with AuNPs@CNDs, AuNPs, CNDs, respectively, and Rh6G only for comparison. An obviously increased SERS signal was observed from the AuNPs@CNDs hybrid substrate. The great signal amplification (>10x) of the main signature peaks of Rh6G obtained using the AuNPs@CNDs was obtained comparing to that of using the AuNPs for Rh6G. The band at 614 cm^{-1} was assigned to C-C-C ring in-plane in xanthene ring, whereas those around 771, 1127, and 1183 cm^{-1} were attributed to C-H ring in xanthene or phenyl ring.[57] The prominent peaks in the range of 1311, 1362, 1507, 1573, and 1650 cm^{-1} were due to the symmetric modes of in-plane C-C stretching vibrations in xanthene or phenyl ring which are the characteristic Raman scattering of Rh6G.[20, 58] These results confirm that the hybrid AuNPs@CNDs system can significantly improve the SERS performance in terms of signal enhancement, implying enhanced sensitivity and accuracy for sensing application.

Figure 2-4- (A). SERS spectra of Rh6G (48×10^{-8} M) using CNDs, AuNPs, and AuNPs@CNDs, respectively. (B) Raman signal at 1650 cm^{-1} vs. Rh6G concentration in logarithmic value using AuNPs@CNDs for SERS measurement.

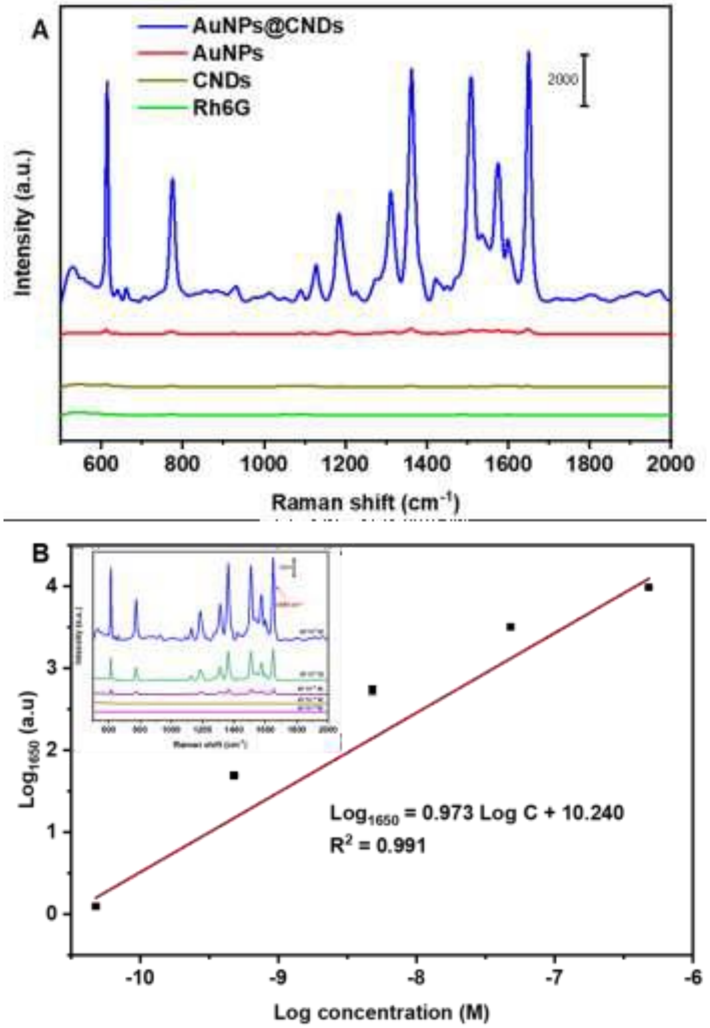

Next, we collected the SERS of Rh6G at different concentration ranging from 48×10^{-12} to 48×10^{-8} M using the same AuNPs@CNDs substrate. **Figure 4**B shows that there is an increase in the Raman signal intensity of the characteristic Rh6G peaks by increasing the concentration of Rh6G. By plotting LogI$_{1650}$ (logarithm of SERS peak intensity at 1650 cm^{-1}) versus LogC (logarithm of Rh6G concentration), a linear calibration curve was obtained, where the square coefficient of determination (R^2) is 0.991, demonstrating a linear function of the Raman intensity vs. the concentration.

To quantitatively evaluate the enhancement ability of AuNPs@CNDs, the enhancement factor (EF) values of SERS peak for Rh6G was calculated by employing the following equation:

$$\mathrm{EF} = \frac{I_{\mathrm{SERS}} \times C_{\mathrm{Raman}}}{I_{\mathrm{Raman}} \times C_{\mathrm{SERS}}}$$

Where C_{SERS} stands for the concentration of probe molecules that lead to a SERS signal I_{SERS}, and C_{Raman} represent the concentration of probe molecules that cause a Raman signal I_{Raman}. The data are listed in table 2, where the EF values of the AuNPs@CNDs is 34.72-fold higher than those of AuNPs. The excellent SERS effects induced by AuNPs@CNDs can be explained as follows: On the one hand, based on Cytoviva Hyperspectra (Figure 2.3), the intensities of SPR peaks of AuNPs@CNDs are much higher than that of AuNPs, suggesting the enhancement effect of AuNPs@CNDs. On the other hand, the N-doped CNDs are considered to be affiliative to the Rh6G dye molecules due to the π-π stacking interaction and electrostatic interaction.

The reproducibility and stability of the SERS substrate for sensing are important for detection of analytes of interest especially if deployed in the field [49]. The SERS responses collected at 18 random points on the same sample using AuNPs@CNDs and 48×10^{-8} M Rh6G displays the uniformity of the sample (Figure 5A) based on the standard deviation of 0.9% from the peak intensity at 1650 cm^{-1}. The uniformity in SERS signals recorded confirms good reproducibility and homogeneity of using the hybrid AuNPs@CNDs in sample preparation and detection. Furthermore, to confirm the batch-to-batch reproducibility, 6 different batches of AuNPs@CNDs substrates were used for SERS measurement of Rh6G and the SERS intensity at peak 1650 cm^{-1} were collected from 3 random points of each substrate. Figure 5B demonstrates averaged Raman intensity for the six samples which show excellent reproducibility. Figure 5C-D shows the stability during the storage by measuring the UV-visible spectra of AuNPs@CNDs and SERS spectra of 48×10^{-8} M Rh6G with AuNPs@CNDs up to 60 days, respectively. There are no significant changes in both spectra, which confirms the high stability of the hybrid AuNP@CNDs substrate.

Figure 2-5- (A) Multiple points Raman signal collection profiles of AuNPs@CNDs with Rh6G of 48×10^{-8} M; (B) Raman signal intensity at 1650 cm^{-1} of Rh6G with 6 different batches of AuNPs@CNDs; (C) UV-vis spectra of the stored AuNPs@CNDs for the period of 10-60 days.

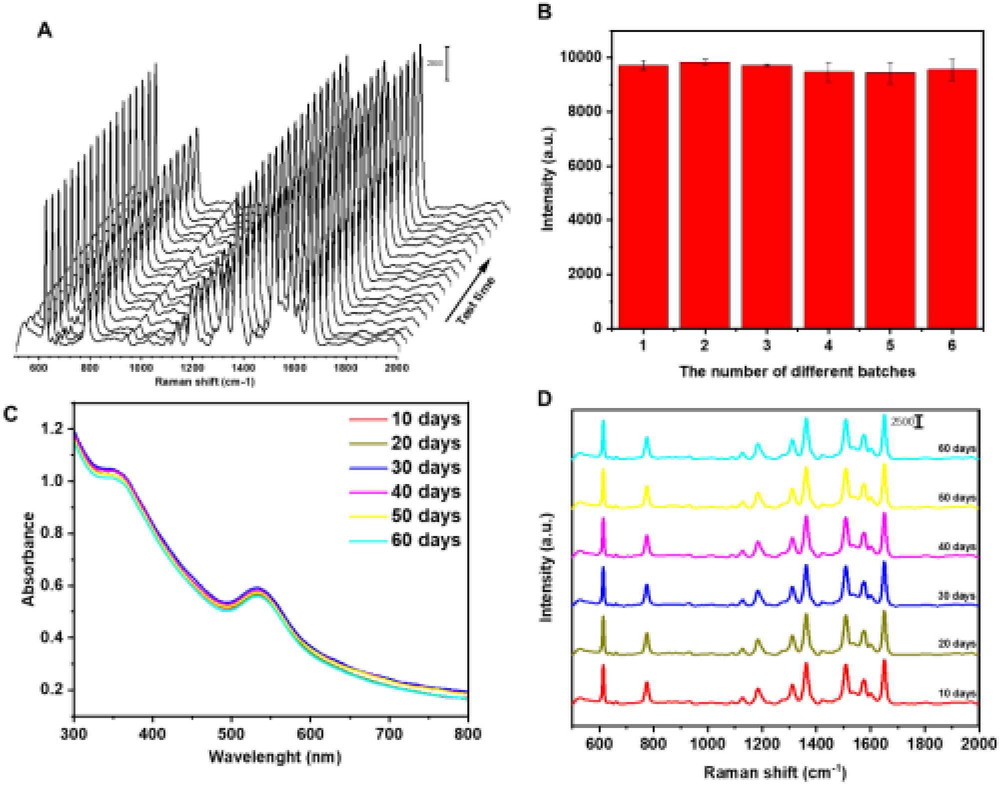

SERS detection of herbicide molecules

The 2.4-ratio AuNPs@CNDs substrate in solution was further applied for detection of two different groups of herbicides. As described in the experimental section, the first group of herbicides is CGA77102 (S-metolachlor 86.6% wt.) and A19414A formulation (S-metolachlor 27.1% wt.). S-metolachlor is a member of the chloroacetanilide family of herbicides, which is used for grass and broadleaf control in corn, soybean, etc. The signal amplification of the main Raman peaks at 994.4 and 989.6 cm^{-1} obtained using the AuNPs@CNDs to that of bare AuNPs is calculated to be 10.8 and 7.3- fold for CGA77102 and A19414A, respectively (Figure S6a-b).

The second group of herbicides is ZA1296E (mesotrione, 60% wt.) and A12738A formulation (mesotrione 40% wt.) with the main effective component of mesotrione. Mesortione has an aromatic ketone and is a toxic synthetic herbicide in agriculture industry for the selective contact and residual control of broadleaf weeds in field corn. According to **Figure** S6c-d, the SERS peaks at 1526, 1552, and 1608 cm^{-1} are attributed to the C=C stretching in carotenoids, the central 16-membered-ring vibrations and the C-C stretching of the pyrrole ring in chlorophyll, and ν phenyl ring in phenolic compounds, respectively.[59] Similarly, the hybrid AuNPs@CNDs render greater Raman signal enhancement than the AuNPs.

Figure 2-6- SERS spectra of (A) CGA77102, (B) A19414A formulation with different concentrations (B), (C) ZA1296E, and (D) A12738A formulation at the effective component concentration from 10^{-3}-10^{-10} M using AuNPs@CNDs.

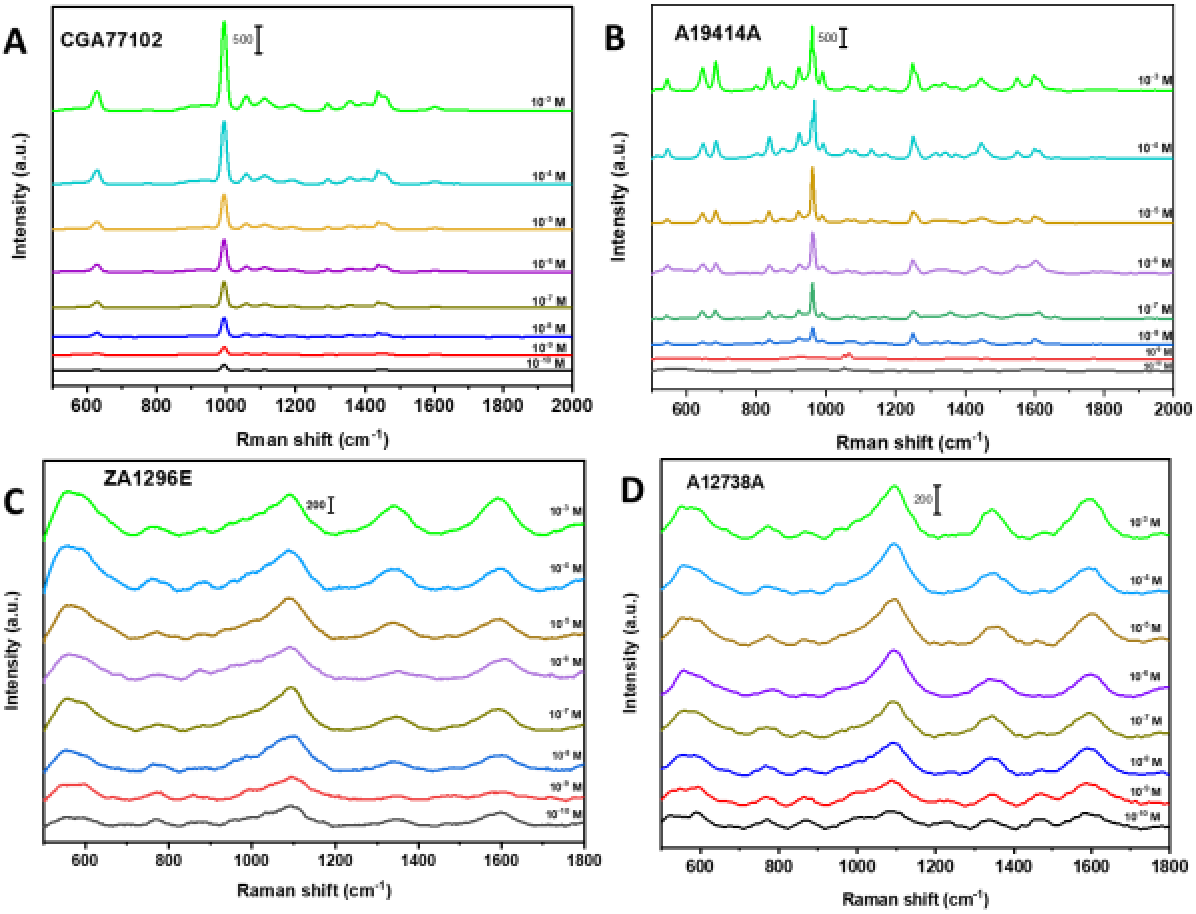

Figure 6 shows the SERS spectra of the four herbicide samples using the hybrid AuNPs@CNDs as Raman enhancement probes. The spectra of CGA77102 and A19414A with different concentrations indicate the Raman signal intensity decline along with decreasing concentration. Similarly, the SERS spectra of ZA1296E and A12738A with different concentrations show the Raman intensity decline along with decreasing concentration. Linear calibration curves as a function of the herbicide concentration ranging from 10^{-10} to 10^{-3} M are achieved by plotting the $LogI_{994.4}$ and $LogI_{989.6}$ versus LogC for CGA77102 and A19414A (**Figure 7**A-B) which demonstrate a linear detection response with R^2 values 0.984 and 0.970, respectively. A small shift of the characteristic peak position between CGA77102 and A19414A (994.4 vs. 989.6

cm^{-1}) could attribute to the different components in the original samples or interaction between substrates and analytes. The logarithm value of SERS intensity of peak 1081 and 1081 cm^{-1} versus the logarithm concentration of ZA1296E and A12738A in range of 10^{-10} - 10^{-3}M was plotted with a good linearity ($R^2 = 0.992, 0.9749$) for ZA1296E and A12738A respectively as shown in **Figure 7**C-D.

The broad Raman peaks in Figure 2.6C-D is due to the fact that Raman scattering involves transitions between quantized vibrational energy levels. The probabilistic nature of these transitions, governed by quantum mechanics, contributes to the intrinsic line width. This fundamental broadening sets a lower limit on the width of Raman peaks. In practice, additional factors (like thermal effects, instrumental limitations, or sample heterogeneity) often contribute significantly to the observed peak width, but these are not as fundamentally rooted in basic physical principles as the natural line width.

Figure 2-7- Calibration curves plotted with logarithm Raman signal vs. Concentration using the marker peak intensity for CGA77102 at 994.4 cm^{-1} (A) and A19414A at 989.6 cm^{-1} (B), ZA1296E at 1081 cm^{-1} (C), and A12738A at 770 cm^{-1} (D).

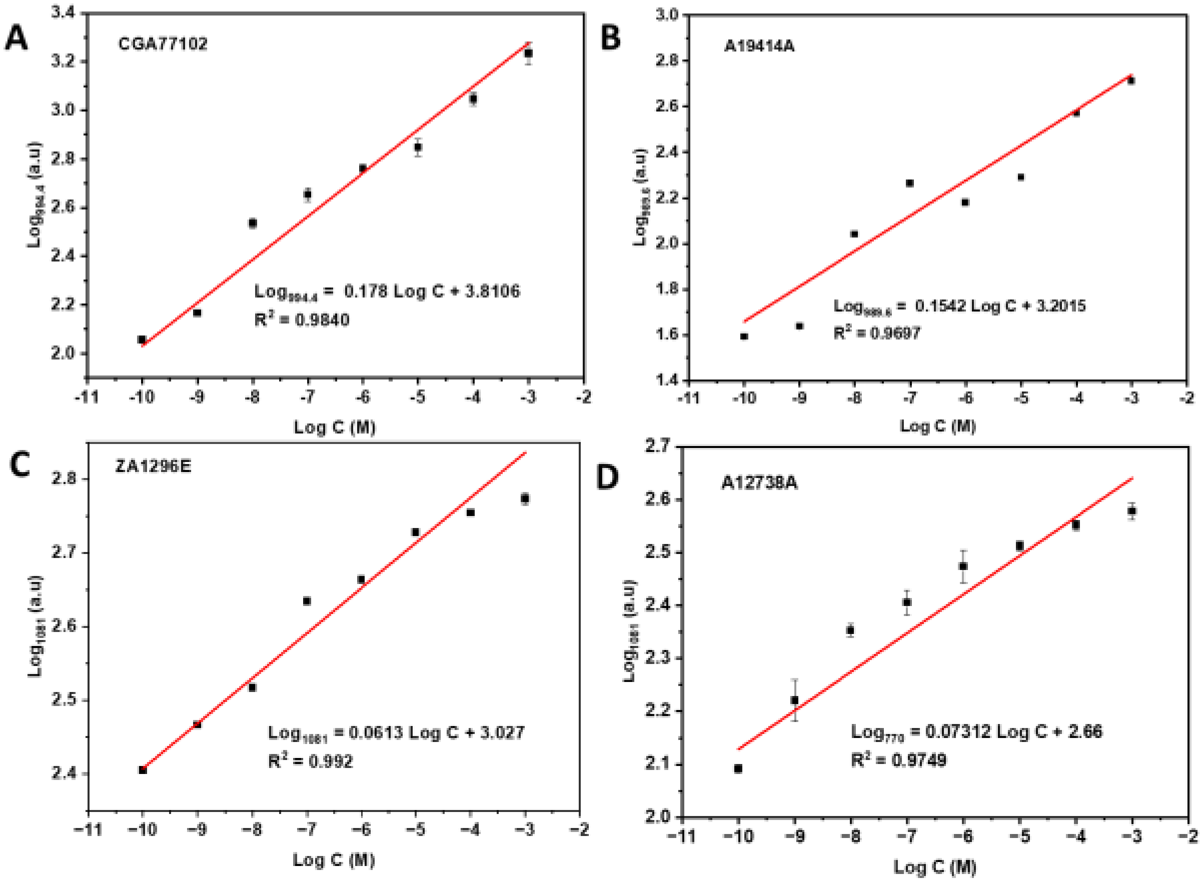

Detection of herbicides in tap water and recovery experiments

To test the capability of using the hybrid AuNPs@CNDs as Raman probe for herbicide detection, we spiked the herbicide sample into tap water and obtained the SERS spectra to evaluate the recovery rate, i.e., the percentage of measured concentration to the spiked concentration. In these experiments, three distinct concentration levels at low (10^{-10} M), medium (10^{-6} M), and high (10^{-3} M) concentrations were prepared, and the SERS spectra were obtained (Figure S7). Based on the Raman signal intensity at the marker peak of each sample we got the measured concentrations according to the calibration curves in Figure 7. The recovery rate of known amounts of spiked herbicides in tap water were calculated with respect the spiked concentration and reported in Table

1. The results indicate that the recovery rate at medium and high levels is > 90%, higher than the lower level in the range of 87-88%. These results demonstrate the effectiveness using the AuNPs@CNDs for detection of herbicides in tap water.

Table 2-1- Recovery rate (%=Measured Conc/Spiked Con.×100) of spiked herbicides in tap water.

Herbicide	**Spiked herbicide (M)**	**Measured (M, averaged)**	**Recovery rate (%)**
CGA77102	10^{-3}	0.95×10^{-3}	95 ± 2
	10^{-6}	9.66×10^{-7}	96 ± 1.8
	10^{-10}	6.73×10^{-11}	87 ± 1.5
A19414A	10^{-3}	0.95×10^{-3}	95 ± 2.1
	10^{-6}	9.82×10^{-7}	98 ± 1.2
	10^{-10}	8.71×10^{-11}	87 ± 1.9
ZA1296E	10^{-3}	0.87×10^{-3}	87 ± 4.8
	10^{-6}	9.91×10^{-7}	89 ± 3.0
	10^{-10}	7.69×10^{-11}	87 ± 4.0
A12738A	10^{-3}	0.88×10^{-3}	88 ± 1.0
	10^{-6}	9.61×10^{-7}	96 ± 1.1
	10^{-10}	8.71×10^{-11}	87 ± 3.5

Conclusion

Hybrid AuNPs@CNDs SERS substrate was synthesized with a simple approach using CNDs as reducing and stabilizing agent. The SERS substrate at different mass ratios of CNDs to $HAuCl_4$ in synthesis were evaluated using Rh6G and it turned out the ratio 2.4 renders the highest Raman enhancement. The enhancement is believed arising from electronic coupling at the interference of gold and carbon structures with the specific size and composites for optimized localized electromagnetic field in SERS. The hybrid AuNPs@CNDs substrates produce highly enhanced Raman signal with excellent response that is highly reproducible compared to AuNPs or CNDs alone when the substrate was used for herbicide detection. The SERS measurement of four different herbicide samples illustrate excellent repeatability, reproducibility, and stability, and demonstrate capability of sensitive determination of the herbicides spiked in tap water.

CHAPTER III: MERCAPTOPYRIDINR-FUNCTIONALIZED GOLDNANOPARTICLES@CARBON NANODOTS FOR MERCURY DETECTIONM

Abstract

Mercury (II) ions (Hg^{2+}) is one of the most hazardous pollutants causing serious damage to the environment and human health. Surface-enhanced Raman scattering (SERS) has emerged as a powerful technique for detecting and analyzing different kinds of toxic materials including mercury. However, developing a low-cost, highly sensitive, reproducible, and repeatable nanostructured substrate for mercury detection remains a particular challenge. Here, 4-mercaptopyridine (MPY) was selected as the sensing material and was decorated on the surface of AuNPs@CNDs to detect Hg^{2+}. The optical, chemical, and physical properties of nanostructured substrates were thoroughly investigated using various techniques including UV-vis spectrometry, Raman spectroscopy, X-ray photoelectron spectroscopy (XPS), scanning electron microscopy (SEM), transmission electron microscopy (TEM), and Fourier transform infrared (FTIR) spectroscopy. The sensor exhibited good selectivity for Hg^{2+} detection compared with other common metal ions in water. The sensor detects Hg^{2+} with a concentration as low as 0.05 nM. Furthermore, we validated the sensor's practicality for Hg^{2+} detection in simulated water samples.

Introduction

Heavy metals ions are taken into account as one of the most important pollutants in the environment, representing a serious threat to the environment and living organisms[50]–[52]. Among the heavy metal ions, Hg^{2+} is known to be highly toxic even at low concentration [46], [53]–[58] that can cause damage to the central nervous system, kidney, and other vital organs[59]. Based on the United States Environmental Protection Agency (EPA) and the World Health Organization (WHO), the highest mercury concentration in drinking water that meets the standard is 2 ppb (10 nM) and 6 ppb (30 nM), respectively [59], [60]. So far, the methods for mercury ions detection are mainly includes atomic fluorescence [61]–[64], inductively coupled plasma mass spectrometry [65]–[68], and atomic absorption spectroscopy [69]–[71]. These methods are time consuming, destructive, require expensive instrumentations, complicated sample manipulation, and large sample volume. To, address these issues, sensing platforms for detection of Hg^{2+} have been used, including colorimetry [72]–[74], surface-enhanced Raman chips [42], [75], fluorescent probes [43], [76]–[81], electro chemiluminescent immunoassay [44], [82]. However, most of the fluorescent probes involve toxic reagents and complex synthesis, which limit their practical applications. Electrochemical sensors are sensitive but have low selectivity. Compared to above mentioned techniques, surface-enhanced Raman scattering (SERS) is a powerful and simple detection and analysis technique with high selectivity and sensitivity [83]–[97].

However, direct SERS detection of monoatomic metal ions, such as Hg^{2+}, is challenging due to their small scattering cross section and the absence of vibrational modes in ions [98]. Therefore, SERS sensor based on the turn-on and turn-off mechanism have been identified as a promising method for indirect detection of Hg^{2+} [42], [99]–[103]. Discovery of Hg^{2+}- mediated thymine-thymine (T-T) mismatches was an important development in SERS sensors based on the turn-on signal, which relies on the T-Hg^{2+}-T coordination chemistry and the formation of NP aggregates [104]–[109]. As examples of SERS sensors that can detect Hg^{2+} based on the increase in the SERS intensity in the presence of metal ion, AuNPs decorated silicon nanowire array (SiNWAr) [110], and DNA modified AuNPs [111] was investigated. Opposite to turn-on signals is the turn-off signal where the mechanism is based on the decrease in SERS signal. For instance when high affinity of Hg^{2+} with Au displaces SERS probes such as rhodamine B molecules attached to the surface of Au [112]. Although these methods are sensitive and selective but surface functionalization of nanoparticles with DNA probe is time consuming and the signal is not reproducible due to uncontrollable aggregation of nanoparticles that leads to different aggregate size with different numbers of hot spots.

Inspired by these studies, herein, we proposed to develop a sensitive and selective SERS approach for Hg^{2+} detection based on MPY - functionalized AuNPs@CNDs, where the MPY is a bifunctional molecule that coordinate mercuric species via the nitrogen of the pyridine moiety in water [47], [48]. We introduce a simple and low-cost method to successfully modify the surface of AuNPs@CNDs with MPY. The SERS substrate provide a repeatable and reproducible signal for mercury detection that can be easily apply for sensitive detection of mercury in water at a short time without the need for complex sample manipulation and highly trained operators. The sensing was based on the characteristic spectral changes produced by the complexation of the mercury with an organic ligand (MPY), which allows selective identification and quantification of mercury at trace level.

Materials and methods

Chemical and reagents

Hydrogen tetrachloroaurate ($HAuCl_4$) solution (Fisher Scientific, Au 44% w/w), sodium citrate (Fisher Scientific), Rhodamine 6G (ACROS Organics), citric acid (ACROS Organics), and ethylenediamine (EDA, Fisher Scientific) were used in this work without further purification. Mercury(II) chloride, ACS, 99.5% min and Methylmercury(II) chloride was purchased from Thermo Scientific Chemicals. 4-Mercaptopyridine (MPY)

Materials characterization

Elemental composition of the samples was characterized using XPS (Thermo Scientific ESCALAB Xi$^+$). Raman spectroscopy was conducted using a Horiba XploRA One Raman Confocal Microscope System. Ultraviolet-visible spectrophotometry (Varian Cary 6000i) and fluorescence spectrophotometry (Varian Cary Eclipse) were used to investigate the optical properties of the NPs. Fourier transform infrared (FTIR) spectroscopy (Agilent FTIR) was used to investigate surface functional groups. The morphology of NPs was examined using field-emission scanning electron microscopy (FE-SEM) conducted with a Carl Zeiss Auriga-BU FIB FESEM Microscope. The measurements were performed at an accelerating voltage of 5.0 kV. Additionally, transmission electron microscopy (TEM) was employed using a Carl Zeiss Libra 120 PLUS instrument to further investigate the morphology.

Synthesis of NPs

Synthesis of CNDs. CNDs was synthesized followed by our previous method applying a microwave-assisted procedure conducted at 300 W for 18 minutes using aqueous solution of ethylenediamine and citric acid as precursors, following by the purification using centrifugation for 20 minutes [113]. Subsequently, it was dialyzed freeze-dried to obtain the solid sample.

Synthesis of AuNPs. AuNPs were synthesized following the method introduced by Frens [114], [115]. Initially, a 25 mL solution of $HAuCl_4$ (0.01% by weight) was heated to 97°C follow byadding 375 μL of an aqueous solution of sodium citrate (1% by weight) under continuous stirring, maintaining the temperature at 100°C for 30-minute. Subsequently, the suspension was cooled to room temperature and dialyzed.

Synthesis of AuNPs@CNDs. The hybrid AuNPs@CNDs were synthesized followed our previously reported method. Briefly, a 150 μL aqueous solution of $HAuCl_4$ (1 mg mL^{-1}) was added to a 3 mL solution of CNDs (0.12 mg mL^{-1}) and mixed continuously at 100°C for 80 minutes. Subsequently, the mixture was cooled to room temperature and then purified using dialysis method. By adjusting the feeding mass ratio of $HAuCl_4$ to CNDs, AuNPs@CNDs with different sizes can be obtained.

Synthesis of MPY-functionalized AuNPs@CNDs. 150 μL aqueous solution of $HAuCl_4$ (1 mg mL^{-1}) was added to 3 mL solution of CNDs (0.12 mg mL^{-1}) and the mixed solution was kept at 100°C for 40 min. Then 3 mL solution of MPY (0.36 mg mL^{-1}) was added to the mixture and kept stirring for 40 min at the same temperature.

SERS measurement of Rh6G and Hg^{2+} by MPY-functionalized AuNPs@CNDs

For the SERS measurement, 10 μL of Rh6G or $HgCl_2$ aqueous solutions was mixed with 50 μL of AuNPs@CNDs aqueous suspension and the mixed suspension was sonicated for 30 min. 60 μL of each sample was dropped on cover glass substrate and the samples were air-dried for 3 hours in fume hood before SERS measurement. The SERS measurements obtained using 532 nm excitation, 50 × objective, grating 1800 gr/nm, and acquisition and accumulation time 5 s for Rh6G detection. While for Hg^{2+} detection, 532 nm excitation, grating 1200 gr/nm, and accumulation and acquisition time of 10 s was applied.

Results and discussions

Characterization of AuNPs, CNDs, and AuNPs@CNDs

SEM and TEM images of AuNPs (Figure S1A-B) reveal the spherical shape of AuNPs with a size of approximately 50 nm, consistent with the 540 nm absorption of the UV-vis spectra of AuNPs (Figure S2A). The HR-TEM images of 2.4-ratio AuNPs@CNDs (Figure S1C) suggest successful wrapping of AuNP cores by CND structures.

According to Figure S2A, UV-visible absorption spectra of AuNPs confirmed a localized surface plasmon resonance LSPR peak at 540 nm, which indicate the formation of the AuNPs with a size of around 50 nm [116]. The absorption spectrum of CNDs displays a typical peak at 360 nm [117]. The absorption spectrum of AuNPs@CNDs presents both the plasmon absorption peak at 540 nm of the AuNP core [114] and the 360 nm peak for CNDs, corroborating the hybrid composition. Raman spectra of both CNDs and AuNPs@CNDs (Figure S2B) show two distinct peaks at 1340 cm^{-1} and 1590 cm^{-1}. the relative intensity of D and G band (D/G ratio) in Raman spectra of AuNPs@CNDs is equal to 0.780, whereas this ratio is 0.741 for CNDs. The D and G band intensities of AuNPs@CNDs are much higher than that of CNDs, suggesting the enhanced defect effect of AuNPs [118], [119].

SERS spectra of Rh6G (Figure S3) at the concentration of 48×10^{-8} M using AuNPs@CNDs substrates produced from different $HAuCl_4$/CNDs mass ratio shows that the 2.4 ratio hybrid substrate provides the best SERS signal enhancement of Rh6G. Therefore, the mass ratio 2.4 AuNPs@CNDs hybrid substrate is selected for the further investigation and applied in herbicide sensing studies.

Characterization of MPY-functionalized AuNPs@CNDs

To investigate the adsorption of the MPY molecules on AuNPs@CNDs, XPS analysis was carried out as shown in Figure 1A-D. A full survey scan spectrum of the MPY-functionalized AuNPs@CNDs indicates the presence of prominent peak characteristic of O 1s, C 1s, S 2p, N 1s, and Au 4f elements (Figure S4A). In contrast to the spectra of AuNPs@CNDs (red line), the presence of S 1s peak in MPY-functionalized AuNPs@CNDs spectra (black line) primarily confirms the presence of sulfur (S) in the sample. Notably, both modified and unmodified samples show the presence of oxygen, carbon (C), nitrogen (N), and gold (Au) atoms.

High resolution XPS scan spectra of AuNPs@CNDs exhibit three binding energy (BE) windows of C 1s, N 1s, and O 1s, and Au 4f respectively. The N 1s XPS spectra in Figure S4B feature two peaks corresponding to pyridinic nitrogen (398 eV) and pyridone nitrogen (399.6 eV) [120]. The C 1s XPS spectra of AuNPs@CNDs (Figure S4C) show BE peaks at 284.3, 285.4, and 287.5 eV which are attributed to C-C, C-O-C, O-C=O groups, respectively [121]. The deconvoluted O 1s band (Figure S4D) show three peaks centered at 531.4 and 531.9 which represents the C-O and C=O groups, respectively.

The high-resolution scan spectrum representing N 1s peak region of MPY-functionalized AuNPs@CNDs is shown in Figure 1A. The N 1s spectrum has been deconvoluted into 5 peaks. Among them, the peak centered at∼398.8 eV is attributed to the C−N bond associated with the MPY molecule. The other deconvoluted peaks at 399, at 400.6, 401.4 and 401.5 eV are assigned to the deprotonated thione (MPYD, 399 eV) and the protonated thione (MPYH, 400.6 and 401. 5 eV) forms of the MPY molecule, respectively. The above XPS analyses suggest the presence of both the MPYH and MPYD thiolate forms of the MPY molecule that remain adsorbed on the AuNPs@CNDs [122]. Studied showed that in the surface adsorbed state, MPY molecules exist in the MPYH as well as in the MPYD [123], [124].

The C 1s XPS spectra of MPY-functionalized AuNPs@CNDs (Figure 1B) show BE peaks at 284.7, 286.4, and 289.7 eV which originate from C-C, C-O-C, O-C=O groups, respectively. The deconvoluted O 1s band (Figure 1C) show three peaks located at 530.1 and 530.9, and 532.7 eV which represents the C-O and C=O groups, respectively.

The narrow scan deconvoluted XPS spectrum of MPY-functionalized AuNPs@CNDs in the S 2p region (Figure 1D) is characterized by intense and well resolved peak at ~165 eV together with weak but prominent bands centered at 161.7, 163.1, and 163.7eV [125]. The peaks at 161.7 and 165 eV are characteristic of the S $2p_{3/2}$ level, while the peak at 163.7 eV originates from the S $2p_{1/2}$ level of the sulfur atom. The other two peaks at 163 and 163.1 eV are assigned to $2p_{3/2}$ and $2p_{1/2}$ levels of sulfur, respectively [122], [126].

FTIR spectra in Figure 2B provide structural insights into both AuNPs@CNDs and MPY-functionalized AuNPs@CNDs samples. The presence of characteristic surface chemical groups is evident. Broad absorption features around 3400 cm-1 confirm the presence of -OH and -NH_2 groups in both modified and unmodified samples. Strong signal bands around 1750 cm-1 indicate C=O stretching vibrations, revealing carbonyl and carboxyl functional groups arising from the presence of CNDs in the samples. Notably, a weak peak at 2560 cm-1 in the MPY-functionalized-AuNPs@CNDs sample indicates the presence of -SH groups, absent in the AuNPs@CNDs sample, confirming the presence of MPY moieties. Additional signals at 960 cm^{-1} suggest the presence of aromatic structures [127].

The UV-vis adsorption spectra of the as-prepared AuNPs@CNDs and MPY-functionalized AuNPs@CNDs are given in Figure 3. Compared to the as-prepared AuNPs suspension, there is a red-shift of 1 nm in the LSPR band of the modified AuNPs, which is due to higher refractive index of MPY. The absence of peak around 700 nm confirms the absence of aggregation after modifying the surface of AuNPs@CNDs with MPY.

Figure 3-1- (A) N 1s XPS; (B) C1 s XPS; (C) O 1s XPS; (D) S 2p XPS spectra of MPY-functionalized AuNPs@CNDs.

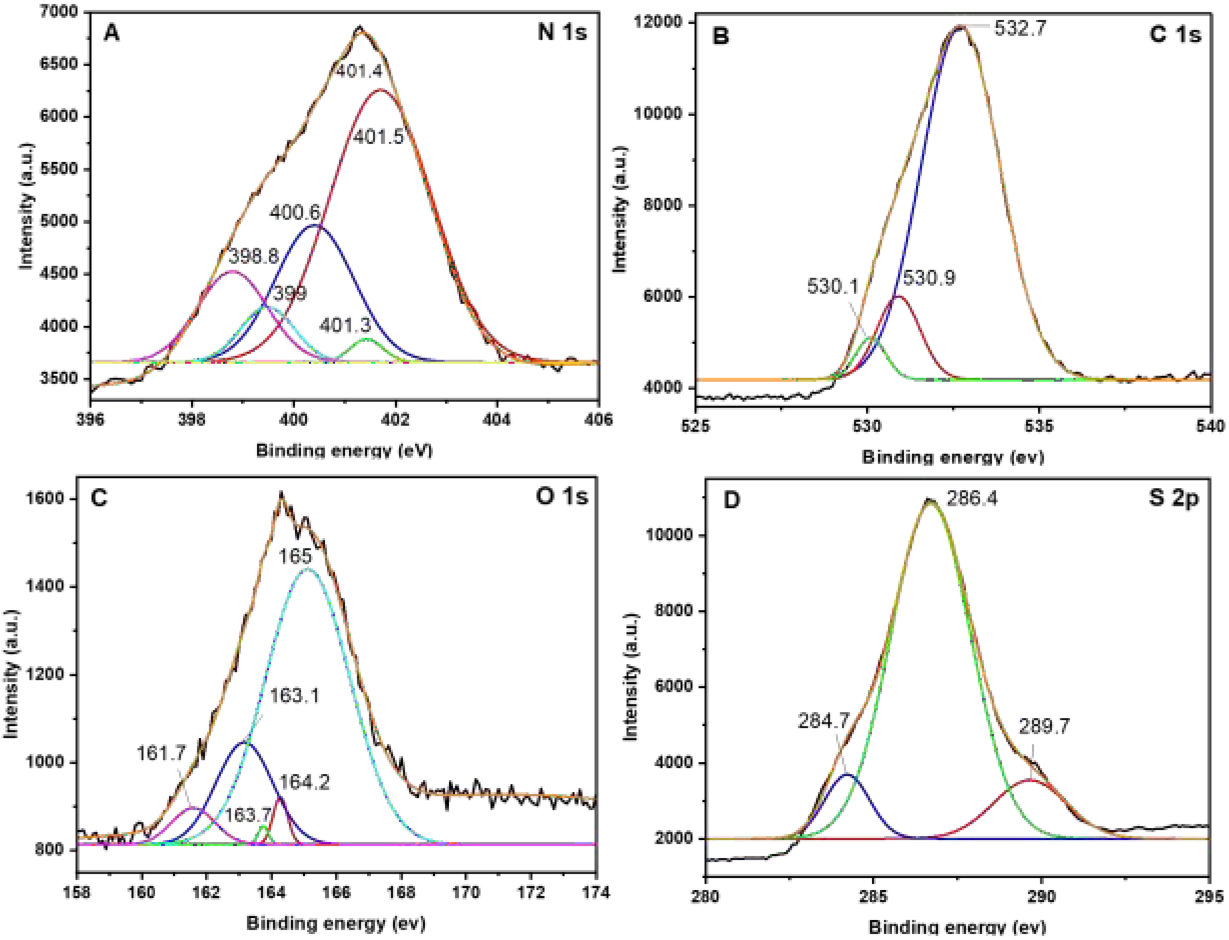

Figure 3-2- (A) Comparing Raman spectra and (B) FTIR spectra of MPY with MPY-functionalized AuNPs@CNDs and AuNPs@CNDs.

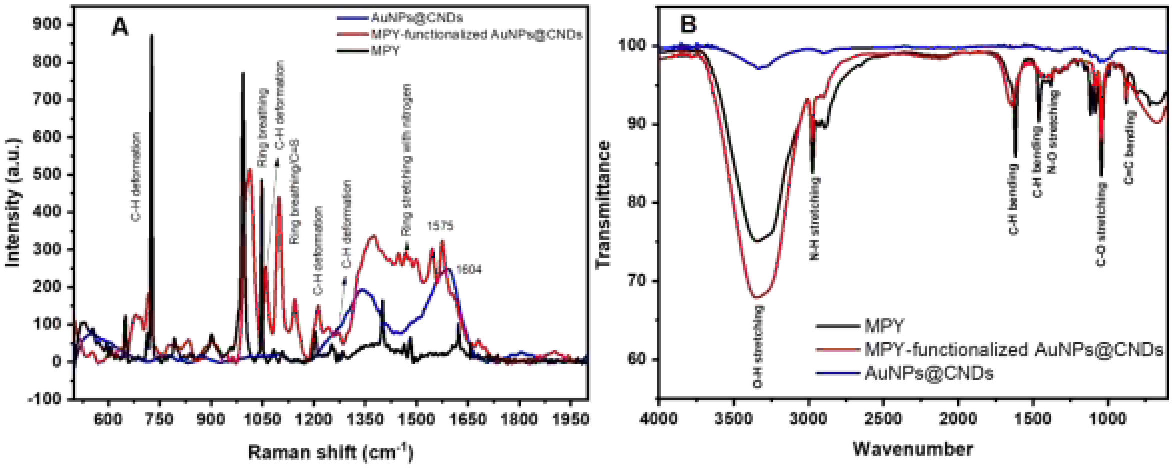

Figure 3-3- UV-Vis spectra of AuNPs@CNDs and MPY-functionalized AuNPs@CNDs.

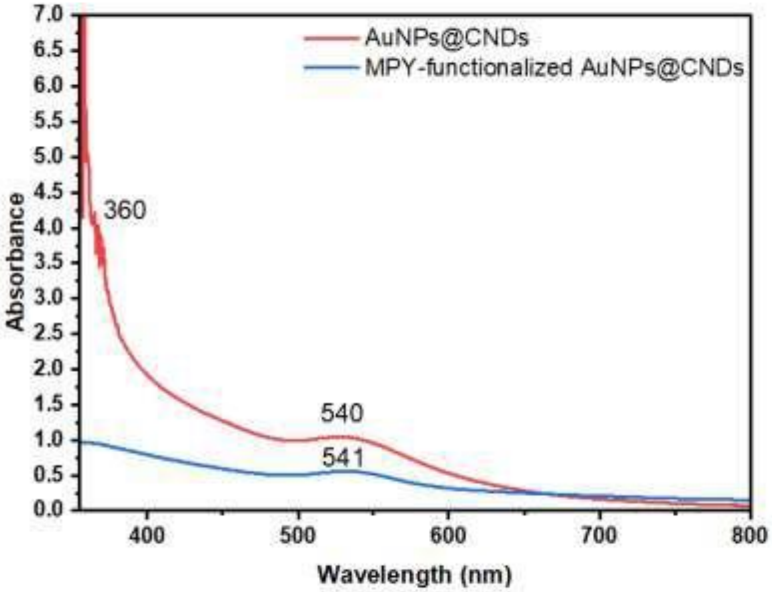

Rh6G measurement by SERS nanosensors

Rh6G with concentration 48×10^{-8}, 48×10^{-9}, and 48×10^{-10} M was selected as a reporter to perform the SERS evaluation on MPY-functionalized AuNPs@CNDs substrates. Based on Figure 4A, the band at 614 cm^{-1} was assigned to C-C-C ring in-plane in xanthene ring, whereas those around 771, 1127, and 1183 cm^{-1} were attributed to C-H ring in xanthene or phenyl ring. The prominent peaks in the range of 1311, 1362, 1507, 1573, and 1650 cm^{-1} were due to the symmetric modes of in-plane C-C stretching vibrations in xanthene or phenyl ring [49], [128]. These results confirm that SERS substrates successfully detected Rh6G in the solution with the characteristics peaks of Rh6G exactly aligned with the reported characteristic peaks [49], [128].

Figure 4A shows that there is an increase in the intensity of all the characteristic Rh6G peaks by increasing the concentration of Rh6G and Rh6G with a low concentration of 48×10^{-10} M can be sensitively detected using colloidal MPY-functionalized AuNPs@CNDs solution. As it can be seen in Figure 4B, by plotting LogI_{1650} (logarithm of SERS peak intensity at 1650 cm^{-1}) versus LogC (logarithm of Rh6G concentration), a linear calibration curve is obtained, where the coefficient of determination (R^2) is 0.996. It demonstrates a linear detector response for the applied Rh6G concentration.

Figure 3-4- (A) Raman spectra of Rh6G with different concentration on MPY-functionalized AuNPs@CNDs nanosensor and (B) Calibration curve.

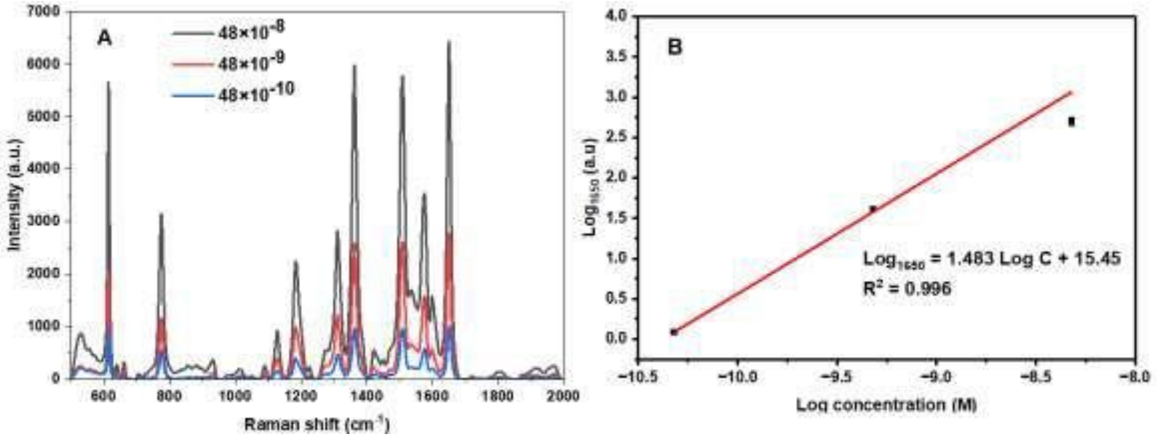

Hg^{2+} detection by SERS nanosensors

In order to determine the length of incubation time needed in the Hg^{2+} solution to reach a constant intensity ratio, a solution of 0.48 μM Hg^{2+} was incubated in the MPY-functionalized AuNPs@CNDs for 0-40 min (Figure S5A). As it can be shown in Figure S5B, the intensity ratio of I_{717}/I_{431} first decreases with increasing incubation time up to 20 min and then becomes constant at about 20 min. Therefore, 20 min was selected as the incubation time in this research. The calibration curve in the Figure 8B is based on the ratio of I_{717}/I_{431} that can be used to determine the concentration of unknown Hg^{2+}.

According to the Figure 5 the change in the SERS spectra of MPY-functionalized AuNPs@CNDs after immersion of nanoparticles in Hg^{2+} solution is observed. There is a decrease in the intensity of most pyridyl-related Raman bands at 1013, 1059, 1097, 1212, and 1575 cm^{-1} and all these bonds are shifted to higher wavenumbers [47], [48], [129]. The isolated Raman peak at 708 cm^{-1} corresponding to the out-of-plane C-H deformation is slightly shifted to the lower frequency and increased in intensity [47], [48], [129]. There is a decrease in the isolated peak at 431 cm^{-1} which is corresponding to the in-plane deformation (C-S)/out-of-plane wagging (C-C-C). Increase in Raman peak at 708 cm^{-1} and redshifts in Raman bands at 1013, 1059, 1097, 1212, 1575, and 1605 cm^{-1} after coordination with Hg^{2+} can confirm more perpendicular orientation of MPY on the AuNPs@CNDs surface [47], [48], [129]. The remarkable frequency shifts and alteration in intensities of Raman peaks in MPY-functionalized AuNPs@CNDs spectrum indicates the redistribution of the electron among different bond within the aromatic ring as a result of coordination of metal ions to the pyridinic nitrogen [48], [130], [131].

Figure 3-5- SERS spectra of MPY-AuNPs@CNDs before (black curve) and after (red curve) exposure to Hg2^{+} (0.48 µM).

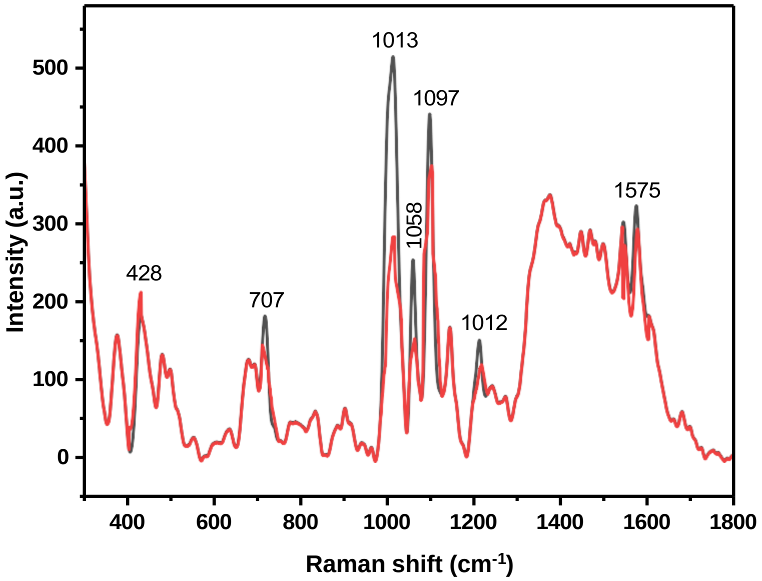

Sensitivity, reproducibility, and selectivity of nanosensors

The sensitive SERS analysis of MPY-functionalized AuNPs@CNDs was investigated after exposing the nanosensors to Hg ions for 20 min while the concentration of Hg^{2+} was varying from 0.05 nM to 0.48 mM (Figure 6). Intensity ratio of I_{717}/I_{431} decrease exponentially with increase in the Hg ions concentration until about 48 µM and then changes slightly. As it can be seen in Figure 7A and B there is a linear relationship for the logarithmic concentration in the range of 0.05 nM to 480 nM. The lowest concentration that our MPY-functionalized AuNPs@CNDs nanosensor can detect is 0.05 nM, which is lower than concentration of Hg^{2+} in drinking water permitted by WHO 30 nM.

Figure 3-6- SERS spectra of nanosensor after exposure to Hg^{2+} for 20 min at the concentrations indicated.

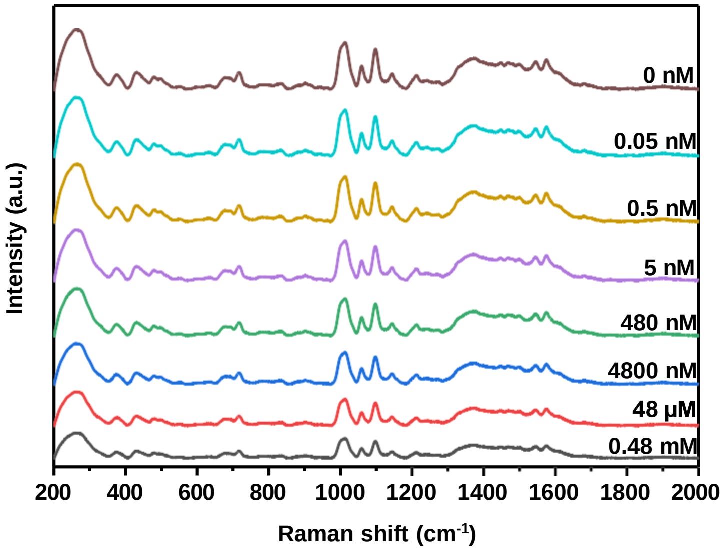

Due to the strong specific binding capability between Hg^{2+} and MPY, the sensor showed a high selectivity and strong anti-interference ability for Hg^{2+} detection. MPY can interact with Hg^{2+} through its pyridyl group. Therefore, upon coordination with mercury, the orientation of the MPY molecules adsorbed on AuNPs@CNDs changes from nominally flat to perpendicular. These results in selective detection of mercury among other heavy metals [47], [129].

Figure 3-7- Calibration curves of nanosensors after exposure to Hg^{2+} concentration, with insets indicating linear plots for concentrations ranging from 0.05 nM to 480 nM for Hg^{2+}.

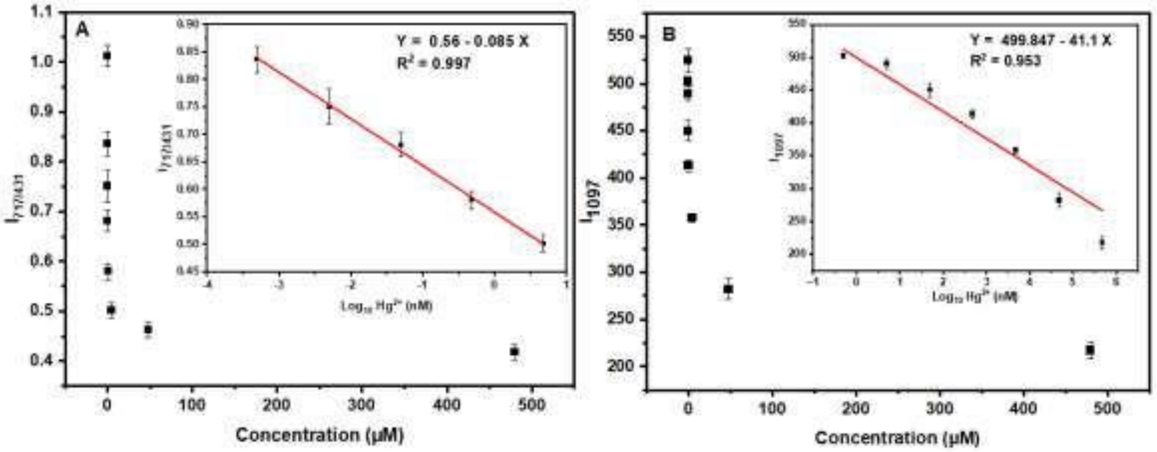

For the batch-to-batch reproducibility, 18 SERS spectra of 0.48 µM Hg^{2+} on 6 different batches of MPY-functionalized AuNPs@CNDs substrates collected from 3 random points in each substrate was captured (Figure 8A). The relative standard deviation (RSD) obtained from the variation in measured peak intensities at 1097 cm^{-1} is 6%, whereas it is 9% for I_{717}/I_{431} which shows acceptable batch reproducibility in Hg^{2+} detection by MPY-functionalized AuNPs@CNDs substrate was acquired (Figure 8C-D).

Several metal ions including Fe^{3+}, Mg^{2+}, Ca^{2+}, Co^{2+}, Cu^{2+}, Zn^{2+}, and Ag^{+} were selected to examine the selectivity of nanosensors. Based on the Figure 8B there is no significant change in the SERS spectra and bar graphs of the corresponding intensity ratio of I_{717}/I_{431} (Figure 8E and C) for 0.48 µM solutions of Fe^{3+}, Mg^{2+}, Ca^{2+}, Co^{2+}, Cu^{2+}, Zn^{2+}, whereas Hg^{2+} caused a decrease in SERS intensity, demonstrating the high selectivity of the nanosensors for Hg^{2+} detection. The sensors capability to sense Hg^{2+} in complex solutions (Fe^{3+}, Mg^{2+}, Ca^{2+}, Co^{2+}, Cu^{2+}, and Zn^{2+}) was also investigated, and the result demonstrated that it was able to detect Ag+ without interference (Figure 9).

Figure 3-8- (A) SERS reproducibility illustrated by SERS spectra acquired on the six random nanosensors on three positions for each sensor; (B) SERS spectra of nanosensors after exposure to mixture of heavy metals; (C) Corresponding bar graphs using intensity of t the 1097 cm^{-1}; (E) Bar graph of the corresponding intensity ratios, I_{717}/I_{431} After exposure to heavy metals. Error bars were estimated from three different sensors.

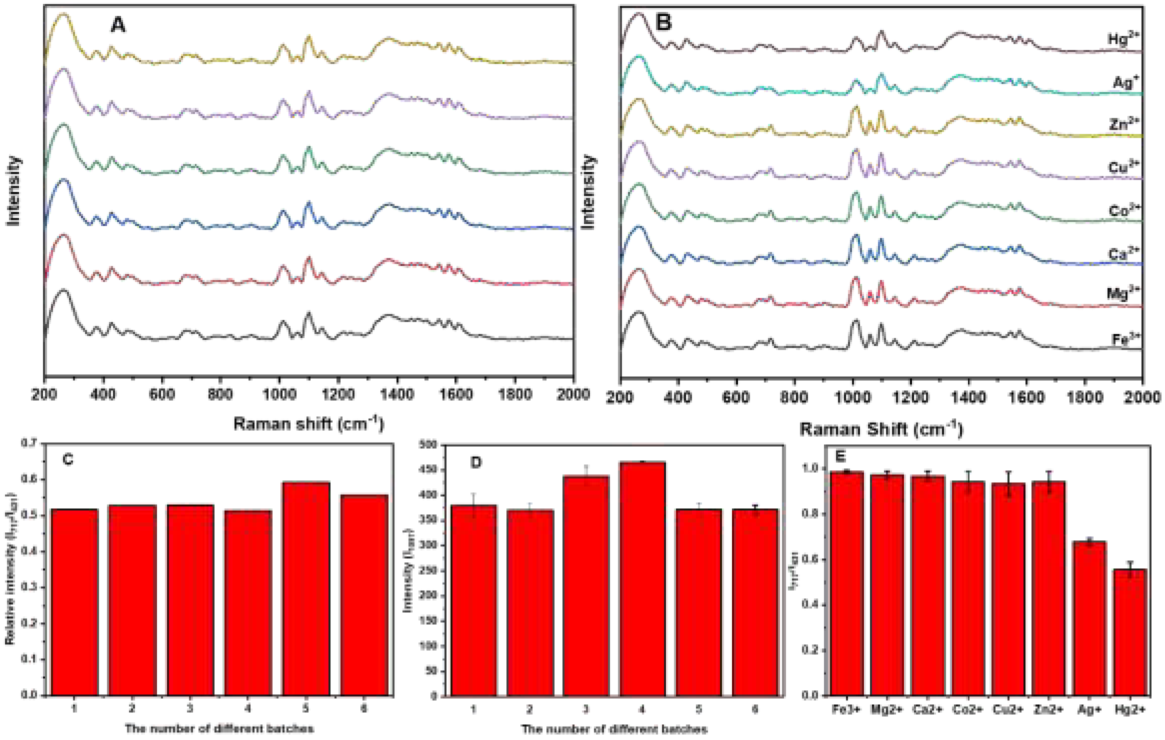

Figure 3-9- Selectivity for mixture of heavy metals. Error bars were estimated from three different sensors.

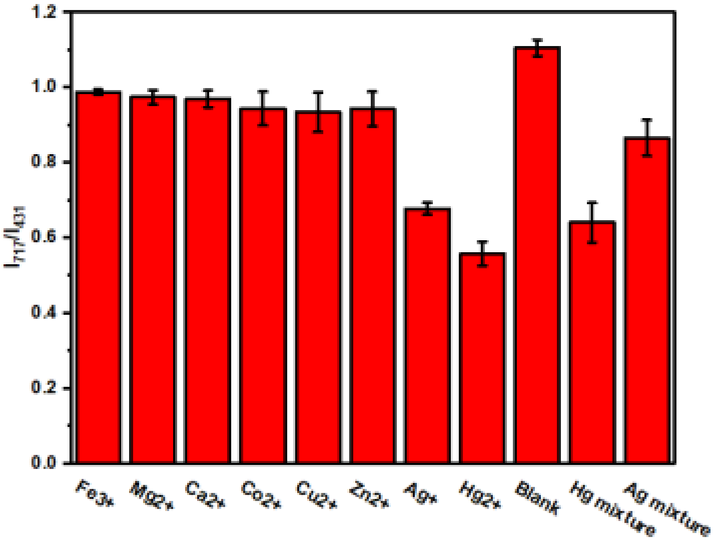

Compared to the reported methods for mercury detection, our SERS method based on MPY-functionalized AuNPs@CNDs, has lower cost, convenience, and rapider determination. In addition, the as prepared SERS substrate has high sensitivity, selectivity, and reproducibility. In the SERS methods reported (Table 1), the some of the AuNPs based SERS probe has good are fast and convenience but they don't have high sensitivity. Based upon the Raman intensity response of polyaniline-nano gold composite to Hg^{2+}, a highly sensitive SERS detection technique was proposed for the quasi-quantitative analysis of mercury in the range of 1–300 nM, with complicated operation. This MPY-functionalized AuNPs@CNDs SERS method is a good SERS quantitative analytical method.

Table 3-1- Comparison of the reported SERS methods for Hg^{2+} detection.

Method	LOD	Linear range	Comments	Reference
SERS using gold substrate	165 nM	-	Convenience and reproducibility	[132]

SERS on silver colloid substrate	50 nM	2.5 – 100 nM	-	[133]
SERS using a roughened silver electrode	63 nM	-	-	[134]
SERS on roughened gold substrate	1000 nM	-	-	[135]
SERS on AuNPs@CNDs	0.05 nM	0.05 – 4800 nM	High sensitivity and selectivity, convenience, and reproducible	This work
Au/polyaniline	0.01 nM	No linear, quasi-quantitative analysis	Highly sensitive, but complicated	[136]
AuNP on glass slide	50 nM	No linear, quasi-quantitative analysis	Doubly labeled, complicated	[137]

Detection of mercury in simulated water and recovery experiments

To test the capability of using the MPY-functionalized AuNPs@CNDs as Raman probe for mercury detection, we spiked the mercury sample into simulated water and obtained the SERS spectra to evaluate the recovery rate. In these experiments, three distinct concentration levels at low (0.05 M), medium (0.5 M), and high (5 M) concentrations were prepared, and the SERS spectra were obtained (Figure S6). Based on the Raman signal intensity at the marker peak of I_{717}/I_{431}, we measured concentrations according to the calibration curves in Figure 7. The recovery percentage of known amounts of spiked mercury in simulated water were calculated with respect the spiked concentration and reported in Table 2. The results indicate that the recovery rate at medium and high levels is > 100%, higher than the lower (98%). These results demonstrate the effectiveness using the MPY-functionalized AuNPs@CNDs for detection of mercury in simulated water.

Table 3-2- Recovery (%) of mercury in simulated water samples.

Sample	Hg^{2+} added/nM	Hg^{2+}found/nM	Recovery/%
1	0.05	0.049	98 ± 2.1
2	0.5	0.512	102.4 ± 1.42
3	5	5.018	100.6 ± 3.15

Conclusion

In conclusion, we have investigated the application of a sensitive and selective SERS sensor for Hg^{2+} detection by using MPY-Functionalized AuNPs@CNDs. A series of aqueous solution with different mercury concentrations was applied to calibrate Hg^{2+} sensor. A wide linear concentration was observed from 0.05 nm to 0.48 µM. The lowest concentration detected for Hg^{2+} was as low as 0.05 nM, which is lower than the maximum level in drinking water permitted by WHO and EPA. The results demonstrate that this chemical sensor has excellent selectivity for Hg^{2+} between other common metal ions in water. In addition, we applied the sensor for Hg^{2+} detection in simulated water samples with excellent recoveries (98−100.6%). This SERS sensor has the advantage of simplicity, high selectivity, signal reproducibility and repeatability, and high sensitivity, which has great practical potentials for on-site Hg^{2+} detection in various environments.

CHAPTER VI: HYPERSPECTRAL IMAGING OF NANOPARTICLES IN THE PLANT CELL

Introduction

Determining the localization and characteristics of nanoparticles inside cells for sensing application, cancer therapy, and nanomedicine is very important [138], [139]. Various macroscopic and spectroscopic techniques, including scanning electron microscopy (SEM) [140], [141], transition electron microscopy (TEM) [142], [143], fluorescence imaging [144], and etc., have been developed currently for detection and visualization of nanoparticles inside cells. However, methods such as TEM are costly and required complicated sample preparation [145]. SEM technique is simple, but it can image only the surface of cells [146] and fluorescence imaging require addition of tags onto nanoparticles, which require a system capable of super resolution imaging [144]. Among these methods, hyperspectral-enhanced dark field microscopy (HEDFM) enables direct optical observation of nano-scale entities in a wide range of transparent and translucent sample environments, without the need of labels or other markers [147], [148]. HEDFM provides high signal-to-noise images (up to ten times higher than that of other optical instruments), which is because of maximum photon density focused on the sample coming from a unique light path design [149]. This high-performance capability provides users with both good images as well as allowing establishing techniques, such as Raman and hyperspectral microscopy to be applied in new and exciting ways [139], [150].

The hyperspectral imaging is based on the plasmonic shifts occurring because of the interaction of nanoparticles with the surrounding medium [139], [151]. Most important optical properties of plasmonic materials including gold nanoparticles are localized surface plasmon resonance (LSPR) which is influenced by microenvironment providing information on region where nanoparticles are distributed [152]. When a hyperspectral image is captured in this darkfield optical mode, every nanoscale pixel in the hyperspectral image contains the spectral response of that pixel's spatial area [147], [150], [153]. This enables spectral identification of the nanoparticles for spectral mapping in the cell structure [147].

Dark-field microscopy may substitute more expensive and sophisticated microscopy techniques, such as SEM and TEM for rapid and sensitive identification of nanoparticles in in environmental samples (sediments, wastewater, soil, etc.) [154]–[157] and biological specimens (tissues organisms and cells) [158], [159]. So far different types of specimens have been imaged in dark-field mode, including plant tissue specimens [160], microbial biofilms [161], surface-attached human cells [162], suspended mammal cells [163] and etc.,. In general, sample preparation of enhanced dark-field microscopy does not require any specific stains or fluorescent markers and its simple that can be applied to detect nanoparticle on different kinds of specimens [164].

Our aim is to study the effectiveness of HEDFM for visualization cell specimen. We selected AuNPs and AuNPs@CNDs as a candidate for HEDFM evaluation owing to their unique plasmonic properties. We reported for the first-time nano hybrid AuNPs@CNDs for HEDFM evaluation in cell specimen. This study will pave the way for applying HEDFM using hybrid plasmonic sensors in environmental samples and biological specimens for detection and visualization.

Sample preparation

50 µL of AuNPs or AuNPs@CNDs aqueous suspension (50 nm, 0.0585 mg mL^{-1}) was dropped carefully on the surface of thoroughly washed organic spinach, (purchase from a local LIDL grocery) and samples where dried for an hours. Then the samples were washed with distilled water two time and dried with pure nitrogen flow before HEDFM imaging. The dried

samples were hold between to cover glass slides and the two cover glass slides were hold together with tape carefully. For the spectral profile of CGA77102 herbicide (S-metolachlor 86.6% by weight), different concentrations of herbicides (10^{-3}, 10^{-5}, and 10^{-7} M) was prepared and spiked on the spinach surface after about 12 hours, AuNPs@CNDs was dropped on the surface of samples and let it dry Sbefore Hyperspectral imaging.

Hyperspectral imaging system

Cytoviva hyperspectral imaging system was used to capture hyperspectral images (HSIs) of AuNPs and AuNPs@CNDs on the spinach leaves. This system provides a high-resolution dark-field-based optical microscope combined with a photospectrometer for spectral characterization and spectral mapping at the nanoscale. AuNPs are brighter in HIS images and can be characterized by studying their spectral information. The LSPR properties of AuNPs in the biological environment can be measured to determine and identify spatial distributions in cells without damaging the sample [165].

The exposure time for each spectral area was set to 0.2-0.3 ms. The desired area was scanned at 700 × 700 pixel resolution. ENVI 4.8 software was used for processing the collected spectral data. The desired regions of interest (ROIs) were chosen, and the mean spectral data were collected for approximately 70–100 pixels.

In experimental measurement, unpolarized plain light (broad band) from a halogen lamp was used as incident light to illuminate the nanoparticle samples from the bottom. The transmitting light signal captured by a 50 and 100 × objective lens is then collected using in a darkfield CytoViva hyperspectral imaging system.

Results and discussion

Figure 4.1 A-C shows dark field (DK) images of spinach, AuNPs and AuNPs@CNDs on spinach. Due to the dark background, the NPs are bright and easy to visualize. As shown in the DK images, nanoparticles were localized randomly on the wall and center of spinach cells. The distribution patterns of the AuNPs and AuNPs@CNDs in spinach cells were similar. As we compared the DK imaging of spinach and AuNPs and AuNPs@CNDs on spinach, we observed that we can easily distinguish between the wall and cells of plant tissues when the spinach is exposed to NPs. These images indicate cellular uptake of NPs on center and wall of NPs with approximately uniform distribution and no aggregation. These scientific finding indicate that we can apply the NPs on the surface of plant cells including spinach to monitor the existence of toxic material on the plant cell, which is a promising step for detecting and analyzing the toxic materials remains on the surface of plant cells.

Figure 1D-F shows the spectral profile of Spinach, AuNPs, and AuNPs@CNDs. According to figure 1E, the peak at around 550 nm is corresponding to the SPR of AuNPs and confirm that the SPR of AuNPs occurs at around 540 nm. It is noteworthy that the peak around 580 nm can be attributed to the SPR of aggregation of group of AuNPs. The intensities of SPR peaks of AuNPs@CNDs are much higher than that of AuNPs, suggesting the enhancement effect of AuNPs@CNDs. A new resonant mode located at 615 nm appeared after AuNPs is covered by CNDs, this is probably because of coupling between AuNPs and CNDs. These figures indicate that Cytoviva hyperspectral imaging techniques is a very accurate techniques that can monitor the plasmonic picks of NPs absorbed on the surface of plant cells. We were able to distinguish between the AuNPs and AuNPs@CNDs plasmonic based on the spectral profile of NPs on spinach, while the spectral profile of spinach was captured as reference and did not show any plasmonic peaks. This step is very important to monitor what kinds of NPs ae absorbed on the surface of plant cells based on their plasmonic peaks.

Figure 4-1- Dark field image of (A) spinach, (B) AuNPs on spinach, (C) AuNPs@CNDs on spinach. Spectral profile of (D) spinach, (E) AuNPs on spinach, (F) AuNPs@CNDs on spinach.

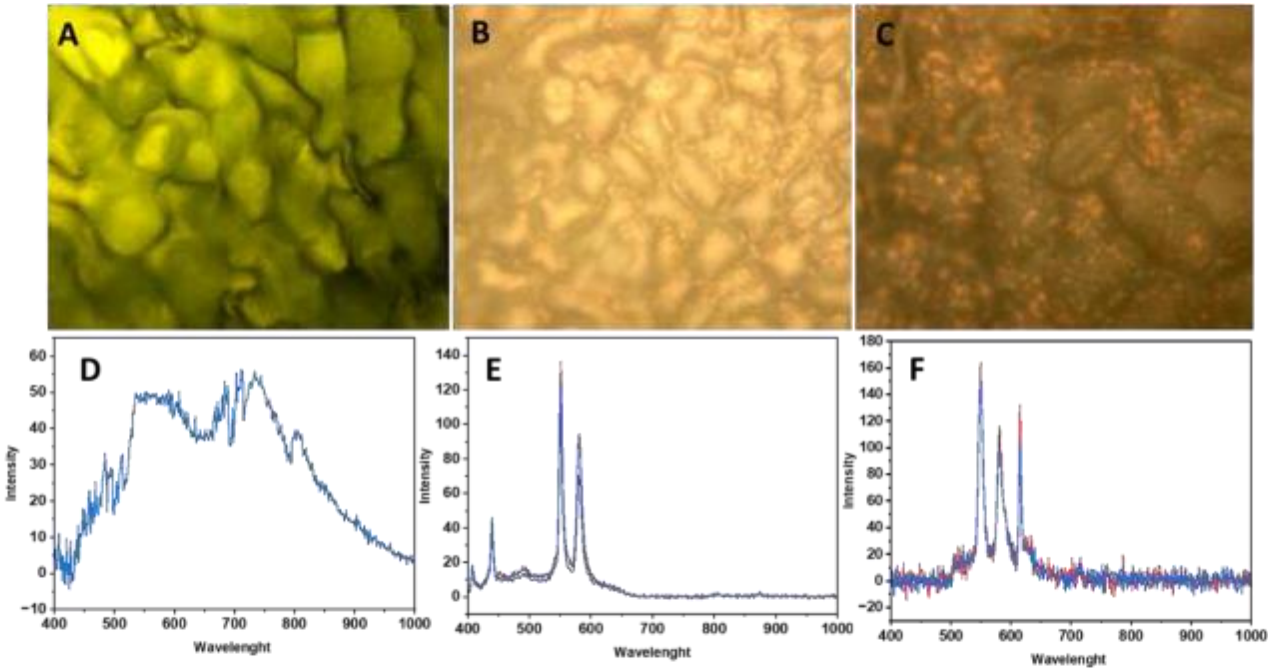

Figure **4.1 A-B** shows the DK image and hyperspectral image of CGA77102 herbicide spiked (10^{-3} M) on spinach afteradding AuNPs@CNDs on spinach surface, respectively. Figure C shows the region of interest for 10^{-3} M herbicide spiked on the surface of spinach afteradding AuNPs@CNDs on the cell surface. The spectra profile of CGA77102 with different concentrations (10^{-3}, 10^{-5}, and 10^{-7} M) (Figure D) indicate the signal intensity decline along with decreasing concentration. The spectra profile of herbicide indicates the chemical fingerprint of selected herbicides.

Figure 4-2- Dark field image of CGA77102 herbicide on spinach (A), Hyperspectral image of CGA77102 herbicide on spinach (B), Spectral profile of CGA77102 herbicide on spinach (C), and region of interest for figure C (D). Raman spectra of 10-3 M CGA77102 herbicide (E).

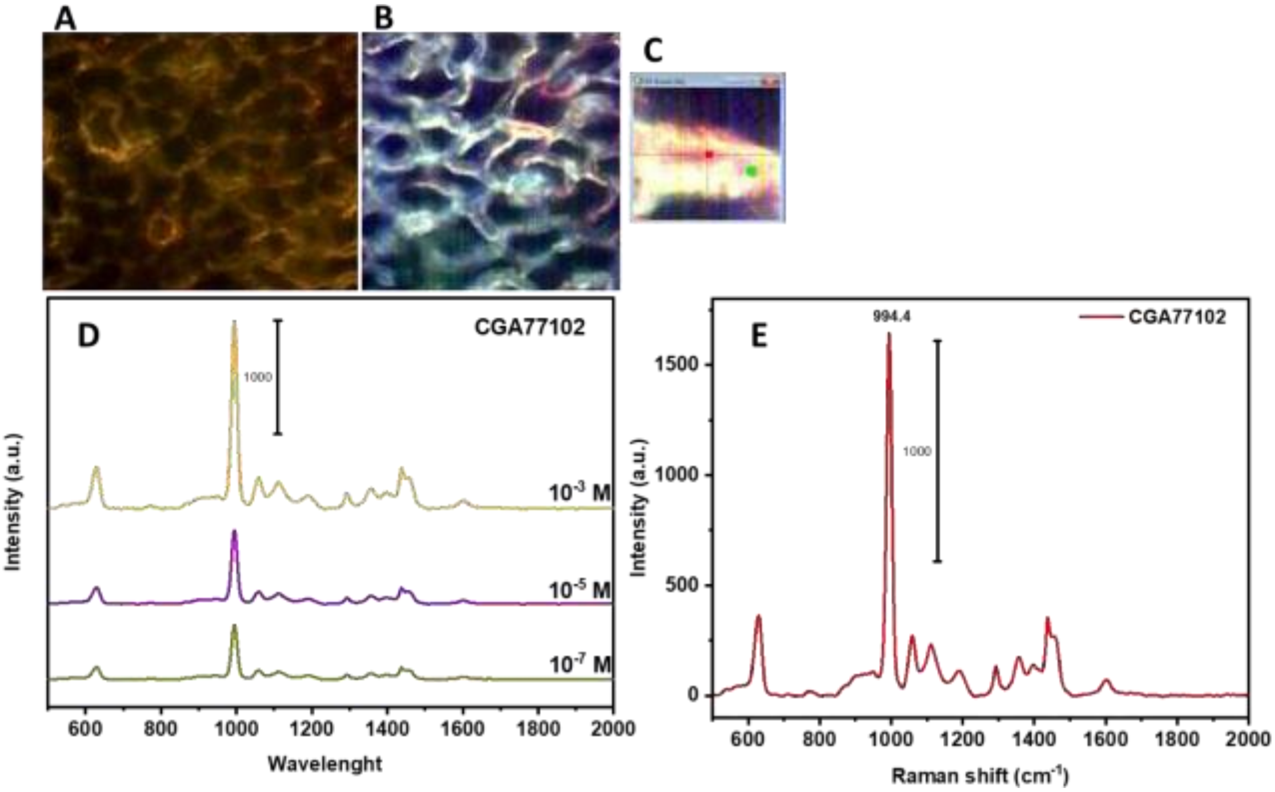

According to Figure **4.2 A-D**, our AuNPs@CNDs is a very sensitive sensor that can detect the toxic materials, including herbicide on the surface of plant cells, including spinach. The high signal intensity and the accurate fingerprint of herbicide detected by our nanostructured SERS substrate is very important in detecting herbicide at very low concentration in the range of 10^{-7} M. The spectral profile of CGA77102 recorded by Cytoviva hyperspectral imaging was compared with Raman spectra of herbicide at the same concentration recorded on glass slide and confirm that in both graphs, the peak at 994.4 is the characteristic Raman peak with the highest signal. We observed an increase in signal intensities of all the characteristics peaks of herbicides by increasing the concentration of herbicides, which indicate the accuracy of our nano sensor for sensing different concentrations of herbicides on the surface of spinach plant cell.

Conclusion

To improve fundamental knowledge in bio-nano-interaction, novel imaging techniques are needed for diagnostic and therapeutic levels. The HEDFM presents easy and rapid analysis of nanomaterials in various environmental samples. This research shows that, AuNPs and AuNPs@CNDs with well-defined optical properties, are good for HEDFM imaging. We were able to detect the herbicide using cytoviva hyperspectral. As a final remark, we anticipate that the HEDFM technology will provide wide range of opportunities for bionanotechnological development in modern health sciences.

CHAPTER V: CONCLUSIONS

In chapter II, AuNPs@CNDs SERS with spherical shape of AuNPs with a size of approximately 50 nm, was synthesized with the optimized CNDs/$HAuCl_4$ mass ratio of 2.4, which was confirmed that, for the mass ratio of 2.4, the AuNPs@CNDs have spherical shape, and the NPs are not agglomerated and more uniformly distributed compared to other mass ratios. The SERS substrate was served as a sensor for rapid and sensitive detection of Rh6G with concentration in the range of 48×10^{-12} M (48×10^{-3} nM). Improvement in SERS activity was due to combination of chemical and electromagnetic mechanism, which can be attributed to the efficient transfer of electrons from the carbon nanomaterial to gold nanoparticle in addition to the electromagnetic field enhancement via effective plasmonic propagation and the formation of localized hotspots under light illumination. The prepared AuNPs@CNDs substrates produce highly enhanced Raman signal with excellent signal uniformity compared to AuNPs or CNDs alone. The AuNPs@CNDs shows remarkable key parameters of SERS sensor including, repeatability, reproducibility, and stability, which provide the promising application of SERS sensor for ultra-sensitive determination of organic compounds in water and food for the future.

Chapter III demonstrates a sensor based on AuNPs@CNDs modified with MPY. The sensor was very selective for mercury detection in water. The sensor exhibited good selectivity for Hg^{2+} detection compared with other common metal ions in water. The sensor detects Hg^{2+} with a concentration as low as 0.05 nM. In the future, our SERS-based sensor can apply for sensitive and selective detection of heavy metal in cancer cells including breast cancer cells.

The primary purpose of the whole project was to investigate state-of-the-art SERS application of hybrid materials based on carbon nanotubes and gold nanoparticles, and to get a comprehensive understanding of the role SERS enhancement. To this end, the compelling findings in this dissertation presented some advances in knowledge and technical methods for development of hybrid nanoelectrodes based on carbon materials and gold nanoparticles as SERS detection of toxic materials. Future work could further investigation of SERS sensor for biomolecular detection, as well as incorporating other active species and engineering their interface to accelerate charge transport and improve SERS activity. For practical applications, continuous efforts of the research communities should be made on exploring advanced application of hybrid materials and device engineering. It is highly likely to develop SERS substrate for demonstrated its potential application for environmental water on-site monitoring.

REFRENCES

[1] H. Malekzad *et al.*, “Noble metal nanostructures in optical biosensors: Basics, and their introduction to anti-doping detection,” *TrAC Trends Anal. Chem.*, vol. 100, pp. 116–135, 2018, doi: https://doi.org/10.1016/j.trac.2017.12.006.

[2] J. Butet, P.-F. Brevet, and O. J. F. Martin, “Optical Second Harmonic Generation in Plasmonic Nanostructures: From Fundamental Principles to Advanced Applications,” *ACS Nano*, vol. 9, no. 11, pp. 10545–10562, Nov. 2015, doi: 10.1021/acsnano.5b04373.

[3] E. Petryayeva and U. J. Krull, “Localized surface plasmon resonance: Nanostructures, bioassays and biosensing—A review,” *Anal. Chim. Acta*, vol. 706, no. 1, pp. 8–24, 2011, doi: https://doi.org/10.1016/j.aca.2011.08.020.

[4] P. Vítek, K. Novotná, P. Hodaňová, B. Rapantová, and K. Klem, “Detection of herbicide effects on pigment composition and PSII photochemistry in Helianthus annuus by Raman spectroscopy and chlorophyll a fluorescence,” *Spectrochim. Acta Part A Mol. Biomol. Spectrosc.*, vol. 170, pp. 234–241, 2017, doi: https://doi.org/10.1016/j.saa.2016.07.025.

[5] M.-L. Xu, Y. Gao, X. X. Han, and B. Zhao, “Detection of Pesticide Residues in Food Using Surface-Enhanced Raman Spectroscopy: A Review,” *J. Agric. Food Chem.*, vol. 65, no. 32, pp. 6719–6726, Aug. 2017, doi: 10.1021/acs.jafc.7b02504.

[6] Á. I. López-Lorente, “Recent developments on gold nanostructures for surface enhanced Raman spectroscopy: Particle shape, substrates and analytical applications. A review,” *Anal. Chim. Acta*, vol. 1168, p. 338474, 2021, doi: https://doi.org/10.1016/j.aca.2021.338474.

[7] G. Xiao, Y. Li, W. Shi, L. Shen, Q. Chen, and L. Huang, “Highly sensitive, reproducible and stable SERS substrate based on reduced graphene oxide/silver nanoparticles coated weighing paper,” *Appl. Surf. Sci.*, vol. 404, pp. 334–341, 2017, doi: https://doi.org/10.1016/j.apsusc.2017.01.231.

[8] B. Sharma *et al.*, “High-performance SERS substrates: Advances and challenges,” *MRS Bull.*, vol. 38, no. 8, pp. 615–624, 2013, doi: 10.1557/mrs.2013.161.

[9] J. Zhao, A. Das, G. C. Schatz, S. G. Sligar, and R. P. Van Duyne, “Resonance Localized Surface Plasmon Spectroscopy: Sensing Substrate and Inhibitor Binding to Cytochrome P450,” *J. Phys. Chem. C*, vol. 112, no. 34, pp. 13084–13088, Aug. 2008, doi: 10.1021/jp801719c.

[10] X. X. Han, R. S. Rodriguez, C. L. Haynes, Y. Ozaki, and B. Zhao, “Surface-enhanced Raman spectroscopy,” *Nat. Rev. Methods Prim.*, vol. 1, no. 1, p. 87, 2022, doi: 10.1038/s43586-021-00083-6.

[11] M. Fleischmann, P. J. Hendra, and A. J. McQuillan, “Raman spectra of pyridine adsorbed at a silver electrode,” *Chem. Phys. Lett.*, vol. 26, no. 2, pp. 163–166, 1974, doi: https://doi.org/10.1016/0009-2614(74)85388-1.

[12] D. L. Jeanmaire and R. P. Van Duyne, “Surface raman spectroelectrochemistry: Part I. Heterocyclic, aromatic, and aliphatic amines adsorbed on the anodized silver electrode,” *J. Electroanal. Chem. Interfacial Electrochem.*, vol. 84, no. 1, pp. 1–20, 1977, doi: https://doi.org/10.1016/S0022-0728(77)80224-6.

[13] J. I. Gersten, R. L. Birke, and J. R. Lombardi, “Theory of Enhance I Light Scattering from Molecules Adsorbed at the Metal-Solution Interface,” *Phys. Rev. Lett.*, vol. 43, no. 2, pp. 147–150, Jul. 1979, doi: 10.1103/PhysRevLett.43.147.

[14] M. G. Albrecht and J. A. Creighton, "Anomalously intense Raman spectra of pyridine at a silver electrode," *J. Am. Chem. Soc.*, vol. 99, no. 15, pp. 5215–5217, Jun. 1977, doi: 10.1021/ja00457a071.

[15] D. Radziuk and H. Moehwald, "Prospects for plasmonic hot spots in single molecule SERS towards the chemical imaging of live cells," *Phys. Chem. Chem. Phys.*, vol. 17, no. 33, pp. 21072–21093, 2015, doi: 10.1039/C4CP04946B.

[16] S. L. Kleinman, R. R. Frontiera, A.-I. Henry, J. A. Dieringer, and R. P. Van Duyne, "Creating, characterizing, and controlling chemistry with SERS hot spots," *Phys. Chem. Chem. Phys.*, vol. 15, no. 1, pp. 21–36, 2013, doi: 10.1039/C2CP42598J.

[17] Z. Li *et al.*, "High-performance SERS substrate based on hybrid structure of graphene oxide/AgNPs/Cu film@pyramid Si," *Sci. Rep.*, vol. 6, no. 1, p. 38539, 2016, doi: 10.1038/srep38539.

[18] M. Rycenga, P. H. C. Camargo, W. Li, C. H. Moran, and Y. Xia, "Understanding the SERS Effects of Single Silver Nanoparticles and Their Dimers, One at a Time," *J. Phys. Chem. Lett.*, vol. 1, no. 4, pp. 696–703, 2010, doi: 10.1021/jz900286a.

[19] F. Fu *et al.*, "Biomimetic synthesis of 3D Au-decorated chitosan nanocomposite for sensitive and reliable SERS detection," *Chem. Eng. J.*, vol. 392, p. 123693, 2020, doi: https://doi.org/10.1016/j.cej.2019.123693.

[20] K.-M. Lee *et al.*, "Rapid detection and prediction of chlortetracycline and oxytetracycline in animal feed using surface-enhanced Raman spectroscopy (SERS)," *Food Control*, vol. 114, p. 107243, 2020, doi: https://doi.org/10.1016/j.foodcont.2020.107243.

[21] W. Li, X. Zhao, Z. Yi, A. M. Glushenkov, and L. Kong, “Plasmonic substrates for surface enhanced Raman scattering,” *Anal. Chim. Acta*, vol. 984, pp. 19–41, 2017, doi: https://doi.org/10.1016/j.aca.2017.06.002.

[22] H. Li *et al.*, “SERS-activated platforms for chemical contaminants in food: Probes, encoding methods, and detection,” *TrAC Trends Anal. Chem.*, vol. 169, p. 117365, 2023, doi: https://doi.org/10.1016/j.trac.2023.117365.

[23] D. Lin, S. Qiu, Y. Chen, S. Feng, and H. Zeng, “Chapter 11 - Multivariate approaches for SERS data analysis in clinical applications,” Y. B. T.-P. and C. D. A. of S.-E. R. S. Wang, Ed. Elsevier, 2022, pp. 395–431.

[24] B. P. Nanda, P. Rani, P. Paul, Aman, G. Subrahmanya S, and R. Bhatia, “Recent Trends and Impact of Localized Surface Plasmon Resonance (LSPR) and Surface-Enhanced Raman Spectroscopy (SERS) in Modern Analysis,” *J. Pharm. Anal.*, 2024, doi: https://doi.org/10.1016/j.jpha.2024.02.013.

[25] N. John and A. T.M, “New trends in gold nanostructure-based SERS substrate: From fundamental to biomedical applications,” *Vib. Spectrosc.*, vol. 124, p. 103477, 2023, doi: https://doi.org/10.1016/j.vibspec.2022.103477.

[26] B. Sharma, R. R. Frontiera, A.-I. Henry, E. Ringe, and R. P. Van Duyne, “SERS: Materials, applications, and the future,” *Mater. Today*, vol. 15, no. 1, pp. 16–25, 2012, doi: https://doi.org/10.1016/S1369-7021(12)70017-2.

[27] J. Langer *et al.*, “Present and Future of Surface-Enhanced Raman Scattering,” *ACS Nano*, vol. 14, no. 1, pp. 28–117, Jan. 2020, doi: 10.1021/acsnano.9b04224.

[28] F. Svedberg, Z. Li, H. Xu, and M. Käll, “Creating Hot Nanoparticle Pairs for Surface-Enhanced Raman Spectroscopy through Optical Manipulation,” *Nano Lett.*, vol. 6, no. 12, pp. 2639–2641, Dec. 2006, doi: 10.1021/nl062101m.

[29] C. Li, P. Fan, A. Liang, and Z. Jiang, “Using Ca-doped carbon dots as catalyst to amplify signal to determine ultratrace thrombin by free-label aptamer-SERS method,” *Mater. Sci. Eng. C*, vol. 99, pp. 1399–1406, 2019, doi: https://doi.org/10.1016/j.msec.2019.02.080.

[30] X. Feng, C. Li, A. Liang, Y. Luo, and Z. Jiang, “Doped N/Ag Carbon Dot Catalytic Amplification SERS Strategy for Acetamiprid Coupled Aptamer with 3,3’-Dimethylbiphenyl-4,4’-diamine Oxidizing Reaction,” *Nanomaterials (Basel, Switzerland)*, vol. 9, no. 3. Key Laboratory of Ecology of Rare and Endangered Species and Environmental Protection (Guangxi Normal University), Ministry of Education, Guilin 541004, China. fxz97118@guet.edu.cn., 2019, doi: 10.3390/nano9030480.

[31] Y. Fan *et al.*, “Honeycomb architecture of carbon quantum dots: a new efficient substrate to support gold for stronger SERS,” *Nanoscale*, vol. 4, no. 5, pp. 1776–1781, 2012, doi: 10.1039/C2NR12015A.

[32] J. Jin *et al.*, “Precisely Controllable Core–Shell Ag@Carbon Dots Nanoparticles: Application to in Situ Super-Sensitive Monitoring of Catalytic Reactions,” *ACS Appl. Mater. Interfaces*, vol. 8, no. 41, pp. 27956–27965, Oct. 2016, doi: 10.1021/acsami.6b07807.

[33] L. Wang, C. Li, Y. Luo, and Z. Jiang, “Preparation of Highly Catalytic N-Doped Carbon Dots and Their Application in SERS Sulfate Sensing,” *Materials (Basel, Switzerland)*, vol. 11, no. 9. School of Food and Bioengineering, Hezhou University, Hezhou 542899, China. 18074841309@163.com., 2018, doi: 10.3390/ma11091655.

[34] R. Das, S. Parveen, A. Bora, and P. K. Giri, "Origin of high photoluminescence yield and high SERS sensitivity of nitrogen-doped graphene quantum dots," *Carbon N. Y.*, vol. 160, pp. 273–286, 2020, doi: https://doi.org/10.1016/j.carbon.2020.01.030.

[35] J. Ju, W. Liu, C. M. Perlaki, K. Chen, C. Feng, and Q. Liu, "Sustained and Cost Effective Silver Substrate for Surface Enhanced Raman Spectroscopy Based Biosensing," *Sci. Rep.*, vol. 7, no. 1, p. 6917, 2017, doi: 10.1038/s41598-017-07186-9.

[36] J. Yang, L. Xia, Z. Lin, Z. Tang, G. Li, and Y. Hu, "Core (Au)-shell (Ag) structure nitrogen dots for the recognition of nitroaniline isomers by surface-enhanced Raman scattering," *Chinese Chem. Lett.*, vol. 30, no. 3, pp. 638–642, 2019, doi: https://doi.org/10.1016/j.cclet.2018.08.004.

[37] D.-J. Lee and D. Y. Kim, "Hydrophobic Paper-Based SERS Sensor Using Gold Nanoparticles Arranged on Graphene Oxide Flakes," *Sensors*, vol. 19, no. 24. 2019, doi: 10.3390/s19245471.

[38] Q. Huang *et al.*, "A sensitive and reliable dopamine biosensor was developed based on the Au@carbon dots–chitosan composite film," *Biosens. Bioelectron.*, vol. 52, pp. 277–280, 2014, doi: https://doi.org/10.1016/j.bios.2013.09.003.

[39] X. Su, X. Chen, C. Sun, B. Zhao, and W. Ruan, "[Preparation of Au Nanoparticles with Different Morphologies and Study of Their Property as Surface Enhanced Raman Scattering Substrates]," *Guang Pu Xue Yu Guang Pu Fen Xi*, vol. 37, no. 1, pp. 7–12, 2017, [Online]. Available: http://europepmc.org/abstract/MED/30192456.

[40] X. X. Han, W. Ji, B. Zhao, and Y. Ozaki, "Semiconductor-enhanced Raman scattering: active nanomaterials and applications," *Nanoscale*, vol. 9, no. 15, pp. 4847–4861, 2017, doi: 10.1039/C6NR08693D.

[41] T. Li, S. Dong, and E. Wang, “Label-Free Colorimetric Detection of Aqueous Mercury Ion (Hg2+) Using Hg2+-Modulated G-Quadruplex-Based DNAzymes,” *Anal. Chem.*, vol. 81, no. 6, pp. 2144–2149, Mar. 2009, doi: 10.1021/ac900188y.

[42] X. Guo *et al.*, “Recyclable Raman chip for detection of trace Mercury ions,” *Chem. Eng. J.*, vol. 390, p. 124528, 2020, doi: https://doi.org/10.1016/j.cej.2020.124528.

[43] A. Aliberti, P. Vaiano, A. Caporale, M. Consales, M. Ruvo, and A. Cusano, “Fluorescent chemosensors for Hg2+ detection in aqueous environment,” *Sensors Actuators B Chem.*, vol. 247, pp. 727–735, 2017, doi: https://doi.org/10.1016/j.snb.2017.03.026.

[44] F. Cai, Q. Zhu, K. Zhao, A. Deng, and J. Li, “Multiple Signal Amplified Electrochemiluminescent Immunoassay for Hg2+ Using Graphene-Coupled Quantum Dots and Gold Nanoparticles-Labeled Horseradish Peroxidase,” *Environ. Sci. Technol.*, vol. 49, no. 8, pp. 5013–5020, Apr. 2015, doi: 10.1021/acs.est.5b00690.

[45] D.-W. Li, W.-L. Zhai, Y.-T. Li, and Y.-T. Long, “Recent progress in surface enhanced Raman spectroscopy for the detection of environmental pollutants,” *Microchim. Acta*, vol. 181, no. 1, pp. 23–43, 2014, doi: 10.1007/s00604-013-1115-3.

[46] H. Yuan *et al.*, “Mercaptopyridine-Functionalized Gold Nanoparticles for Fiber-Optic Surface Plasmon Resonance Hg2+ Sensing,” *ACS Sensors*, vol. 4, no. 3, pp. 704–710, Mar. 2019, doi: 10.1021/acssensors.8b01558.

[47] X. Zhao *et al.*, “Surface-Enhanced Raman Scattering Optophysiology Nanofibers for the Detection of Heavy Metals in Single Breast Cancer Cells,” *ACS Sensors*, vol. 6, no. 4, pp. 1649–1662, Apr. 2021, doi: 10.1021/acssensors.1c00332.

[48] L. Guerrini *et al.*, “Chemical speciation of heavy metals by surface-enhanced Raman scattering spectroscopy: identification and quantification of inorganic- and methyl-

mercury in water," *Nanoscale*, vol. 6, no. 14, pp. 8368–8375, 2014, doi: 10.1039/C4NR01464B.

[49] K. Sridhar, B. S. Inbaraj, and B.-H. Chen, "An improved surface enhanced Raman spectroscopic method using a paper-based grape skin-gold nanoparticles/graphene oxide substrate for detection of rhodamine 6G in water and food," *Chemosphere*, vol. 301, p. 134702, 2022, doi: https://doi.org/10.1016/j.chemosphere.2022.134702.

[50] J. Huang *et al.*, "Tyndall-effect-enhanced supersensitive naked-eye determination of mercury (II) ions with silver nanoparticles," *Sensors Actuators B Chem.*, vol. 344, p. 130218, 2021, doi: https://doi.org/10.1016/j.snb.2021.130218.

[51] F. Hu, Y. Li, Y. Zhang, Y. Li, H. Li, and S. Ai, "Flexible Ag NCs/CNFs film for colorimetric and SERS dual-mode ultrasensitive detection of mercury ions (II)," *Vib. Spectrosc.*, vol. 118, p. 103342, 2022, doi: https://doi.org/10.1016/j.vibspec.2022.103342.

[52] X. Xu, S. Yang, Y. Wang, and K. Qian, "Nanomaterial-based sensors and strategies for heavy metal ion detection," *Green Anal. Chem.*, vol. 2, p. 100020, 2022, doi: https://doi.org/10.1016/j.greeac.2022.100020.

[53] G. Panthi and M. Park, "Synthesis of metal nanoclusters and their application in Hg2+ ions detection: A review," *J. Hazard. Mater.*, vol. 424, p. 127565, 2022, doi: https://doi.org/10.1016/j.jhazmat.2021.127565.

[54] T. K. Kavya Bodhi, R. Tamizhselvi, S. Mohandoss, and A. Arumugam Napoleon, "Novel benzohydrazide-based Schiff base for highly selective and sensitive colorimetric detection of Hg2+ ions; DFT analysis and test strips applications," *Inorg. Chem. Commun.*, vol. 159, p. 111649, 2024, doi: https://doi.org/10.1016/j.inoche.2023.111649.

[55] P. P. Gawas, B. Ramakrishna, R. Pamanji, J. Selvin, and V. Nutalapati, “A novel triphenylamine based push–pull fluorophore bearing a 2-thiohydantoin unit for toxic Hg2+ ion detection: exploring its potential for live cell imaging††Electronic supplementary information (ESI) available. CCDC 2278085. For ESI and crystallographic,” *Mater. Adv.*, vol. 5, no. 1, pp. 336–348, 2024, doi: https://doi.org/10.1039/d3ma00559c.

[56] A. Chakraborty, V. K. Rajana, C. Saritha, A. Srivastava, D. Mandal, and N. Das, “A new Eosin Y-based ‘turnon’ fluorescent sensor for ratiometric sensing of toxic mercury ion (Hg2+) offering unaided eye detection and its antibacterial activity,” *J. Hazard. Mater.*, vol. 470, p. 134207, 2024, doi: https://doi.org/10.1016/j.jhazmat.2024.134207.

[57] R. Ayranci, G. Celik Cogal, M. Ak, and A. Uygun Oksuz, “A novel type of multifunctional pRM@Au-Ni micromotor for screening of Hg2+ heavy metal ion,” *Microchem. J.*, vol. 193, p. 109166, 2023, doi: https://doi.org/10.1016/j.microc.2023.109166.

[58] Z. Mirzaei Karazan, M. Roushani, and S. Jafar Hoseini, “Simultaneous electrochemical sensing of heavy metal ions (Zn2+, Cd2+, Pb2+, and Hg2+) in food samples using a covalent organic framework/carbon black modified glassy carbon electrode,” *Food Chem.*, vol. 442, p. 138500, 2024, doi: https://doi.org/10.1016/j.foodchem.2024.138500.

[59] Y. Duan *et al.*, “4-Mercaptopyridine Modified Fiber Optic Plasmonic Sensor for Sub-nM Mercury (II) Detection,” *Photonic Sensors*, vol. 12, no. 1, pp. 23–30, 2022, doi: 10.1007/s13320-021-0611-z.

[60] L. Chen, N. Qi, X. Wang, L. Chen, H. You, and J. Li, “Ultrasensitive surface-enhanced Raman scattering nanosensor for mercury ion detection based on functionalized silver

nanoparticles," *RSC Adv.*, vol. 4, no. 29, pp. 15055–15060, 2014, doi: 10.1039/C3RA47492E.

[61] L. Li *et al.*, "Applications of photochemical vapor generation-analytical atomic spectrometry for the speciation analysis of arsenic, mercury and selenium," *Spectrochim. Acta Part B At. Spectrosc.*, vol. 199, p. 106579, 2023, doi: https://doi.org/10.1016/j.sab.2022.106579.

[62] F. A. da Silva Cunha, M. J. de Oliveira, P. P. Florez-Rodriguez, and J. C. C. Santos, "Mercury speciation in estuarine water using dithiol-based magnetic solid-phase extraction and cold vapor atomic fluorescence spectrometry," *Spectrochim. Acta Part B At. Spectrosc.*, vol. 192, p. 106412, 2022, doi: https://doi.org/10.1016/j.sab.2022.106412.

[63] K.-Q. He *et al.*, "Identification of mercury species in coal combustion by-products from power plants using thermal desorption-atomic fluorescence spectrometry on-line coupling system," *Chemosphere*, vol. 312, p. 137206, 2023, doi: https://doi.org/10.1016/j.chemosphere.2022.137206.

[64] Y. Liu, J. Zou, B. Luo, H. Yu, Z. Zhao, and H. Xia, "Ivy extract-assisted photochemical vapor generation for sensitive determination of mercury by atomic fluorescence spectrometry," *Microchem. J.*, vol. 169, p. 106547, 2021, doi: https://doi.org/10.1016/j.microc.2021.106547.

[65] A. A. Krata and E. Vassileva, "Simultaneous speciation analysis of mercury in marine origin samples by high performance liquid chromatography and species - specific isotope dilution inductively coupled plasma mass spectrometry," *Talanta*, vol. 217, p. 121113, 2020, doi: https://doi.org/10.1016/j.talanta.2020.121113.

[66] S. Kulomäki, E. Lahtinen, S. Perämäki, and A. Väisänen, “Preconcentration and speciation analysis of mercury: 3D printed metal scavenger-based solid-phase extraction followed by analysis with inductively coupled plasma mass spectrometry,” *Talanta*, vol. 240, p. 123163, 2022, doi: https://doi.org/10.1016/j.talanta.2021.123163.

[67] S. Kulomäki, S. Perämäki, and A. Väisänen, “Addition of thiourea and hydrochloric acid: Accurate nanogram level analysis of mercury in humic-rich natural waters by inductively coupled plasma mass spectrometry,” *Talanta*, vol. 218, p. 121125, 2020, doi: https://doi.org/10.1016/j.talanta.2020.121125.

[68] K. K. Jinadasa, P. Herbello-Hermelo, E. Peña-Vázquez, P. Bermejo-Barrera, and A. Moreda-Piñeiro, “Mercury speciation in edible seaweed by liquid chromatography - Inductively coupled plasma mass spectrometry after ionic imprinted polymer-solid phase extraction,” *Talanta*, vol. 224, p. 121841, 2021, doi: https://doi.org/10.1016/j.talanta.2020.121841.

[69] T. P. T. Nguyen, M. H. Kim, Y. K. Kwon, and Y. S. Hong, “Fast and stable real time monitoring of gaseous mercury in its catalytic oxidation using a fully modified cold-vapor atomic absorption mercury analyzer,” *Measurement*, vol. 200, p. 111614, 2022, doi: https://doi.org/10.1016/j.measurement.2022.111614.

[70] G. da S. Coelho Junior, D. L. G. Borges, M. Svoboda, J. Dědina, and J. Kratzer, “Plasma-mediated vapor generation of mercury species in a dielectric barrier discharge: Direct analysis in a single drop by atomic absorption spectrometry,” *Spectrochim. Acta Part B At. Spectrosc.*, vol. 200, p. 106596, 2023, doi: https://doi.org/10.1016/j.sab.2022.106596.

[71] B. Zhao, M. He, B. Chen, and B. Hu, “Facile green synthesis of magnetic porous organic polymers for fast preconcentration of trace lead and mercury from environmental water

followed by graphite furnace atomic absorption spectrometry detection," *Spectrochim. Acta Part B At. Spectrosc.*, vol. 196, p. 106524, 2022, doi: https://doi.org/10.1016/j.sab.2022.106524.

[72] S. Sajed, F. Arefi, M. Kolahdouz, and M. A. Sadeghi, "Improving sensitivity of mercury detection using learning based smartphone colorimetry," *Sensors Actuators B Chem.*, vol. 298, p. 126942, 2019, doi: https://doi.org/10.1016/j.snb.2019.126942.

[73] J. Tao, S. Chen, E. K. Fodjo, W. Deng, and D. Li, "Tailoring dual-functional gold nanoplasmonic rods for colorimetric and SERS detection of mercury species in complex matrices," *Chem. Eng. J.*, vol. 452, p. 139026, 2023, doi: https://doi.org/10.1016/j.cej.2022.139026.

[74] J. Li, L. Li, X. Bi, X. Liu, L. Luo, and T. You, "Fluorescence/colorimetry dual-mode sensing strategy for mercury ion detection based on the quenching effect and nanozyme activity of porous cerium oxide nanorod," *Sensors Actuators B Chem.*, vol. 360, p. 131483, 2022, doi: https://doi.org/10.1016/j.snb.2022.131483.

[75] Q. Zheng *et al.*, "A Raman chip for rapid and specific detection of trace mercury ions in seawater," *Sensors Actuators B Chem.*, vol. 346, p. 130468, 2021, doi: https://doi.org/10.1016/j.snb.2021.130468.

[76] M. Zhou, M. Zheng, S. Xue, B. Chen, P. Wang, and Y. An, "A novel peptide-based fluorescent probe with large Stokes shift for simultaneous detection of zinc (II) and mercury (II): Smartphone, test strips, living cells and real samples applications," *J. Mol. Struct.*, vol. 1294, p. 136409, 2023, doi: https://doi.org/10.1016/j.molstruc.2023.136409.

[77] Y. Gou, P. Hou, Q. Wang, F. He, P. Wang, and X. Yang, "A novel AIE peptide-based fluorescent probe for highly selective detection of mercury(II) ions and its application in

food samples and cell imaging," *Microchem. J.*, vol. 195, p. 109400, 2023, doi: https://doi.org/10.1016/j.microc.2023.109400.

[78] J. Wang, Y. Liu, Z. Shang, C. Dong, Y. Wang, and S. Shuang, "A novel multi-functional fluorescent probe for dual-channel detection of SO2 and Hg2+ and dynamic visualization of SO2 fluctuations in vivo upon mercury exposure," *Anal. Chim. Acta*, vol. 1279, p. 341786, 2023, doi: https://doi.org/10.1016/j.aca.2023.341786.

[79] Y. An *et al.*, "A rapid and specific fluorescent probe based on aggregation-induced emission enhancement for mercury ion detection in living systems," *J. Hazard. Mater.*, vol. 465, p. 133331, 2024, doi: https://doi.org/10.1016/j.jhazmat.2023.133331.

[80] L. Wang, Y. Ma, and W. Lin, "A coumarin-based fluorescent probe for highly selective detection of hazardous mercury ions in living organisms," *J. Hazard. Mater.*, vol. 461, p. 132604, 2024, doi: https://doi.org/10.1016/j.jhazmat.2023.132604.

[81] S. Fang *et al.*, "Insight into mercury ion detection in environmental samples and imaging in living systems by a near-infrared fluorescent probe," *Sensors Actuators B Chem.*, vol. 411, p. 135768, 2024, doi: https://doi.org/10.1016/j.snb.2024.135768.

[82] M. Saqib, S. Bashir, S. Ali, and R. Hao, "Highly selective and sensitive detection of mercury (II) and dopamine based on the efficient electrochemiluminescence of Ru(bpy)32+ with acridine orange as a coreactant," *J. Electroanal. Chem.*, vol. 906, p. 115896, 2022, doi: https://doi.org/10.1016/j.jelechem.2021.115896.

[83] C. Qu, H. Fang, F. Yu, J. Chen, M. Su, and H. Liu, "Artificial nose of scalable plasmonic array gas sensor for Multi-Dimensional SERS recognition of volatile organic compounds," *Chem. Eng. J.*, vol. 482, p. 148773, 2024, doi: https://doi.org/10.1016/j.cej.2024.148773.

[84] Q. Wang, K. Chang, Q. Yang, and W. Wu, “Semiconductor-based surface-enhanced Raman scattering sensing platforms: State of the art, applications and prospects in food safety,” *Trends Food Sci. Technol.*, vol. 147, p. 104460, 2024, doi: https://doi.org/10.1016/j.tifs.2024.104460.

[85] K. Dey, V. S. Goudar, K. Kaladharan, T. S. Santra, and F.-G. Tseng, “Continuous in-vitro physiological glucose sensing for co-cultured 3D tumour spheroids using SERS based nano particle sensors (SERS-gNPS),” *Sensors Actuators B Chem.*, vol. 404, p. 135243, 2024, doi: https://doi.org/10.1016/j.snb.2023.135243.

[86] K. Lai *et al.*, “A hybrid SERS sensing platform constructed by porous carbon/Ag nanoparticles for efficient imatinib detection in bio-environment,” *Spectrochim. Acta Part A Mol. Biomol. Spectrosc.*, vol. 300, p. 122971, 2023, doi: https://doi.org/10.1016/j.saa.2023.122971.

[87] T. N. Q. Trang, N. T. G. Bao, L. Q. Vinh, and V. T. H. Thu, “Centrifuge tube-based SERS sensor on heterogenous dimers of plasmonic coupling as a microreactor for ultrasensitive SERS sensing pesticide residues in environmental water,” *Sensors Actuators A Phys.*, vol. 369, p. 115173, 2024, doi: https://doi.org/10.1016/j.sna.2024.115173.

[88] L. Vázquez-Iglesias *et al.*, “SERS sensing for cancer biomarker: Approaches and directions,” *Bioact. Mater.*, vol. 34, pp. 248–268, 2024, doi: https://doi.org/10.1016/j.bioactmat.2023.12.018.

[89] Y. Lu *et al.*, “A recyclable SERS-DGT device for in-situ sensing of sulfamethazine by Au@g-C3N4NS in water,” *Water Res.*, vol. 253, p. 121307, 2024, doi: https://doi.org/10.1016/j.watres.2024.121307.

[90] M. Qi *et al.*, “Smartphone readable colorimetry and surface-enhanced raman scattering (SERS) dual-mode sensing platform for ascorbic acid detection based on GeO2 composite nanozymes,” *J. Food Compos. Anal.*, vol. 125, p. 105740, 2024, doi: https://doi.org/10.1016/j.jfca.2023.105740.

[91] A. Srivastava, T. K. Naqvi, A. K. Srivastava, P. K. Dwivedi, and S. K. Jha, “Nitrogen and sulfur co-doped reduced graphene oxide (rGO)/gold nanoparticles hybrids for SERS sensing platform,” *Sensors Actuators A Phys.*, vol. 363, p. 114758, 2023, doi: https://doi.org/10.1016/j.sna.2023.114758.

[92] J. Zhou, Y. Du, H. Li, L. Zheng, Y. Zhang, and L. Fu, “A novel AuNRs self-assembly dimer-based aptasensor for ultrasensitive SERS sensing of wheat gluten,” *Sensors Actuators B Chem.*, vol. 393, p. 134233, 2023, doi: https://doi.org/10.1016/j.snb.2023.134233.

[93] N. Tyagi *et al.*, “2D-MXenes to tackle wastewater: From purification to SERS-based sensing,” *Coord. Chem. Rev.*, vol. 496, p. 215394, 2023, doi: https://doi.org/10.1016/j.ccr.2023.215394.

[94] Y. Qin, X. Tian, H. Wang, X. Guo, Y. Wen, and H. Yang, “Magnetically optimized surface enhanced Raman scattering detection strategy and its sensing applications,” *Coord. Chem. Rev.*, vol. 510, p. 215848, 2024, doi: https://doi.org/10.1016/j.ccr.2024.215848.

[95] C. Wang, G. Weng, J. Li, J. Zhu, and J. Zhao, “A review of SERS coupled microfluidic platforms: From configurations to applications,” *Anal. Chim. Acta*, vol. 1296, p. 342291, 2024, doi: https://doi.org/10.1016/j.aca.2024.342291.

[96] J. Xu, W. Gao, and S. Jiang, “Synergistically enhanced electric field in inhomogeneous nanocavities for the application of recyclable SERS sensing,” *Appl. Mater. Today*, vol. 26, p. 101251, 2022, doi: https://doi.org/10.1016/j.apmt.2021.101251.

[97] T. N. Quynh Trang, N. T. Phuong Trinh, N. T. Gia Bao, and V. T. H. Thu, “Hotspot-type silver-polymers grafted nanocellulose paper with analyte enrichment as flexible plasmonic sensors for highly sensitive SERS sensing,” *J. Sci. Adv. Mater. Devices*, vol. 8, no. 3, p. 100597, 2023, doi: https://doi.org/10.1016/j.jsamd.2023.100597.

[98] R. A. Alvarez-Puebla and L. M. Liz-Marzán, “SERS Detection of Small Inorganic Molecules and Ions,” *Angew. Chemie Int. Ed.*, vol. 51, no. 45, pp. 11214–11223, Nov. 2012, doi: https://doi.org/10.1002/anie.201204438.

[99] W. Ma, M. Sun, L. Xu, L. Wang, H. Kuang, and C. Xu, “A SERS active gold nanostar dimer for mercury ion detection,” *Chem. Commun.*, vol. 49, no. 44, pp. 4989–4991, 2013, doi: 10.1039/C3CC39087J.

[100] Z. Guo *et al.*, “Chemometrics coupled 4-Aminothiophenol labelled Ag-Au alloy SERS off-signal nanosensor for quantitative detection of mercury in black tea,” *Spectrochim. Acta Part A Mol. Biomol. Spectrosc.*, vol. 242, p. 118747, 2020, doi: https://doi.org/10.1016/j.saa.2020.118747.

[101] B. Anantha Lakshmi, R. Sangubotla, J. Kim, and Y.-J. Kim, “Vinyl-functionalized polyphenolic-carbon dot-based fluorometric turn-off–on biosensor for the dual detection of mercury and cysteine and their in vivo sensing in zebrafish larvae,” *Spectrochim. Acta Part A Mol. Biomol. Spectrosc.*, vol. 282, p. 121685, 2022, doi: https://doi.org/10.1016/j.saa.2022.121685.

[102] A. Thakuri, A. A. Bhosle, S. D. Hiremath, M. Banerjee, and A. Chatterjee, “A carbon dots-MnO2 nanosheet-based turn-on pseudochemodosimeter as low-cost probe for selective detection of hazardous mercury ion contaminations in water,” *J. Hazard. Mater.*, vol. 469, p. 133998, 2024, doi: https://doi.org/10.1016/j.jhazmat.2024.133998.

[103] W. Ren, C. Zhu, and E. Wang, “Enhanced sensitivity of a direct SERS technique for Hg2+ detection based on the investigation of the interaction between silver nanoparticles and mercury ions,” *Nanoscale*, vol. 4, no. 19, pp. 5902–5909, 2012, doi: 10.1039/C2NR31410J.

[104] Q. Ran, H. Feng, G. Chang, M. Luo, and S. Xu, “Thymine-mediated electrochemical aptasensor for sensitive and simultaneous detection of Hg2+ and CH3Hg+ in fish samples,” *Electrochim. Acta*, vol. 461, p. 142406, 2023, doi: https://doi.org/10.1016/j.electacta.2023.142406.

[105] H. Torigoe, J. Kondo, and F. Arakawa, “Specific binding of Hg2+ to mismatched base pairs involving 5-hydroxyuracil in duplex DNA,” *J. Inorg. Biochem.*, vol. 241, p. 112125, 2023, doi: https://doi.org/10.1016/j.jinorgbio.2023.112125.

[106] H. J. Chun *et al.*, “Water-soluble mercury ion sensing based on the thymine-Hg2+-thymine base pair using retroreflective Janus particle as an optical signaling probe,” *Biosens. Bioelectron.*, vol. 104, pp. 138–144, 2018, doi: https://doi.org/10.1016/j.bios.2018.01.008.

[107] G. Zeng *et al.*, “Practical and regenerable electrochemical aptasensor based on nanoporous gold and thymine-Hg2+-thymine base pairs for Hg2+ detection,” *Biosens. Bioelectron.*, vol. 90, pp. 542–548, 2017, doi: https://doi.org/10.1016/j.bios.2016.10.018.

[108] Z. Sheng, J. Han, J. Zhang, H. Zhao, and L. Jiang, "Method for detection of Hg2+ based on the specific thymine–Hg2+–thymine interaction in the DNA hybridization on the surface of quartz crystal microbalance," *Colloids Surfaces B Biointerfaces*, vol. 87, no. 2, pp. 289–292, 2011, doi: https://doi.org/10.1016/j.colsurfb.2011.05.031.

[109] E. Xiong, L. Wu, J. Zhou, P. Yu, X. Zhang, and J. Chen, "A ratiometric electrochemical biosensor for sensitive detection of Hg2+ based on thymine–Hg2+–thymine structure," *Anal. Chim. Acta*, vol. 853, pp. 242–248, 2015, doi: https://doi.org/10.1016/j.aca.2014.10.015.

[110] B. Sun *et al.*, "Surface-Enhancement Raman Scattering Sensing Strategy for Discriminating Trace Mercuric Ion (II) from Real Water Samples in Sensitive, Specific, Recyclable, and Reproducible Manners," *Anal. Chem.*, vol. 87, no. 2, pp. 1250–1256, Jan. 2015, doi: 10.1021/ac503939d.

[111] L. Xu, H. Yin, W. Ma, H. Kuang, L. Wang, and C. Xu, "Ultrasensitive SERS detection of mercury based on the assembled gold nanochains," *Biosens. Bioelectron.*, vol. 67, pp. 472–476, 2015, doi: https://doi.org/10.1016/j.bios.2014.08.088.

[112] E. Chung *et al.*, "Trace analysis of mercury(ii) ions using aptamer-modified Au/Ag core–shell nanoparticles and SERS spectroscopy in a microdroplet channel," *Lab Chip*, vol. 13, no. 2, pp. 260–266, 2013, doi: 10.1039/C2LC41079F.

[113] D. M. Arvapalli, A. T. Sheardy, K. C. Alapati, and J. Wei, "High Quantum Yield Fluorescent Carbon Nanodots for detection of Fe (III) Ions and Electrochemical Study of Quenching Mechanism," *Talanta*, vol. 209, p. 120538, 2020, doi: https://doi.org/10.1016/j.talanta.2019.120538.

[114] P. Luo, C. Li, and G. Shi, “Synthesis of gold@carbon dots composite nanoparticles for surface enhanced Raman scattering,” *Phys. Chem. Chem. Phys.*, vol. 14, no. 20, pp. 7360–7366, 2012, doi: 10.1039/C2CP40767A.

[115] G. FRENS, “Controlled Nucleation for the Regulation of the Particle Size in Monodisperse Gold Suspensions,” *Nat. Phys. Sci.*, vol. 241, no. 105, pp. 20–22, 1973, doi: 10.1038/physci241020a0.

[116] M. Berge *et al.*, “Optimization of experimental conditions by surface enhanced Raman Scattering (SERS) spectroscopy with gold nanoparticles suspensions,” *Spectrochim. Acta Part A Mol. Biomol. Spectrosc.*, vol. 268, p. 120628, 2022, doi: https://doi.org/10.1016/j.saa.2021.120628.

[117] B. Bagra, W. Zhang, Z. Zeng, T. Mabe, and J. Wei, “Plasmon-Enhanced Fluorescence of Carbon Nanodots in Gold Nanoslit Cavities,” *Langmuir*, vol. 35, no. 27, pp. 8903–8909, Jun. 2019, doi: 10.1021/acs.langmuir.9b00448.

[118] R. Liu *et al.*, “Metal Nanoparticle/Carbon Quantum Dot Composite as a Photocatalyst for High-Efficiency Cyclohexane Oxidation,” *ACS Catal.*, vol. 4, no. 1, pp. 328–336, Jan. 2014, doi: 10.1021/cs400913h.

[119] X. Fei *et al.*, “One-pot green synthesis of flower-liked Au NP@GQDs nanocomposites for surface-enhanced Raman scattering,” *J. Alloys Compd.*, vol. 725, pp. 1084–1090, 2017, doi: https://doi.org/10.1016/j.jallcom.2017.05.072.

[120] M. Ayiania, M. Smith, A. J. R. Hensley, L. Scudiero, J.-S. McEwen, and M. Garcia-Perez, “Deconvoluting the XPS spectra for nitrogen-doped chars: An analysis from first principles,” *Carbon N. Y.*, vol. 162, pp. 528–544, 2020, doi: https://doi.org/10.1016/j.carbon.2020.02.065.

[121] H. Qiu *et al.*, “Self-cleaning SERS membrane for reusable and ultrasensitive molecular detection via integrating graphitic-carbon-nitride nanosheets and Ag nanospheres into hierarchical graphene layers that covered with graphitic-carbon-nitride quantum-dots,” *Appl. Surf. Sci.*, vol. 489, pp. 1010–1018, 2019, doi: https://doi.org/10.1016/j.apsusc.2019.05.349.

[122] S. Saha, B. Dutta, M. Ghosh, and J. Chowdhury, “Adsorption of 4-Mercapto Pyridine with Gold Nanoparticles Embedded in the Langmuir–Blodgett Film Matrix of Stearic Acid: SERS, XPS Studies Aided by Born–Oppenheimer on the Fly Dynamics, Time–Resolved Wavelet Transform Theory, and DFT,” *ACS Omega*, vol. 7, no. 32, pp. 27818–27830, Aug. 2022, doi: 10.1021/acsomega.1c07321.

[123] Q. Zhou, G. Zhao, Y. Chao, Y. Li, Y. Wu, and J. Zheng, “Charge-Transfer Induced Surface-Enhanced Raman Scattering in Silver Nanoparticle Assemblies,” *J. Phys. Chem. C*, vol. 111, no. 5, pp. 1951–1954, Feb. 2007, doi: 10.1021/jp067045s.

[124] S. Saha, M. Ghosh, and J. Chowdhury, “Infused self-assembly on Langmuir–Blodgett Film: Fabrication of highly efficient SERS active substrates with controlled plasmonic aggregates,” *J. Raman Spectrosc.*, vol. 50, no. 3, pp. 330–344, Mar. 2019, doi: https://doi.org/10.1002/jrs.5529.

[125] “Spectroscopic Ellipsometric Evaluation of Gold Nanoparticle Thin Films Fabricated Using Layer-by-Layer Self-Assembly,” *Advanced Materials*, vol. 15, no. 6. pp. 531–534, doi: 10.1002/adma.200390124.

[126] M. Han, Y. Xie, R. Wang, Y. Li, C. Bian, and S. Xia, “4-Mercaptopyridine-Modified Sensor for the Sensitive Electrochemical Detection of Mercury Ions,” *Micromachines*, vol. 14, no. 4. 2023, doi: 10.3390/mi14040739.

[127] J. Schneider *et al.*, “Molecular fluorescence in citric acid-based carbon dots,” *J. Phys. Chem. C*, vol. 121, no. 3, pp. 2014–2022, 2017, doi: 10.1021/acs.jpcc.6b12519.

[128] C. Kavitha, K. Bramhaiah, N. S. John, and B. E. Ramachandran, “Low cost, ultra-thin films of reduced graphene oxide–Ag nanoparticle hybrids as SERS based excellent dye sensors,” *Chem. Phys. Lett.*, vol. 629, pp. 81–86, 2015, doi: https://doi.org/10.1016/j.cplett.2015.04.026.

[129] K. Li, A. Liang, C. Jiang, F. Li, Q. Liu, and Z. Jiang, “A stable and reproducible nanosilver-aggregation-4-mercaptopyridine surface-enhanced Raman scattering probe for rapid determination of trace Hg2+,” *Talanta*, vol. 99, pp. 890–896, 2012, doi: https://doi.org/10.1016/j.talanta.2012.07.052.

[130] A. G. Brolo, M. Odziemkowski, J. Porter, and D. E. Irish, “In situ micro Raman investigation of electrochemically formed halide and pseudohalide films on mercury electrodes,” *J. Raman Spectrosc.*, vol. 33, no. 3, pp. 136–141, Mar. 2002, doi: https://doi.org/10.1002/jrs.811.

[131] S. Akyüz, A. B. Dempster, R. L. Morehouse, and S. Suzuki, “An infrared and Raman spectroscopic study of some metal pyridine tetracyanonickelate complexes,” *J. Mol. Struct.*, vol. 17, no. 1, pp. 105–125, 1973, doi: https://doi.org/10.1016/0022-2860(73)85047-1.

[132] S. Nie and S. R. Emory, “Probing Single Molecules and Single Nanoparticles by Surface-Enhanced Raman Scattering,” *Science (80-.).*, vol. 275, no. 5303, pp. 1102–1106, Feb. 1997, doi: 10.1126/science.275.5303.1102.

[133] B. Liu, M. Lin, and H. Li, “Potential of SERS for rapid detection of melamine and cyanuric acid extracted from milk,” *Sens. Instrum. Food Qual. Saf.*, vol. 4, no. 1, pp. 13–19, 2010, doi: 10.1007/s11694-009-9091-3.

[134] A. M. Michaels, M. Nirmal, and L. E. Brus, “Surface Enhanced Raman Spectroscopy of Individual Rhodamine 6G Molecules on Large Ag Nanocrystals,” *J. Am. Chem. Soc.*, vol. 121, no. 43, pp. 9932–9939, Nov. 1999, doi: 10.1021/ja992128q.

[135] H. Li *et al.*, “Gold-Stabilized Gold–Silver Alloy Nanostructures as High-Performance SERS Substrate,” *Plasmonics*, vol. 15, no. 6, pp. 2027–2032, 2020, doi: 10.1007/s11468-020-01229-0.

[136] J. Duan and J. Zhan, “Recent developments on nanomaterials-based optical sensors for Hg2+ detection,” *Sci. China Mater.*, vol. 58, no. 3, pp. 223–240, 2015, doi: 10.1007/s40843-015-0031-8.

[137] D. Han, S. Y. Lim, B. J. Kim, L. Piao, and T. D. Chung, “Mercury(ii) detection by SERS based on a single gold microshell,” *Chem. Commun.*, vol. 46, no. 30, pp. 5587–5589, 2010, doi: 10.1039/C0CC00895H.

[138] N. D. Donahue, H. Acar, and S. Wilhelm, “Concepts of nanoparticle cellular uptake, intracellular trafficking, and kinetics in nanomedicine,” *Adv. Drug Deliv. Rev.*, vol. 143, pp. 68–96, 2019, doi: https://doi.org/10.1016/j.addr.2019.04.008.

[139] A. Sohrabi Kashani, A. Piekny, and M. Packirisamy, “Using intracellular plasmonics to characterize nanomorphology in human cells,” *Microsystems Nanoeng.*, vol. 6, no. 1, p. 110, 2020, doi: 10.1038/s41378-020-00219-w.

[140] K. H. Kim *et al.*, “PRMT5 mediates FoxO1 methylation and subcellular localization to regulate lipophagy in myogenic progenitors,” *Cell Rep.*, vol. 42, no. 11, p. 113329, 2023,

doi: https://doi.org/10.1016/j.celrep.2023.113329.

[141] X. Shao, C. Meng, W. Song, T. Zhang, and Q. Chen, “Subcellular visualization: Organelle-specific targeted drug delivery and discovery,” *Adv. Drug Deliv. Rev.*, vol. 199, p. 114977, 2023, doi: https://doi.org/10.1016/j.addr.2023.114977.

[142] C. Péchoux, F. Antigny, and F. B. T.-M. in C. B. Perros, “A correlated light and electron microscopy approach to study the subcellular localization of phosphorylated vimentin in human lung tissue,” Academic Press, 2024.

[143] B. J. Inkson, “2 - Scanning electron microscopy (SEM) and transmission electron microscopy (TEM) for materials characterization,” G. Hübschen, I. Altpeter, R. Tschuncky, and H.-G. B. T.-M. C. U. N. E. (NDE) M. Herrmann, Eds. Woodhead Publishing, 2016, pp. 17–43.

[144] S. Chen *et al.*, “Direct Observation of Nanoparticles within Cells at Subcellular Levels by Super-Resolution Fluorescence Imaging,” *Anal. Chem.*, vol. 91, no. 9, pp. 5747–5752, May 2019, doi: 10.1021/acs.analchem.8b05919.

[145] E. Efeoglu, M. Keating, J. McIntyre, A. Casey, and H. J. Byrne, “Determination of nanoparticle localisation within subcellular organelles in vitro using Raman spectroscopy,” *Anal. Methods*, vol. 7, no. 23, pp. 10000–10017, 2015, doi: 10.1039/C5AY02661J.

[146] A. Ostrowski *et al.*, “Overview about the localization of nanoparticles in tissue and cellular context by different imaging techniques,” *Beilstein J. Nanotechnol.*, vol. 6, pp. 263–280, 2015, doi: 10.3762/bjnano.6.25.

[147] R. Fakhrullin, L. Nigamatzyanova, and G. Fakhrullina, “Dark-field/hyperspectral microscopy for detecting nanoscale particles in environmental nanotoxicology research,”

Sci. Total Environ., vol. 772, p. 145478, 2021, doi: https://doi.org/10.1016/j.scitotenv.2021.145478.

[148] P. Zamora-Perez, D. Tsoutsi, R. Xu, and P. Rivera_Gil, "Hyperspectral-Enhanced Dark Field Microscopy for Single and Collective Nanoparticle Characterization in Biological Environments," *Materials*, vol. 11, no. 2. 2018, doi: 10.3390/ma11020243.

[149] Y. Wu, M. R. K. Ali, K. Chen, N. Fang, and M. A. El-Sayed, "Gold nanoparticles in biological optical imaging," *Nano Today*, vol. 24, pp. 120–140, 2019, doi: https://doi.org/10.1016/j.nantod.2018.12.006.

[150] S. Lawrence, "Enhanced Darkfield Optical Microscopy Opens New Nano-Scale Imaging Possibilities," *Micros. Today*, vol. 29, no. 1, pp. 50–55, Jan. 2021, doi: 10.1017/S1551929520001765.

[151] D. Zopf, J. Jatschka, A. Dathe, N. Jahr, W. Fritzsche, and O. Stranik, "Hyperspectral imaging of plasmon resonances in metallic nanoparticles," *Biosens. Bioelectron.*, vol. 81, pp. 287–293, 2016, doi: https://doi.org/10.1016/j.bios.2016.03.001.

[152] M. L. de O. Pereira, D. Grasseschi, and H. E. Toma, "Photocatalytic Activity of Reduced Graphene Oxide–Gold Nanoparticle Nanomaterials: Interaction with Asphaltene and Conversion of a Model Compound," *Energy & Fuels*, vol. 32, no. 3, pp. 2673–2680, Mar. 2018, doi: 10.1021/acs.energyfuels.7b02715.

[153] N. M. Neu-Baker, A. K. Dozier, A. C. Eastlake, and S. A. Brenner, "Evaluation of enhanced darkfield microscopy and hyperspectral imaging for rapid screening of TiO2 and SiO2 nanoscale particles captured on filter media," *Microsc. Res. Tech.*, vol. 84, no. 12, pp. 2968–2976, Dec. 2021, doi: https://doi.org/10.1002/jemt.23856.

[154] L. Nigamatzyanova and R. Fakhrullin, "Dark-field hyperspectral microscopy for label-free

microplastics and nanoplastics detection and identification in vivo: A Caenorhabditis elegans study," *Environ. Pollut.*, vol. 271, p. 116337, 2021, doi: https://doi.org/10.1016/j.envpol.2020.116337.

[155] P. F. Gao, G. Lei, and C. Z. Huang, "Dark-Field Microscopy: Recent Advances in Accurate Analysis and Emerging Applications," *Anal. Chem.*, vol. 93, no. 11, pp. 4707–4726, Mar. 2021, doi: 10.1021/acs.analchem.0c04390.

[156] D. Sun and T. Y. Hu, "A low cost mobile phone dark-field microscope for nanoparticle-based quantitative studies," *Biosens. Bioelectron.*, vol. 99, pp. 513–518, 2018, doi: https://doi.org/10.1016/j.bios.2017.08.025.

[157] S. Batasheva, F. Akhatova, N. Abubakirov, and R. Fakhrullin, "Probing nanoplastics derived from polypropylene face masks with hyperspectral dark-field microscopy," *Sci. Total Environ.*, vol. 854, p. 158574, 2023, doi: https://doi.org/10.1016/j.scitotenv.2022.158574.

[158] L. Zheng, Y. Wen, W. Ren, H. Duan, J. Lin, and J. Irudayaraj, "Hyperspectral dark-field microscopy for pathogen detection based on spectral angle mapping," *Sensors Actuators B Chem.*, vol. 367, p. 132042, 2022, doi: https://doi.org/10.1016/j.snb.2022.132042.

[159] Y. Liu, E. Naumenko, F. Akhatova, Q. Zou, R. Fakhrullin, and X. Yan, "Self-assembled peptide nanoparticles for enhanced dark-field hyperspectral imaging at the cellular and invertebrate level," *Chem. Eng. J.*, vol. 424, p. 130348, 2021, doi: https://doi.org/10.1016/j.cej.2021.130348.

[160] M. Tiwari *et al.*, "Comparative transcriptome and proteome analysis to reveal the biosynthesis of gold nanoparticles in Arabidopsis," *Sci. Rep.*, vol. 6, no. 1, p. 21733, 2016, doi: 10.1038/srep21733.

[161] M. Basnet, A. Gershanov, K. J. Wilkinson, S. Ghoshal, and N. Tufenkji, “Interaction between palladium-doped zerovalent iron nanoparticles and biofilm in granular porous media: characterization, transport and viability,” *Environ. Sci. Nano*, vol. 3, no. 1, pp. 127–137, 2016, doi: 10.1039/C5EN00109A.

[162] K. Bromma, L. Cicon, W. Beckham, and D. B. Chithrani, “Gold nanoparticle mediated radiation response among key cell components of the tumour microenvironment for the advancement of cancer nanotechnology,” *Sci. Rep.*, vol. 10, no. 1, p. 12096, 2020, doi: 10.1038/s41598-020-68994-0.

[163] M. R. Dzamukova, E. A. Naumenko, E. V Rozhina, A. A. Trifonov, and R. F. Fakhrullin, “Cell surface engineering with polyelectrolyte-stabilized magnetic nanoparticles: A facile approach for fabrication of artificial multicellular tissue-mimicking clusters,” *Nano Res.*, vol. 8, no. 8, pp. 2515–2532, 2015, doi: 10.1007/s12274-015-0759-1.

[164] M. Guttenberg *et al.*, “Biodistribution of inhaled metal oxide nanoparticles mimicking occupational exposure: a preliminary investigation using enhanced darkfield microscopy,” *J. Biophotonics*, vol. 9, no. 10, pp. 987–993, Oct. 2016, doi: https://doi.org/10.1002/jbio.201600125.

[165] E. D. SoRelle, O. Liba, J. L. Campbell, R. Dalal, C. L. Zavaleta, and A. de la Zerda, “A hyperspectral method to assay the microphysiological fates of nanomaterials in histological samples,” *Elife*, vol. 5, p. e16352, 2016, doi: 10.7554/eLife.16352.

APENDIX A: SURFACE-ENHANCED RAMAN SCATTERING ENHANCEMENT USING A HYBRID GOLD NANOPARTICLES@CARBON NANODOTS SUBSTRATE FOR HERBICIDE DETECTION

Figure A3.1. TEM images of AuNPs@CNDs at different $HAuCl_4$ volume from 70-190 µL ($HAuCl_4$/CNDs mass ratio of 5.2, 3.3, 2.4, and 1.9 from a to d, respectively).

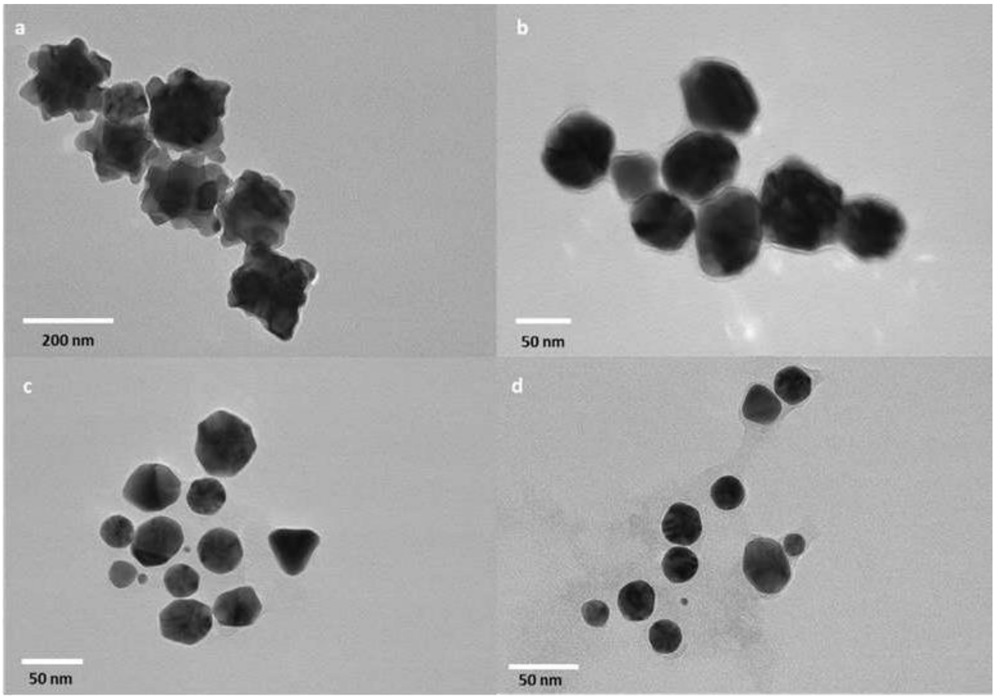

Figure A3.2. Size distribution of AuNPs@CNDs at different $HAuCl_4$ volume from 70-190 μL ($HAuCl_4$/CNDs mass ratio of 5.2, 3.3, 2.4, and 1.9 from a to d, respectively.

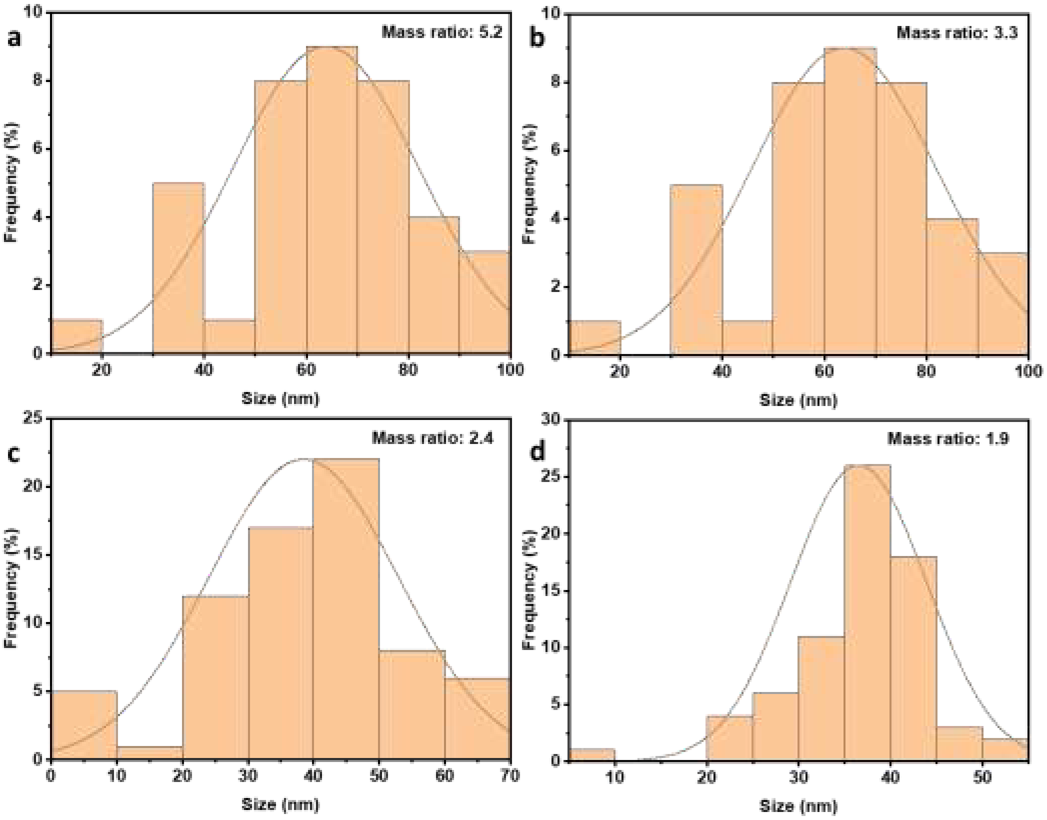

Figure A3.3. UV-vis spectra of AuNPs@CNDs (concentration of CNDs was 0.09, 0.11, and 0.12 mg mL^{-1} while concentration of $HAuCl_4$ was 1 mg mL^{-1}) (a). UV-vis spectra of AuNPs@CNDs with different mass ratio of $HAuCl_4$/CNDs from 5.2-1.9 while the volume of $HAuCl_4$ was 70, 110, 150, and 190 µL and concentration of CNDs was 0.12 mg mL^{-1} (b).

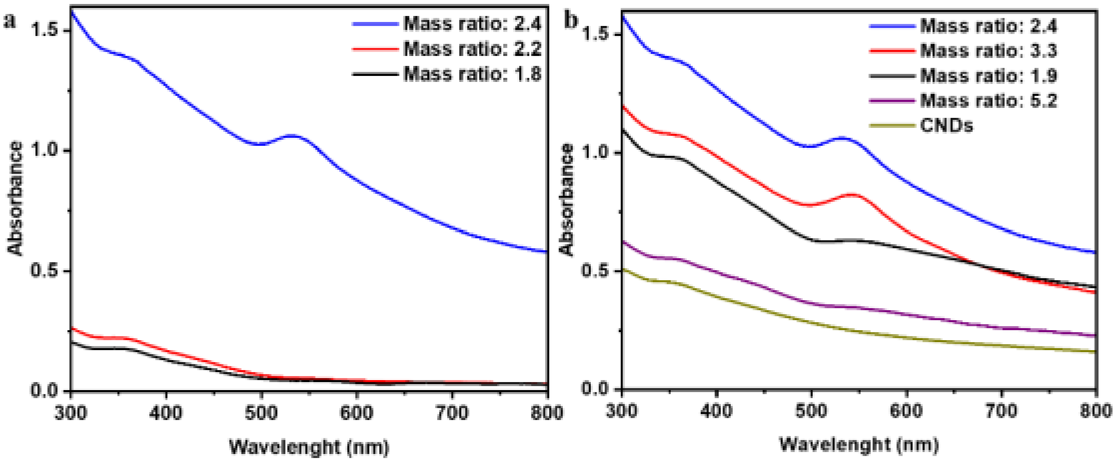

Figure A3.4. Raman spectra of AuNPs@CNDs and CNDs (a). PL spectra of AuNPs@CNDs and CNDs aqueous suspension excited at 380 nm (b).

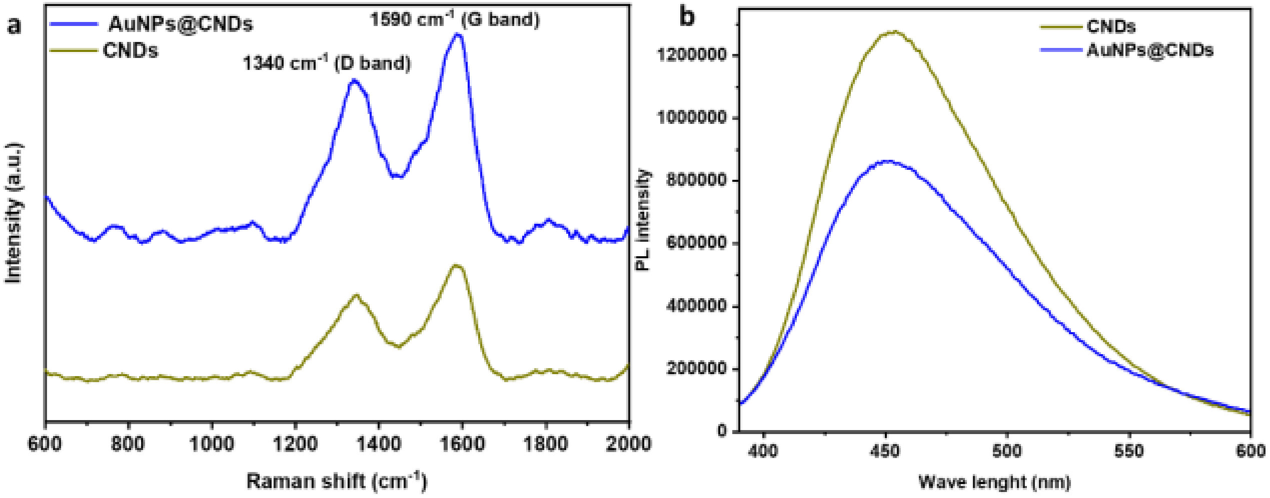

Figure A3.5. Full-scan XPS spectra of CNDs (a) and AuNPs@CNDs (b); The N1s XPS spectra of AuNPs@CNDs (c); The C1s XPS spectra of CNDs (d) and AuNPs@CNDs (e); The O1s XPS spectra of AuNPs@CNDs (f).

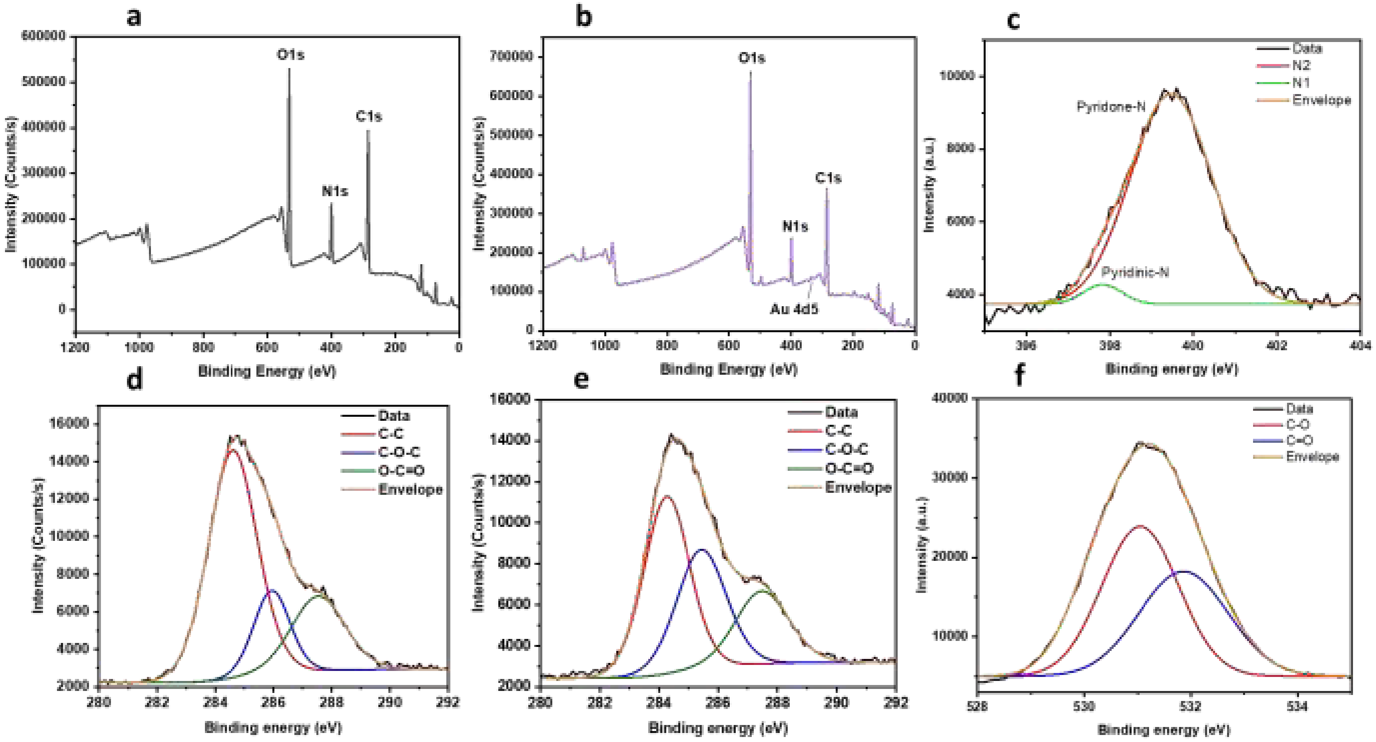

Figure A3.6. SERS spectra of (a) 10^{-3} M CGA77102, (b) A19414A, (c) 10^{-3} M ZA1296E, and (d) and 10^{-3} M A12738A using AuNPs@CNDs and AuNPs, respectively, which show the largely increased Raman signal using AuNPs@CNDs as probes in sensing.

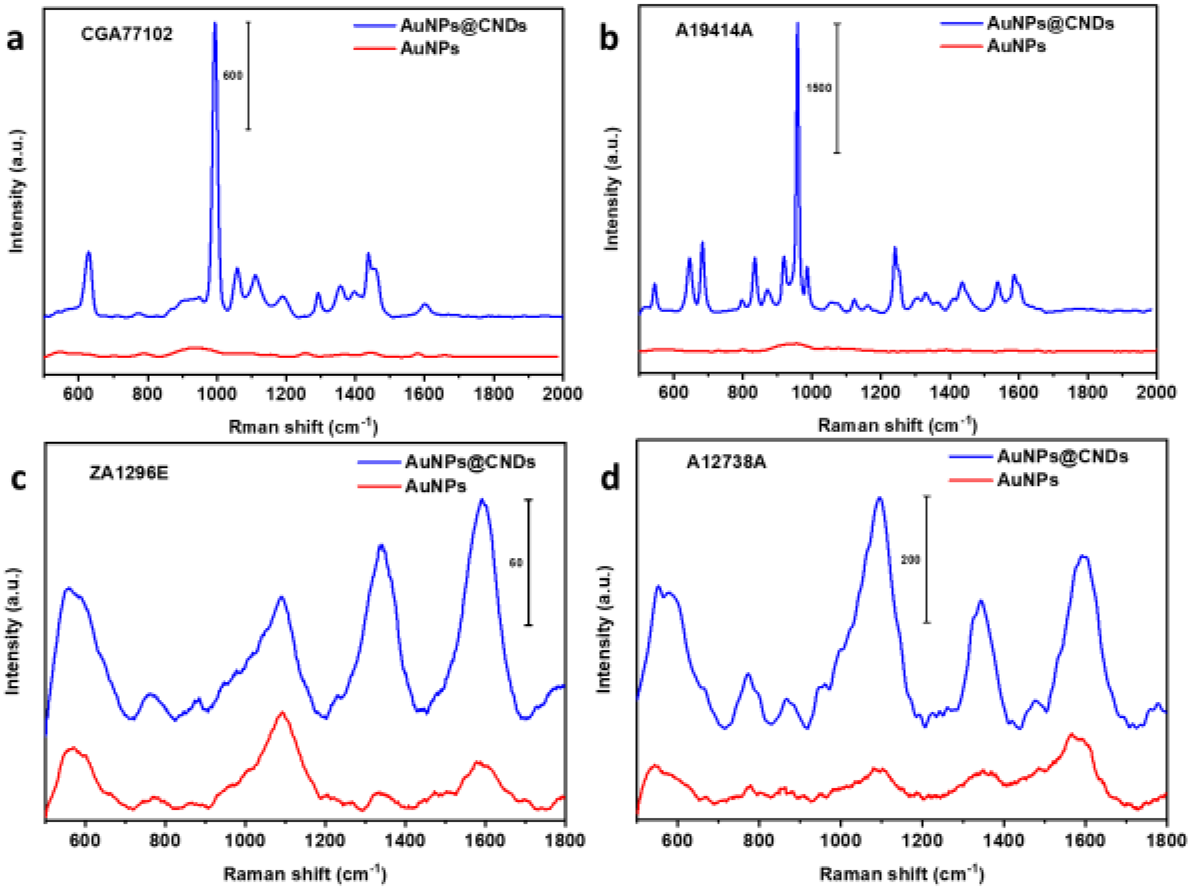

Figure A3.7. SERS spectra of spiked samples at three different concentrations 10^{-10}, 10^{-6} and 10^{-3} M for (a) CGA77102, (b) A19414A, (c) ZA1296E, and (d) A12738A using AuNPs@CNDs for SERS detection.

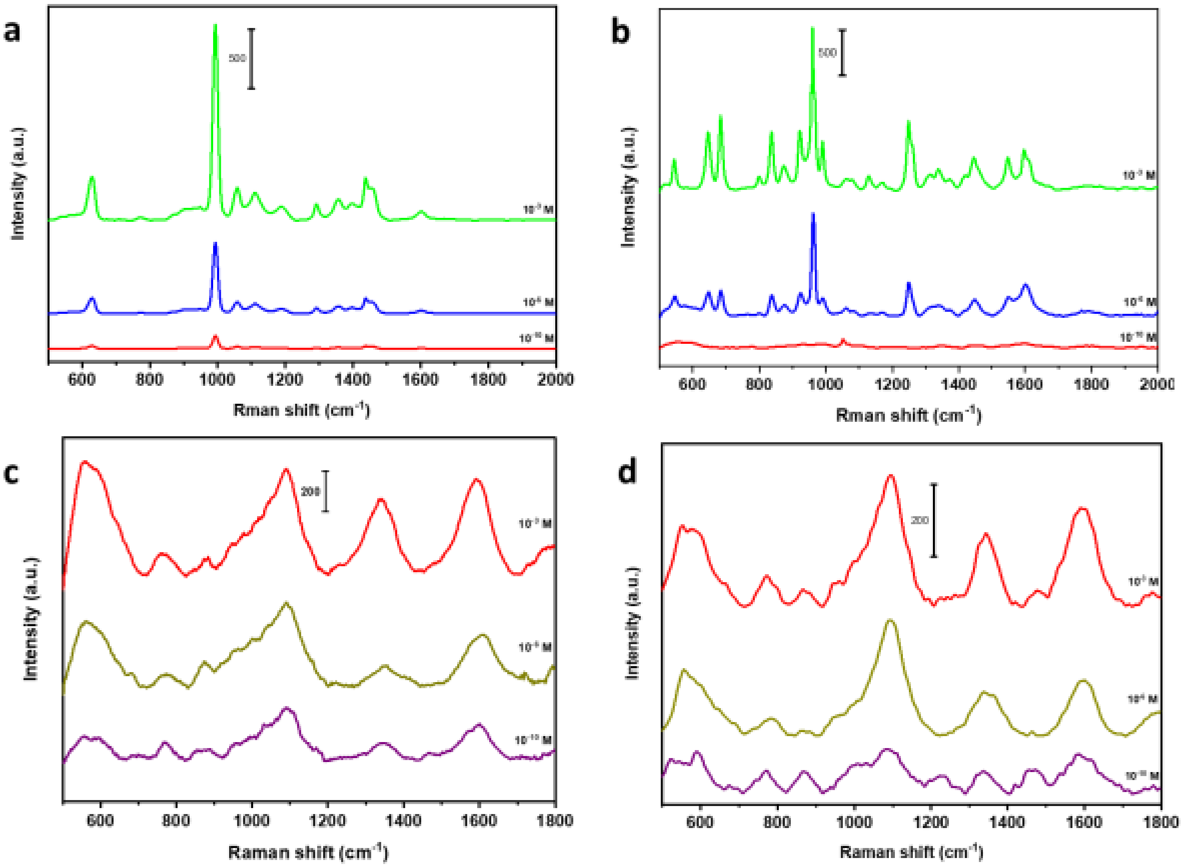

APENDIX B: MERCAPTOPYDIDINE-FUNCTIONALIZED GOLD NANOPARTICLES@CARBON NANODOTS FOR MERCURY DETECTION

Figure B4.1. SEM image of AuNPs (A), HR-TEM image of AuNPs (B), and HR-TEM image of AuNPs@CNDs (C).

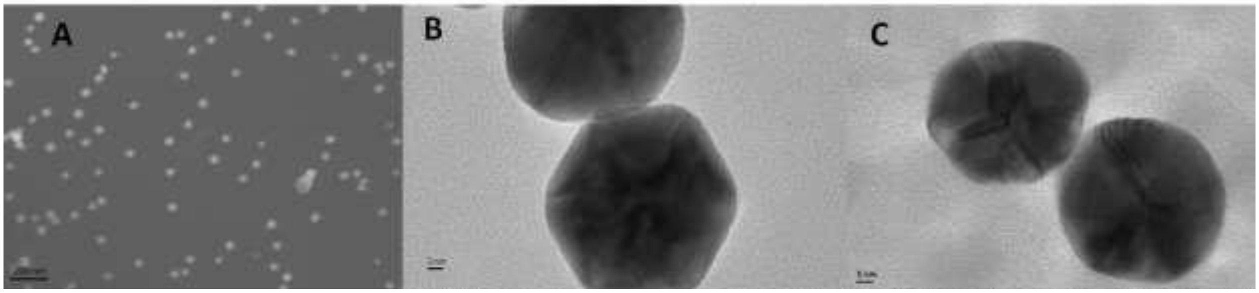

Figure B4.2. (A) UV-Vis absorption spectra of AuNPs, CNDs and hybrid AuNP@CNDs and (B) Raman spectra of AuNPs@CNDs and CNDs.

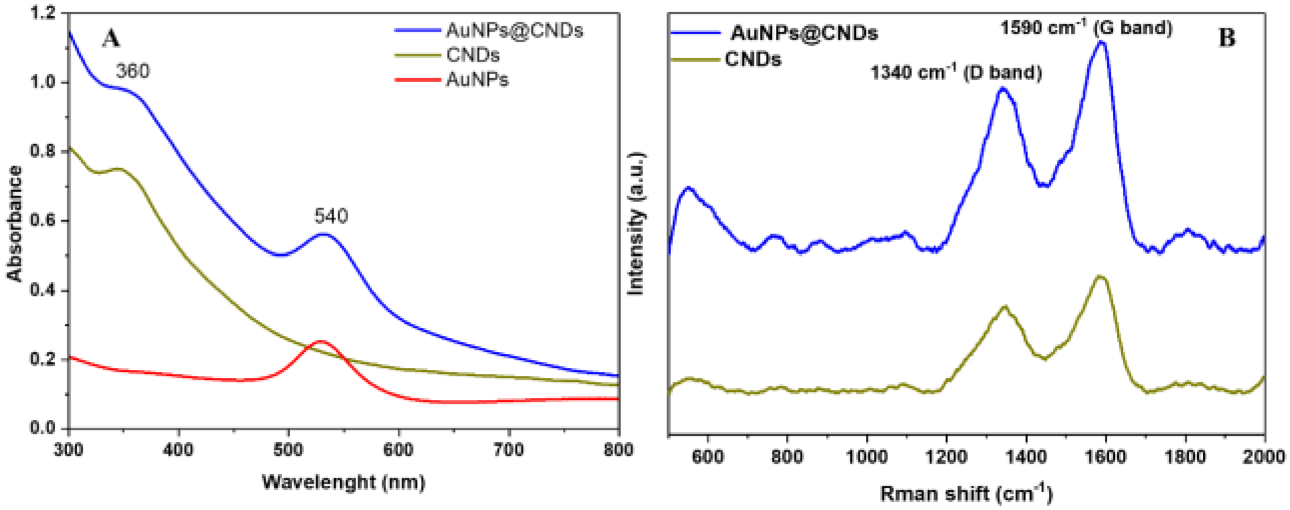

Figure B4.3. SERS of Rh6G with the hybrid AuNPs@CNDs generated with different mass ratios.

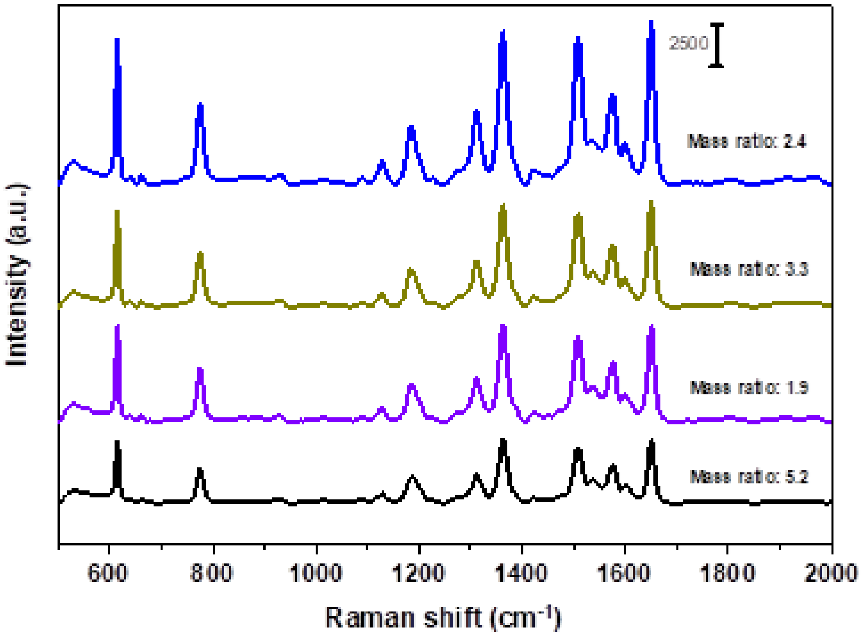

Figure B4.4. (A) Full-scan XPS spectrum of AuNPs@CNDs and MPY-functionalized AuNPs@CNDs; (B) N 1s XPS spectra; (C) C 1s spectra; (D) O 1s XPS spectra of AuNPs@CNDs.

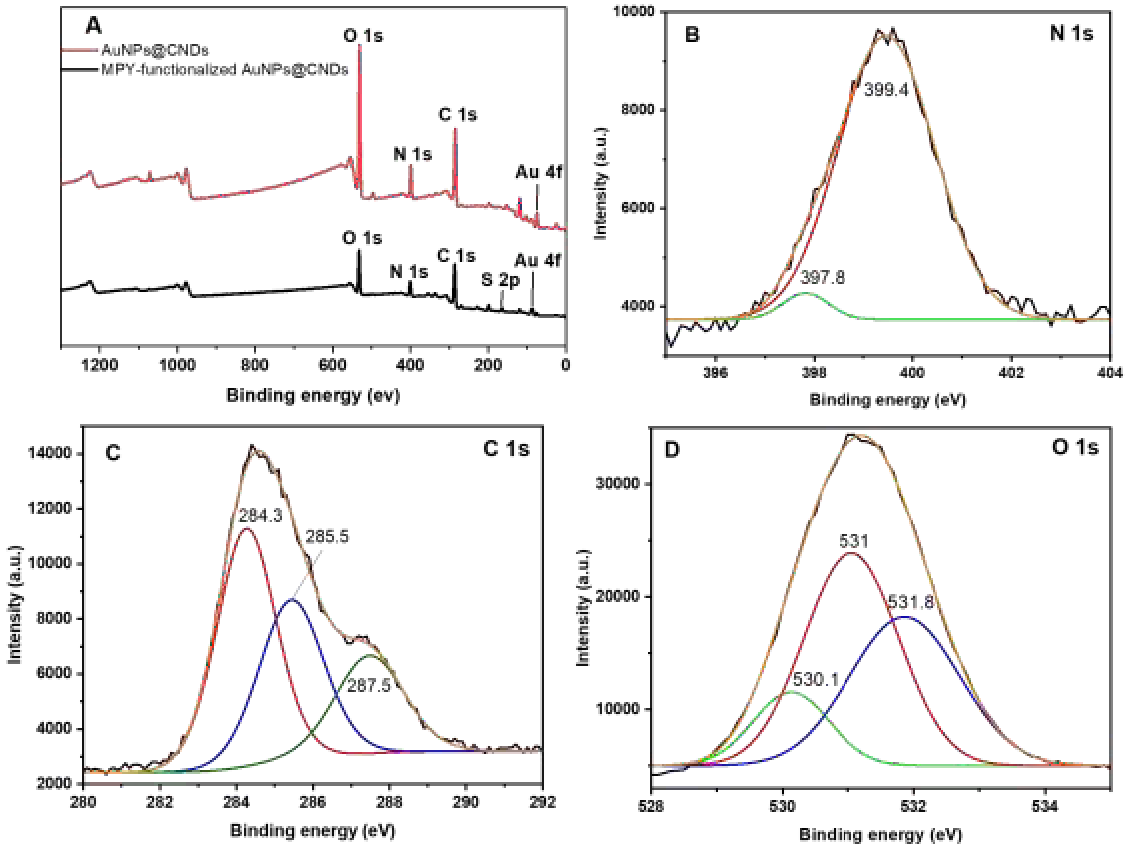

Figure B4.5. SERS spectra of MPY-functionalized AuNPs@CNDs after incubation in 0.48 µM Hg^{2+} for the times indicated (A). Intensity ratio, I_{717}/I_{431}, as a function of incubation time (B).

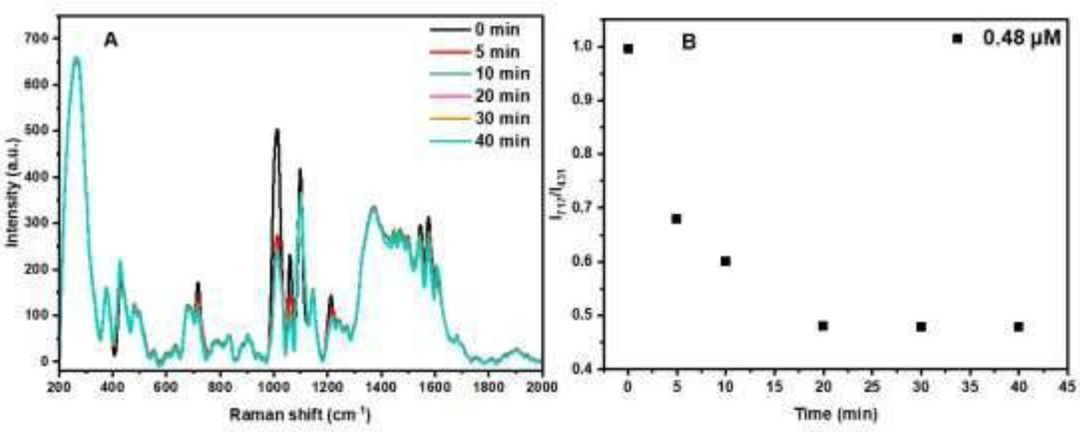

Figure B4.6. SERS spectra of mercury on simulated water.

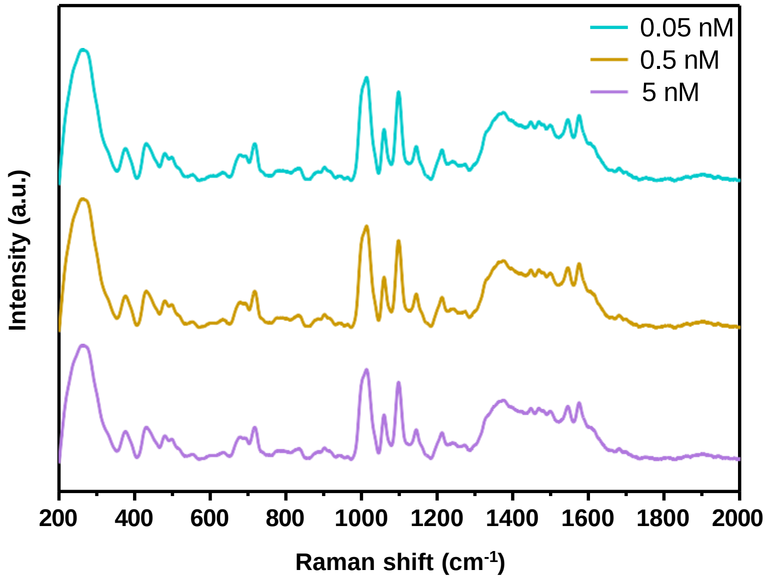

Limit of detection for toxic compounds:

The limit of detection (LOD) was obtained by dividing the standard deviation (SD) of triplicate measurements of blank noise peak obtained from AuNPs@CNDs SERS spectra without toxic compound (Rh6G, herbicides, or mercury) by the slope value (σ) from the toxic compound's calibration curve using the formula shown below:

$$\text{LOD} = 3 \times \frac{SD}{\sigma}$$

Table B4.1. Summary of LODs

Target compound	**LOD**
Rh6G	3.08×10^{-12} (M)
CGA77102	16.85×10^{-10} (M)
A19414A	19.45×10^{-10} (M)
ZA1296E	48.93×10^{-10} (M)
A12738A	41.096×10^{-10} (M)
Mercury	0.073×10^{-8} (nM)